

Electromechanical Properties of Graphene Oxide as a Two-dimensional Actuator

by

Zhenyue Chang
Bachelor of Engineering (Mechanical) (Hons.)

*Thesis submitted in fulfilment
of the requirements for the degree of*

Doctor of Philosophy



Supervisor: Dr. Zhe Liu

Associate Supervisor: Assoc. Prof. Wenyi Yan

Department of Mechanical and Aerospace Engineering
Faculty of Engineering
Monash University
Australia

May 2016

© Copyright

by

Zhenyue Chang

2016

Electromechanical Properties of Graphene Oxide as a Two-dimensional Actuator

Copyright Notices

Notice 1

Under the Copyright Act 1968, this thesis must be used only under the normal conditions of scholarly fair dealing. In particular no results or conclusions should be extracted from it, nor should it be copied or closely paraphrased in whole or in part without written consent of the author. Proper written acknowledgement should be made for any assistance obtained from this thesis.

Notice 2

I certify that I have made all reasonable efforts to secure copyright permissions for third-party content included in this thesis and have not knowingly added copyright content to my work without the owner's permission.



Zhenyue Chang
28th May 2016

"Life is like a box of chocolates, you never know what you're gonna get."

Forrest Gump

In dedication to my parents

Acknowledgements

Firstly, I would like to express my deepest gratitude to my supervisors, Dr. Zhe Liu and Associate Professor Wenyi Yan for their continuous support, guidance, encouragement and understanding throughout my Ph.D study. I am extremely appreciative of the incredible patience and freedom given to run riot with ideas. I could not have asked for better mentors.

Secondly, I thank my fellow colleagues and friends for the stimulating discussions, and for making this journey an unforgettable and entertaining one. The opportunity to work with an amazing and diverse group of people is an experience that I will cherish forever.

To the Department of Mechanical and Aerospace Engineering, the Faculty of Engineering and the Monash Graduate Education, thank you for the technical and administrative support given throughout my candidature.

To my friends, thank you for the continuous encouragement and emotional support which kept me sane in completing the work and the writing up of this thesis.

To my wife, Yaoxin Hu, thank you for your support in my life and study, for the comments and suggestions given on my paper and thesis writing, for your care and love.

Finally, to my mother, Jiasu Chang thank you for your unconditional love and support. This dream would not have been possible without your countless sacrifices.

Zhenyue Chang
Monash University
May 2016

Contents

Acknowledgements	vi
List of Figures	ix
List of Tables	x
Abstract	xi
Publications and Outcomes	xiv
1 Introduction	1
1.1 Miniaturization of Actuator	1
1.2 The Rise of Graphene	5
1.3 Thesis Overview	6
1.3.1 Chapter 2: Background, Theory and Method	7
1.3.2 Chapter 3: Piezoelectric Properties of Graphene Oxide	7
1.3.3 Chapter 4: Two-dimensional Shape Memory Graphene Oxide	7
1.3.4 Chapter 5: Two-way Quantum Mechanical Actuation of Graphene Oxide	8
1.3.5 Chapter 6: Conclusion and Future Work	8
2 Background, Theory and Method	9
2.1 Graphene Oxide	9
2.1.1 Graphene Oxide with Ordered Epoxy Groups	10
2.2 Piezoelectric Effect	16
2.2.1 Piezoelectricity at Nanoscale	18
2.2.2 Atomically Thin Piezoelectric Materials	20
2.2.3 Graphene-based Piezoelectric Materials	20
2.3 Shape Memory Effect	23
2.3.1 Shape Memory Materials and Shape Memory Mechanisms	24
2.3.2 Multi-shape Memory Effect	27
2.3.3 Shape Memory Effect at Nanoscales	27
2.4 Quantum Mechanical Effect	29
2.4.1 Actuation of Carbon-based Materials	29

2.4.2	Quantum Mechanical Effect of Graphene and Graphene Oxide with Order Epoxy Groups	32
2.5	Density Functional Theory	36
3	Piezoelectric Properties of Graphene Oxide	40
3.1	Overview	40
3.2	Publication	40
4	Two-dimensional Shape Memory Graphene Oxide	48
4.1	Overview	48
4.2	Publication	48
5	Two-way Quantum Mechanical Actuation of Graphene Oxide	76
5.1	Overview	76
5.2	Publication	76
6	Conclusions and Future Work	86
6.1	Contributions	86
6.2	Ongoing and Future Work	87
	Bibliography	89

List of Figures

1.1	Progress of Miniaturization.	1
1.2	(a) Crystallographic structure of graphene. Atoms from different sublattices (A and B) are marked by different colours.(b) Band structure of graphene. Reprinted from Materials Today, Vol 10, Mikhail I. Katsnelson, Graphene: carbon in two dimensions, Pages 20-27, Copyright(2007), with permission from Elsevier. [1]	5
2.1	Structure of Graphene Oxide. Reprinted with permission from [2] Copyright (2010) American Chemical Society.	9
2.2	(a) NC-AFM image of the oxidized single graphene sheet with ordered wrinkles. (b) Magnified NC-AFM image of the area indicated by the white square in (a). Average height profile obtained for the dotted area indicated in (b) is superimposed on the image (z-scale bar = 300 pm). Imaging conditions: cantilever = NSC11, $\Delta f = -20$ Hz, $V_b = 0$ V.(c) Possible structural model of the linear epoxy groups for the observed height profile in (b) is shown. In the stick and ball model, carbon and oxygen atoms are gray and red, respectively. Reprinted with permission from [2] Copyright (2010) American Chemical Society.	11
2.3	Crystal structure of symmetric (a) and asymmetric C_8O (b) with a and b as the lattice constant in x and y -axis. Black and red spheres represent the carbon (C) and oxygen (O) atoms, respectively. Angle α measures the bond angle of oxygen atom and its two neighbouring carbon atoms. The symmetric C_8O unit cell contains 8 carbon atoms and 1 oxygen atom, and the asymmetric C_8O unit cell contains 16 carbon atoms and 2 oxygen atoms.	12
2.4	(a,b) Energetic for the formation and growth of an extended linear defect from the O diffusion to the NNN ET trimer (c,d). Schematic representation of further nucleation and growth of O-driven unzipping in graphene. Reprinted with permission from [3] Copyright (2012) American Chemical Society.	13

2.5	(a) Graphene monolayer transferred to a flexible polymer substrate. (b) The polymer substrate is bent and thus strain is exerted on the attached graphene sheet. (c) Annealing of adsorbed O atoms forms parallel epoxy chains on the graphene. (d) Under further oxidation, the graphene layer is unzipped into nanoribbons. Note that further oxidation in (d) is not necessary for this study. Reprinted with permission from [4] Copyright (2011) John Wiley and Sons.	14
2.6	(a,b) STM images of UHV epitaxial graphene before (a) and after (b) annealing at 260 °C. (c) STM image showing a region of the UHV oxidized epitaxial graphene surface where chemisorbed oxygen has been reversibly desorbed by injection electrons from the STM tip at a sample bias of +4.0 V and tunnelling current of 1 nA. (d,e) STM images before (d) and after (e) hopping of chemisorbed oxygen on epitaxial graphene at room temperature. The displace oxygen adatom is indicated in (e). All STM images were acquired at a sample bias of +2.4 V and a tunnelling current of 50 pA. Reprinted by permission from Macmillan Publishers Ltd: Nature Chemistry, [5] Copyright (2012).	15
2.7	Piezoelectric transduction (a) 33 model (b) 31 model.	17
2.8	(a) Pristine GNR, circular hole GNR, and graphene sheet with triangular hole. The white colored atoms refer to hydrogen atoms which mark the termination of GNR. (b) The development of polarization for triangular-hole-graphene sheet under the action of strain. Reprinted from [6] with the permission of AIP Publishing Copyright (2012)	21
2.9	(a) Unit cells for each of the adatom cases studied are highlighted in yellow. Periodic boundary conditions are employed in all cases. (b) Point group symmetry of lattice unit cells for each case of atom adsorption considered here. In all cases, inversion symmetry is destroyed, leading to piezoelectricity. (c) An external electric field applied perpendicular to the graphene sheet induces an equibiaxial strain in the plane of the sheet. This results in a linear relationship between the electric field and strain at low fields, the slope of which gives the d_{31} piezoelectric coefficient. Reprinted with permission from [7]. Copyright (2012) American Chemical Society.	22
2.10	Comparison between SME and SCE from an energy point of view.	23
2.11	Schematic of shape memory mechanism for thermal-responsive SMA.	24
2.12	Schematic of shape memory mechanism for thermal-responsive SMP.	25
2.13	Specific modulus (ratio of elastic modulus over density) as a function of maximum recoverable elastic strain for common actuation materials (including SMA and SMP highlighted in yellow). Adapted from references [8,9].	26
2.14	Schematic of multi-shape memory effect for thermal-responsive SMP.	27
2.15	Quantum Mechanical Actuation of Graphene upon charge injection.	29

2.16	(a) Experimentally derived changes in basal plane strain as a function of nominal charge for graphite intercalation compounds. (b) Schematic illustration of charge injection in a nanotube-based electromechanical actuator and the effect of nanotube bundling. From [10]. Reprinted with permission from AAAS.	30
2.17	(a) Schematic of a suspended graphene resonator. (b) An optical image of a double-layer graphene sheet that becomes a single suspended layer over the trench. Scale bar, 2 μm . Each colored circle corresponds to a point where a Raman spectrum was measured. (c) Raman signal from a scan on the graphene piece. Each colored scan is data taken at each of the matching colored circles. The top scan is used as a reference and corresponds to the Raman shift of bulk graphite. (d) An optical image of few-layer (~ 4) graphene suspended over a trench and contacting a gold electrode. Scale bar, 1 μm . (Inset) A line scan from tapping mode AFM corresponding to the dashed line in the optical image. It shows a step height of 1.5 nm. (e) A scanning electron microscope image of a few-layer (~ 2) graphene resonator. Scale bar, 1 μm . From [11]. Reprinted with permission from AAAS.	31
2.18	(a) Cross-section SEM image of a graphene film (scale bar: 1 μm) asymmetrically treated with hexane and oxygen plasma (schematic illustration). (b) Curvature change of an Asy-modified graphene strip as a function of applied CV potential within 1.2 V. Insets show the status of the graphene strip at 1.2, 0, and 1.2 V, respectively. Reprinted with permission from [12]. Copyright (2010) American Chemical Society.	32
2.19	(a) Tip displacement of the cantilever beam as a function of temperature. Each data point is the average value of five measurements, and the standard deviation is shown as error bars. The solid line shows the fit to the data obtained from FEA. The insets show the SEM images of the initial position of the cantilever beam (top left) and bend up state upon applying electrical power (rightbottom). (b) Graphene-on-organic film which is in the form of a dragonfly wing. Reprinted with permission from [13]. Copyright (2011) American Chemical Society.	33
2.20	Quantum mechanical and Electrostatic Double-Layer (EDL) effects of graphene actuation. Reprinted with permission from [14] Copyright (2011) American Chemical Society.	33
2.21	(a) Actuation of GO (clamped and unzipped) and pristine graphene due to positive (hole) and negative (electron) charge injection. Inset: close-up of the strain responses between -0.15 and $+0.05$ e per C-atom charge injection. (b) Total strain analysis and excess charge density profile of clamped and unzipped GO upon electron injection. Reprinted with permission from [15] Copyright (2012) American Chemical Society.	34

List of Tables

1.1 Comparison of Actuation Mechanisms.	2
---	---

ABSTRACT

Fast growing miniaturization technologies in various fields have been facilitating the development of actuators in micro/nanoelectromechanical systems. Advanced futuristic actuator requires not only high in actuation performances, but also easy in designing, fabrication, monitoring and controlling at nanoscopic or even atomic scale. Many conventional electric and magnetic actuation materials are not suitable for miniaturization mainly due to the unfavourable scaling factor. Functional materials (or namely smart material), on the other hand, have received extensive attentions thanks to their inherent ability to deform at small scales upon an appropriate extremal stimulus. Piezoelectric materials, shape memory materials, and electro-active materials are three most widely used smart materials for actuation. Not surprisingly, these materials have been successfully employed in a myriad of applications at nanoscopic scales. For instance, many commonly studied atomically thin materials have been reported to exhibit piezoelectric effect, both theoretically and experimentally. Nanoscopic shape memory effect of traditional shape memory materials, like shape memory alloys and shape memory polymers, is observed. Additionally, quantum mechanical effect of nano electro-active materials, such as carbon nanotubes, has inspired many new opportunities in quantum mechanical actuation of graphene-based and two-dimensional materials. Here, we look at electromechanical properties of monolayer graphene oxide crystals that could potentially enable the possibility of designing two-dimensional actuators. In this thesis, three types of electromechanical properties of graphene oxide crystals (i.e. piezoelectric, shape memory, and quantum mechanical effects) are explored via Density Functional Theory calculations. Firstly, highly ordered graphene oxide crystals were found to exhibit a maximum in-plane strain of 0.12 % induced by piezoelectric response. Secondly, a two-dimensional shape memory graphene oxide was discovered. The recoverable strain is as large as 14.5 %. Lastly, some graphene oxide crystals can have two-way quantum mechanical actuation performances. Specifically, a single piece of graphene oxide crystal is capable of both expansion and contraction upon electron injection only, thanks to the existence of intrinsic bi-stable phases. Throughout this thesis, a case is made for monolayer graphene oxide crystals to be utilised in developing different types of electromechanical nano- or two-dimensional actuators.

Monash University

Declaration for thesis based or partially based on conjointly published or unpublished work

General Declaration

In accordance with Monash University Doctorate Regulation 17.2 Doctor of Philosophy and Research Master's regulations the following declarations are made:

I hereby declare that this thesis contains no material which has been accepted for the award of any other degree or diploma at any university or equivalent institution and that, to the best of my knowledge and belief, this thesis contains no material previously published or written by another person, except where due reference is made in the text of the thesis.

This thesis include 1 original paper published, 1 original paper accepted (in press), and 1 original paper submitted and currently under consideration in peer reviewed journals. The core theme of the thesis is to explore the electromechanical properties of graphene oxide as a two-dimensional actuator. The ideas, development and writing up of all the papers in the thesis were the principal responsibility of myself, the candidate, working within Department of Mechanical and Aerospace Engineering, Faculty of Engineering, under the supervision of Dr. Zhe Liu and Assoc. Prof. Wenyi Yan.

The inclusion of co-authors reflects the fact that the work came from active collaboration between researchers and acknowledges input into team-based research.

In the case of Chapters 3–5 my contribution to the work involved the following:

Thesis chapter	Publication title	Publication status	Nature and extent of candidate's contribution
3	Piezoelectric Properties of Graphene Oxide: A First-principles Computational Study	Published	Conceive the idea, design the model, run simulations, results analysis, interpretation and writing.
4	Two-Dimensional Shape Memory Graphene Oxide	Accepted	Conceive the idea, design the model, run simulations, results analysis, interpretation and writing.
5	Two-way Quantum Mechanical Actuation of Graphene Oxide	Submitted	Conceive the idea, design the model, run simulations, results analysis, interpretation and writing.

I have not renumbered sections of submitted or published papers in order to generate a consistent presentation within the thesis.

Signed:



Name: Zhenyue Chang

Date: 28th May 2016

Publications and Outcomes

Articles in peer-reviewed journals

1. **Zhenyue Chang**, Wenyi Yan, Jin Shang, and Jefferson Zhe Liu. Piezoelectric properties of graphene oxide: A first-principles computational study. *Applied Physics Letters*, 105(2):023103, 2014. [16]
2. **Zhenyue Chang**, Junkai Deng, Ganaka G. Chandrakumara, Wenyi Yan and Jefferson Zhe Liu. Two-Dimensional Shape Memory Graphene Oxide. *Nature Communications*, DOI: 10.1038/ncomms11972, Article In Press, 2016. [17]
3. **Zhenyue Chang**, Junkai Deng, Ganaka G. Chandrakumara, Wenyi Yan and Jefferson Zhe Liu. Two-way Quantum Mechanical Actuation of Graphene Oxide. Submitted.
4. Junkai Deng, **Zhenyue Chang**, Tong Zhao, Xiangdong Ding, Jun Sun and Jefferson Zhe Liu. Electric Field Induced Reversible Phase Transition in Li Doped Phosphorene: Shape Memory Effect and Superelasticity. *Journal of The American Chemical Society*, 138(14):4772-4778, 2016. [18]
5. Qianhui Zhang, **Zhenyue Chang**, Guanzhong Xu, Yupeng Zhang, Zai-Quan Xu, Qiaoliang Bao, Jefferson Zhe Liu, Yui-Wing Mai, Wenhui Duan, Michael S. Fuhrer, Changxi Zheng. Strain Relaxation of Monolayer WS₂ on Plastic Substrate. Submitted.

Chapter 1

Introduction

“What could we do with layered structures with just the right layers? What would the properties of materials be if we could really arrange the atoms the way we want them?”

At the atomic level, we have new kinds of forces and new kinds of possibilities, new kinds of effects.”

Richard P. Feynman

In this chapter, miniaturization of actuator and the rise of graphene are to be introduced. This is followed by a brief overview of the outline and layout of the thesis.

1.1 Miniaturization of Actuator

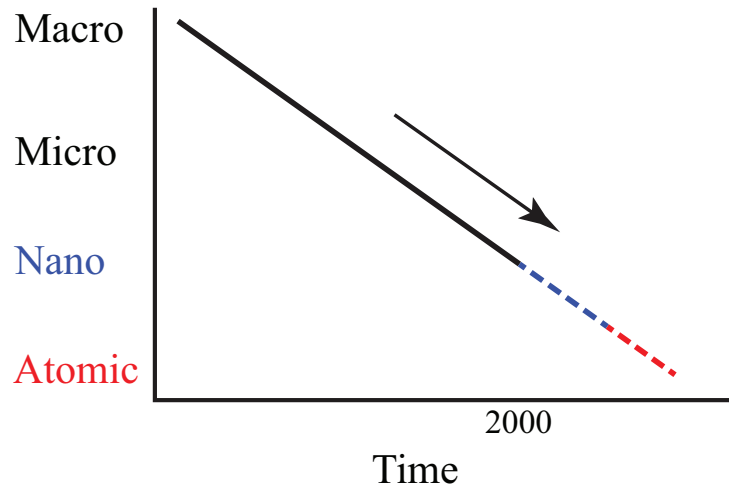


Figure 1.1: Progress of Miniaturization.

As predicted by Richard Feynman more than 50 years ago, miniaturization is considered as the most significant enabling technology of the last century. [19] Because of the rapid development of miniaturization technology Fig. 1.1, [20] the ability to design and fabricate intelligent and autonomous micro/nano-electronics has given birth to micro/nano-electromechanical systems (MEMS/NEMS), which attracted intensive attention range from

Table 1.1: Comparison of Actuation Mechanisms.

	Actuation Principle	Developed force/torque	Range of Motion	Response	Power density
Electric/ Magnetic	Electromagnetic	Small	Large	Fast	High
	Electrostatic	Medium	Small	Fast	Low
Functional Materials- Based	Piezoelectric	Large	Small	Fast	High
	Shape Memory	Medium	Large	Medium	Very High
	Electro-active	Small	Large	Fast	Low
	Quantum Mechanical	Large	Small to Large	Fast	Small to Large

biomedical applications to aerospace industry. [21–23] Consequently, there is no doubt that further miniaturization of such devices/systems to the ultimate atomic scale with greater control and precision will not only continue, but also it will become a dominant technological development in the near future.

An actuator - a device that converts external energy (e.g. electrical, thermal, chemical and magnetic energies) to controllable mechanical deformation or motion - is the core component of many such devices/systems. [24–28] Enormous amount efforts have been made towards the development of actuator with desired properties and characteristics at a microscale or even nanoscale, from which it has been concluded that while the same material constant or physical law applied in the micro and macro world, the effect of these parameters on the whole system and its performance changes dramatically. [20] That is being said, there are several considerations that must be carefully taken into account when making the correct choice of which actuation mechanism is to be implemented for a particular application at small scales. Among them, scaling law acts as the major deciding factor in this emerging technology. Table 1.1 summarizes six commonly used actuation mechanisms available for the miniaturization of actuator, associated with their inherent properties. [20, 29–32]

Overall, these actuation mechanisms are divided into two group. Conventional electric/magnetic actuation in which the actuation is achieved by connecting links through kinematic pairs, similar to the macroscopic devices. Alternatively, functional materials-based (sometimes also called *smart materials*) actuation is generated by the shape deformation of the materials upon the external stimulus (i.e. stimuli-responsive materials), such as electric field, mechanical force and heat.

Electromagnetic actuation is based on the attractive and repulsive forces generated on conductors carrying current in a magnetic field. It is the most widely used actuator in

devices and machines of macroscales thanks to its smooth and quick response on top of the high power density, electric-motor is a good example. [24] However, it is rarely used in micro/nanometre scales due to poor scalability of the electromagnetic force (i.e. $F \propto l^4$). Besides the unfavourable downwards scaling, it is very difficult to implement electromagnetic actuators at small scales due to the complexity of arranging the current-carrying conductor in perpendicular with the moving elements. [20, 31] As such, electromagnetic actuators are not advantageous for MEMS/NEMS.

The electrostatic actuation results from Coulomb force of between two oppositely charged surfaces. Although the electrostatic force is relatively small, clear advantages like fast response and a much better electrostatic force scale of $F \propto l^2$, make it potentially useful for micro/nano-actuators. [33] However, electrostatic actuation inherently exhibits low power density and limited displacement. More importantly, the accurate position control of the two oppositely charged surfaces is extremely difficult because of the scaling effects on surface-related forces at small scales, such as adhesion and stiction. [20] This problem remains as serious obstacle in developing electrostatic actuators for MEMS/NEMS because it may cause some operational issue.

Expectedly, advanced actuators for MEMS/NEMS in the future need to revolutionary in comparison to the conventional system. For example, this is a clear trend that a large amount of elements (e.g. actuators and sensors) need to be integrated into extremely small systems for multi-functional purposes. Based on the conventional actuation mechanisms as discussed in the previous two paragraphs, it is quite challenging to assemble different elements of the system even at microscale using current lithographic technology. Although some sophisticated fabrication techniques can achieve the assembly of MEMS/NEMS down to a few nanometer size recently, notably issues like batch production and reliability still remain. [34]

To meet the requirement that MEMS/NEMS need to be monolithic and integrated to become more intelligent and autonomous, functional-based materials look very promising in this case because these materials can not only form the main body of the MEMS/NEMS, but certain parts of the materials can also provide actuation or sensing simultaneously. [35] Subsequently, it is foreseeable that smart materials will play dominate role in developing advanced actuators at nanoscopic or even atomic scales. Three typical actuation mechanisms of functional-based materials that directly related to the major works of this thesis are introduced as following.

Piezoelectricity was first demonstrated in 1880 by the French physicists Pierre and Jacques Curie. The word 'piezo' in Greek means 'to squeeze or press', which implies electricity resulting from pressure. [36] A piezoelectric material is classified as a crystalline material without inversion symmetry that exhibits a linear electromechanical strain when subjected to the electric field. The piezoelectric effect is a reversible process, whereby,

piezoelectric materials is able to convert a mechanical strain into an electrical signal. [36] Owing to this interesting phenomenon, piezoelectric materials are widely used to operate as actuators and sensors in various applications. [37] Despite relatively small strain performance (i.e. usually less than 1 %), piezoelectric actuation exhibits many highly desirable traits, including fast response, high power density and linear electric field-displacement. Predominately, the largely developed force/torque scaling renders piezoelectricity a very promising candidate for actuation at small scales. [38,39] A more in-depth literature review of using piezoelectric materials at micro-/nanoscopic scales will be discussed in Chapter 2.

Another widely implemented smart material actuation mechanism is based on shape memory materials (SMMs). They are featured by the ability to recover their original shape from a significant deformation upon an appropriate external stimulus. [40] This shape memory phenomenon (also known as shape memory effect (SME)), occurs as a result of reversible phase transformation, is apparently ideal for actuation applications. [41] Two major SMMs (i.e. shape memory alloys and shape memory polymers) are commonly used. In general, reasonably large strain output associated with very high power density can be generated. Although most SMMs are stimulated by heat (which results in a shortcoming of medium or slow response as indicated in Table 1.1), the response speed of more recent SMMs can vary depends on the use of external stimuli, for example, electricity and light. [42] Additionally, SMMs have a fascinating feature, so-called programmability. [43] This feature enable the possibility that SMMs can be programmed for actuation following a predetermined sequence, just like machines but with greater intelligence and flexibility, whereby, the material can actuate, sense and react accordingly just like a machine. [35] This is particularly desirable for the purpose of integration within MEMS/NEMS, and thus utilizing SME in miniaturized actuators is very attractive.

The terminology of electroactive (EA) materials is a rather general description for a range of smart materials. The most commonly used EA material for advanced actuation is EA Polymers (EAPs). In general, EAPs actuators can be classified into two main groups based on their actuation mechanisms, which are well-known as Electronic and Ionic EAP, respectively. More recently discovered carbon nanotube (CNT) and graphene-based materials (detailed in Section 2.4) also belong to the family of EA materials. [44] The three most promising actuation mechanisms employed by EA materials are electrostatic effect for Electronic EAP, [45] ionic intercalation for Ionic EAP and quantum mechanical effects for CNT and graphene-based materials. [10,14] While EAP materials exhibit large strain output and fast response speed, they inherently have small force/torque scaling and low power density. Moreover, they also suffer from operational problems like short cycle life and low energy conversion efficiency. [44]

On the other hand, covalent carbon-carbon bond length change at the atomic scale in highly publicised CNT and graphene-based materials can be used as actuation. [10,14] The most contemporary actuation mechanism is called quantum mechanical effect, in which the

strain output is induced by charge injection into the material. [14] Although the currently reported strain output of quantum mechanical actuation is significantly smaller than that of based on EAPs, the response speed is extremely fast and there is no need to consider scaling law in this case thanks to the nanoscopic scale nature of these carbon-based materials. Thus, quantum mechanical actuation is promising to offer exciting actuation possibilities in advanced actuation technology, such as biomimetic technology and artificial muscle. [46,47]

1.2 The Rise of Graphene

As noted in the previous section, the ultimate goal of miniaturization will be manipulating atoms, it is therefore naturally and unavoidable for us to focus on the materials used and the corresponding energy employed, especially at nanoscopic or even atomic scale.

Graphene, a two-dimensional sheet of carbon honeycomb network, has become the superstar in physics, material science and nanotechnology since its first discovery by A.K. Geim and K. S. Novoselov in 2004. [48] Graphene has many extraordinary physical properties. It was reported that graphene exhibits a Young's modulus of about 1.0 TPa and a breaking strength of approximately 40 Nm^{-1} . Amazingly, it is also elastically stretchable (i.e. approximately 20 %), which is more than any other crystal. [49] Graphene is a perfect thermal conductor as well. A thermal conductivity value of about $5000 \text{ Wm}^{-1}\text{k}^{-1}$ was obtained for a suspended monolayer graphene flake, produced by using mechanical exfoliation. It is much higher than the value observed in all other carbon structures like carbon nanotubes, graphite, and diamond. For instance, graphite shows a smaller thermal conductivity about $1000 \text{ Wm}^{-1}\text{k}^{-1}$. [50]

The primary reason makes graphene extremely attractive in various fields is due to its extraordinary and unique electronic properties. The most discussed is graphene's electronic spectrum. Electrons propagating through the honeycomb lattice completely lose

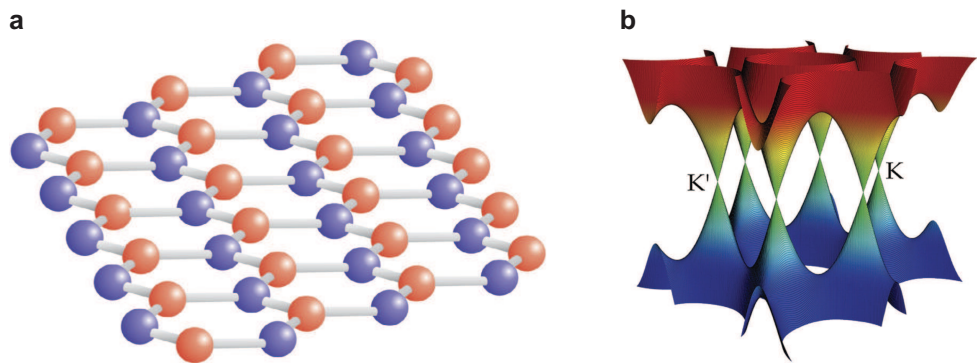


Figure 1.2: (a) Crystallographic structure of graphene. Atoms from different sublattices (A and B) are marked by different colours.(b) Band structure of graphene. Reprinted from Materials Today, Vol 10, Mikhail I. Katsnelson, Graphene: carbon in two dimensions, Pages 20-27, Copyright(2007), with permission from Elsevier. [1]

their effective mass, which results in the Dirac spectrum for massless fermions or quasiparticles. [51–53] More specifically, charges carriers in graphene are described by a Dirac-like spectrum as a direct consequence of graphene’s near perfect crystal structure, two equivalent carbon sublattices A and B (Fig. 1.2 (a)). Two energy bands are formed at K and K’ points (Fig. 1.2 (b)) as a result of quantum-mechanical hopping between sublattice A and B. Besides, the conical energy spectrum is constructed near the edge of the Brillouin zone. Consequently, quasiparticles in graphene are act as massless relativistic particles (because of the linear dispersion relation is given by $E = \hbar k V_f$, where E is the electron energy, \hbar is the Planck’s constant, k is the wavevector, and V_f is the Fermi velocity), and the role of the speed of light c is replaced by the Fermi velocity $V_f \approx c/300$. This means that the electrons travel through the graphene sheet as fast as just one hundredth that of the speed of light, and as if they carry no mass. [1,54] A carrier mobility in excess of $200,000 \text{ cm}^2\text{V}^{-1}$ is measured in 2008. [55]

These outstanding properties immediately generated extensive interest in the utilization of graphene in a broad range of devices. Such as electromechanical resonators, [11] ultrahigh-frequency transistors, [56] development of next generation semiconductor, [57] advanced sensors [58] and actuators. [26,59] Although countless astonishing graphene-based devices have already been created in the last decade, there still remains plenty of unexplored areas that need for further research. A substantial reason is that pristine graphene can be subjected to various structural modifications and surface functionalization, [60] which leads to myriad possibilities beyond graphene.

The vast diversity of graphene oxide (GO) atomistic structures is a good example of this. (A more in-depth literature review of GO and multiple GO crystals simulated in this thesis will be discussed in Section 2.1) By considering two-dimensional GO crystal as a smart material for developing advanced actuators at atomic level, three comprehensive studies in thesis lead to the successful demonstration of piezoelectric properties of GO, the discovery of two-dimensional shape memory GO and the observations of quantum mechanical actuation associated new phenomena and high strain performance.

1.3 Thesis Overview

The scope of this thesis has been to investigate the virtually unexplored opportunities of using two-dimensional graphene oxide crystals as smart materials-based electromechanical actuators. Three basic actuation mechanisms (i.e. piezoelectric, shape memory and quantum mechanical effects) are reviewed and they are successfully realized in graphene oxide associated with the comprehensive physical understandings at atomic scale, as well as, considerably high actuation performances, thus the main scope of this thesis. The external electric field is applied perpendicular to the GO surface to achieve the highly desirable two-dimensional piezoelectric and shape memory actuators. By providing the evidence that GO crystal is programmable, GO has been revealed as the first reported

two-dimensional shape memory material. Furthermore, upon the electron injection, two-way quantum mechanical actuation phenomenon is observed thanks to the existence of multiple phases in various GO crystals.

1.3.1 Chapter 2: Background, Theory and Method

In Chapter 2, a thorough literature review and the background theory on three actuation mechanisms of functional materials-based actuators and more specifically at micro/nanoscale is done. A discussion of density functional theory along with a brief overview of Vienna Ab initio Simulation Package (VASP) used throughout this thesis is included.

1.3.2 Chapter 3: Piezoelectric Properties of Graphene Oxide

In this Chapter, two types of highly ordered graphene oxide (GO) crystals (i.e. clamped and unzipped) are shown to exhibit piezoelectric effect via first-principle density functional calculations. The maximum in-plane strain of 0.12 % and piezoelectric strain coefficient (d_{31}) of 0.24 pmV^{-1} can be obtained by applying an electric field perpendicular to the GO basal plane. These values are comparable with those of some advanced piezoelectric materials. An in-depth crystal structural analysis revealed that the strain output or piezoelectric strain coefficient d_{31} is highly depends on the oxygen doping rate, in where higher oxygen concentration giving rise to a larger d_{31} in clamped GO whereas leading to a reduced d_{31} in the unzipped GO. Thanks to the fact that piezoelectric effect is a reversible process, this thinnest two-dimensional piezoelectric material enables great potential of adopting GO as not only actuators, but also sensors a wide range of extremely small applications. Publication of results [16] from this study is included in this thesis chapter.

1.3.3 Chapter 4: Two-dimensional Shape Memory Graphene Oxide

Here, in Chapter 4 the discovery of shape memory effect in a two-dimensional atomically thin graphene oxide is demonstrated using density functional theory (DFT) calculations. Graphene oxide with ordered epoxy groups, C_8O , is found to have two intrinsically stable phases (or so-called bi-stable phases). Upon a combination stimulus of applied electric field and mechanical force, reversible phase transformation between these two phases lead to a maximum large recoverable strain of 14.5 %. Detailed electronic and structural analysis revealed that the phase transformation is triggered by on or off states of a unique intramolecular bond: long pair- π switch. In addition, programmability, the most important and fascinating feature of shape memory materials, is enabled as a result of co-existence of the two stable phases in a coherent crystal lattice. Furthermore, a prototype design of a two-way nano-actuator simulated solely by an external electric field is presented to demonstrate its potential in emerging smart material-based actuation technology. Providing graphene oxide crystal inherently exhibits many attractive properties similar to graphene (e.g. an atomic thickness, excellent mechanical properties and electric-responsive), the discovery of a two-dimensional shape memory graphene oxide may offer a myriad of opportunities

for developing exceptional micro/nano-electromechanical devices in the near future. The manuscript on this work has been accepted for publishing in Nature Communications and is included in this thesis chapter. [17]

1.3.4 Chapter 5: Two-way Quantum Mechanical Actuation of Graphene Oxide

This Chapter will discuss the observation that graphene oxide crystals with ordered epoxy groups exhibit electron injection-induced two-way quantum mechanical actuation. Inspired by the discovery of two-dimensional shape memory graphene oxide, [17] the search of bi-stable phases among graphene oxide crystals with different oxygen concentrations is applied to C_8O , $C_{12}O$ and $C_{16}O$ GO crystals in this study. An appropriate oxygen doping concentration leads to GO crystal with two stable phases (i.e. so-called meta-stable or stable). Upon electron injection up to -0.12 e per atom, quantum mechanical actuations of meta-stable and stable phases of GO crystals response complete oppositely. A maximum contraction of approximately 5 % was obtained for the stable phase of C_8O -asym GO, in the contrary, a huge expansion of 8 % was measured for the meta-stable phase of the same GO crystal. The work demonstrates that considerably large deformation in opposite two direction can be obtained from a single piece of GO crystal. A manuscript on this work has been submitted for review and is included in this chapter.

1.3.5 Chapter 6: Conclusion and Future Work

Chapter 6, a summary of the contribution to the field of smart materials-based actuation technology for MEMS/NEMS using two-dimensional graphene oxide by the research presented in this thesis is discussed. Finally, suggested future work to be carried out along with further potential contributions to the field of futuristic two-dimensional actuators is presented.

Chapter 2

Background, Theory and Method

2.1 Graphene Oxide

Similar to graphene, which is an atomic layer of carbon-atoms arranged in the honeycomb networks. Graphene oxide (GO) can be considered as a single layer graphite oxide. It has received tremendous research interests in the last decade, especially since the discovery of graphene in 2004. [48] Although GO is a very popular material in various research fields recently, graphite oxide was successfully fabricated more than one and a half centuries ago. [61] There are three major approaches to synthesis graphite oxide, namely Brodie, Staudenmaier and Hummers method. Due to highly toxic gas are generated (ClO_2) using Brodie and Staudenmaier methods, Hummers method is widely used to produce graphite oxide nowadays. However, it is important to note that graphite oxide synthesized using this method show variance depends on the oxidants used, graphite source, and synthesis conditions. [62] After the fabrication of graphite oxide, exfoliating of graphite oxide is necessary to produce monolayer GO sheet. A variety of thermal and mechanical exfoliation methods have been proposed to achieve GO for different purposes. For example, exfoliation of graphite oxide in water by sonication, [63] thermal exfoliation of graphite oxide to not only GO but also graphene. [64,65]

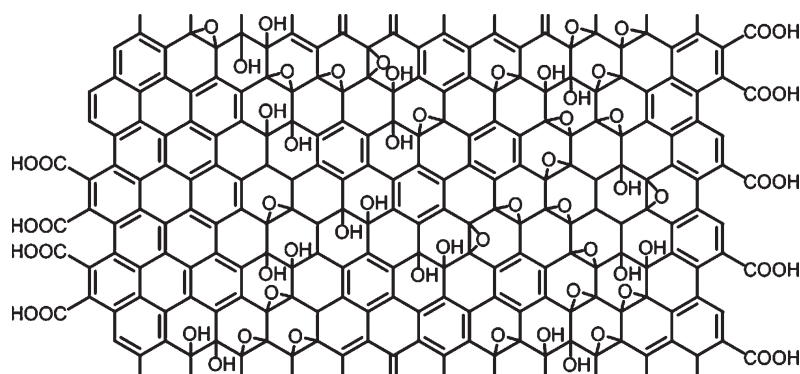


Figure 2.1: Structure of Graphene Oxide. Reprinted with permission from [2] Copyright (2010) American Chemical Society.

After the synthesis of GO, it is essential to determine the structure of GO because the different structural configurations of GO can lead to different mechanical and electric properties. [49,66] Extensive studies using the state-of-art spectroscopic and microscopic techniques have been employed to understand what and how oxygen functional groups distributed on the GO surface. For example, Cai et al. identified that epoxy and hydroxyl are the two major functional groups across the basal plane of GO using high-resolution solid-state NMR. [67] Ruoff's groups further investigated the distribution of the major functional groups, which suggest that small islands of pure epoxide and hydroxyls can exist. [68] While it is generally accepted that epoxy and hydroxyl groups are the two major oxygen functional groups on the basal plane of GO (Fig. 2.1), various GOs with homogeneous or inhomogeneous surface of oxygen functional groups on the basal plane are observed under different synthesis methods and conditions. [2,5,69–72] For instance, hydroxyl groups dominate the basal plane of GO under hydrogen rich environment. [71] On the contrary, GO with epoxy groups only can be fabricated under some well-controlled experimental conditions, like oxidation under ultra-high vacuum condition. [5]

2.1.1 Graphene Oxide with Ordered Epoxy Groups

Direct observations of ordered line patterns of epoxides on the basal plane of GO have been reported in experimental works. For example, atomic images of highly ordered GO crystal with linear arrangement of epoxy groups in a region that covers over 50 % of the total scanned area are captured by Pandey et al. using scanning tunnelling electron microscope. [73] Fujii and Enoki observed regularly spaced (about 5-10 nm) line defects on chemically oxidized graphene sheet using non-contact atomic force microscopic imaging. As shown in 2.2, these line defects with the length of more than 100 nm were identified as the linear arrangement of epoxy groups. [2] In addition, many theoretical studies have been carried out to provide the underlying formation mechanism of such GOs with linear patterned epoxy groups in experiments. [3,74–76] The general explanation is that the presence of epoxy group in the graphene basal plane severely strains the graphene lattice. The strain can be effectively reduced via the cooperative alignment of epoxy groups in rows, which results in a more stable structure namely GO with ordered epoxy groups. The linearly aligned epoxy groups tend to unzip the carbon-carbon bonds beneath the oxygen atoms and reduce the energy further by approximately 1.2 eV per bond, which was believed to cause the faulty lines in graphene observed via dark field optical microscope images. [74]

There are two possible configurations of GO with ordered epoxy groups that closely resemble the one observed in Fujii and Enoki's experiments. [2] They are named as symmetric (Sym) and asymmetric (Asym) GO as shown in Fig. 2.3 (a) and (b), respectively. The Sym-GO is defined as linear alignment of epoxy groups on one side of the basal plane, and Asym-GO is recognised if epoxide lines can be found on both sides. [76,77] Figure 2.3 shows GOs with the carbon to oxygen (C:O) ratio of eight. It is not a surprise that structural differences caused by the C:O ratio can lead to different electromechanical properties

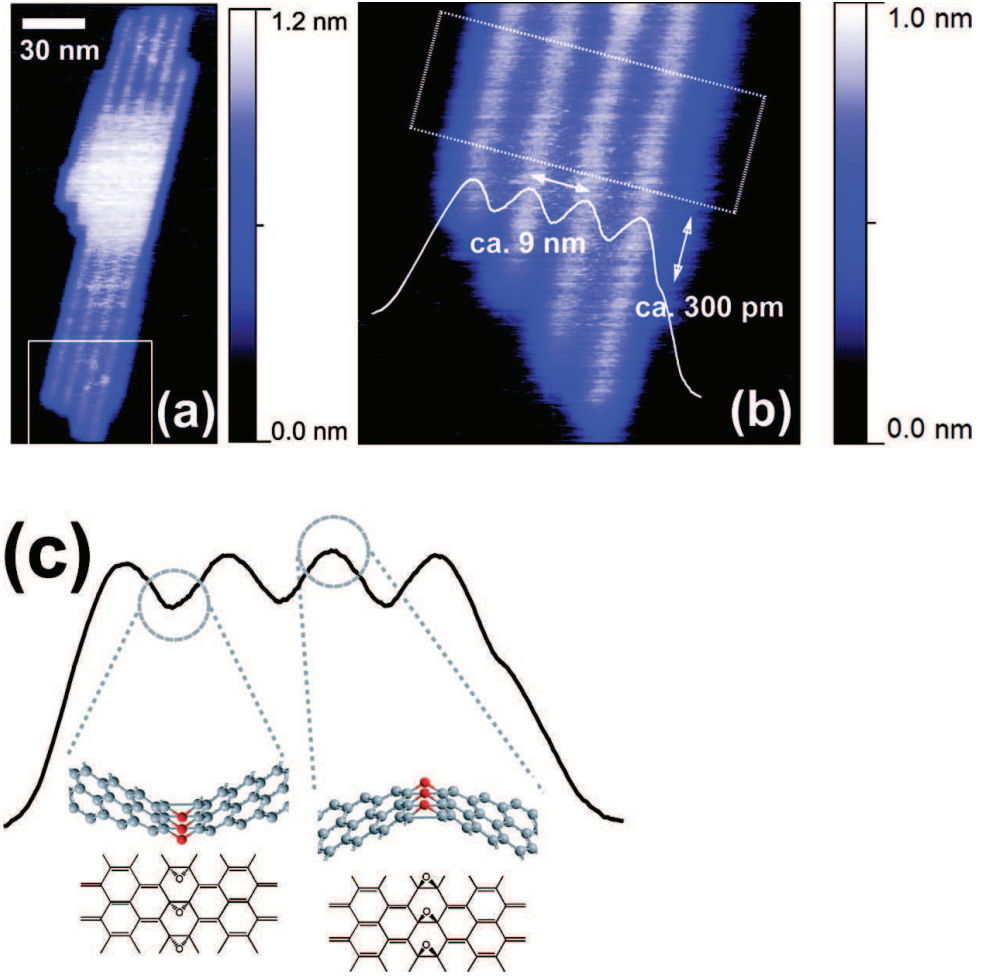


Figure 2.2: (a) NC-AFM image of the oxidized single graphene sheet with ordered wrinkles. (b) Magnified NC-AFM image of the area indicated by the white square in (a). Average height profile obtained for the dotted area indicated in (b) is superimposed on the image (z-scale bar = 300 pm). Imaging conditions: cantilever = NSC11, $\Delta f = -20$ Hz, $V_b = 0$ V. (c) Possible structural model of the linear epoxy groups for the observed height profile in (b) is shown. In the stick and ball model, carbon and oxygen atoms are gray and red, respectively. Reprinted with permission from [2] Copyright (2010) American Chemical Society.

of the GO crystals. Hence, C:O ratios of 2, 4, 8, 12, and 16 are studied in this thesis.

Based on current available technologies, some possible fabrication methods are proposed to synthesis GO with ordered epoxy groups in experiments. These methods are generally divided into two main steps.

Since the precondition of GO crystals studied in this thesis contain epoxy groups only, the first and prerequisite step is to achieve homogeneous functionalization of epoxy groups on the GO surface. Although Hummers method is most widely used at present, the chemical inhomogeneity of oxygen functional groups make this choice obviously unfavourable for this case. Fortunately, there are two alternative methods in order to obtain

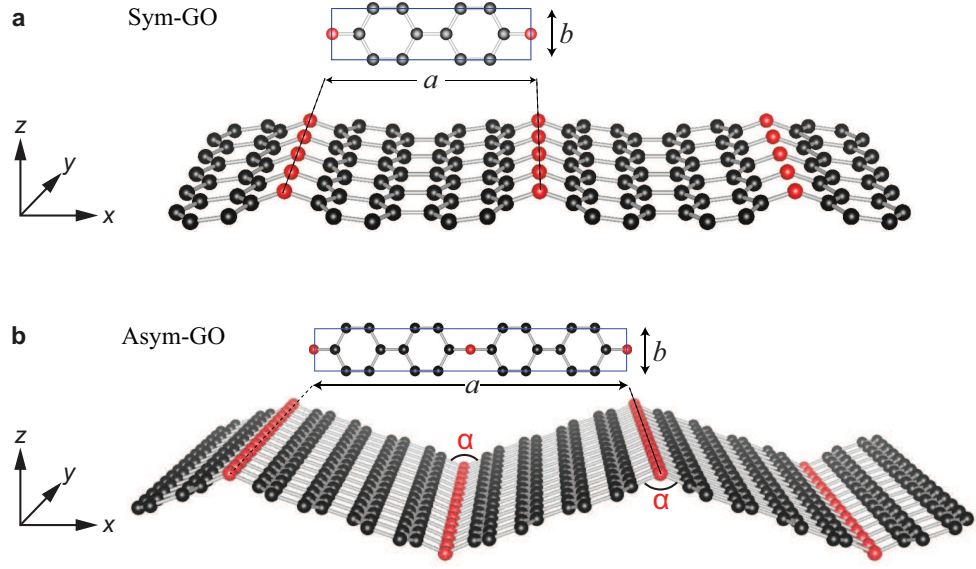


Figure 2.3: Crystal structure of symmetric (a) and asymmetric C₈O (b) with a and b as the lattice constant in x and y -axis. Black and red spheres represent the carbon (C) and oxygen (O) atoms, respectively. Angle α measures the bond angle of oxygen atom and its two neighbouring carbon atoms. The symmetric C₈O unit cell contains 8 carbon atoms and 1 oxygen atom, and the asymmetric C₈O unit cell contains 16 carbon atoms and 2 oxygen atoms.

the homogeneous functionalization. Hossain et al. reported that uniform functionalization of epoxy groups can be achieved via oxidation of epitaxial graphene using atomic oxygen under ultrahigh-vacuum condition. Additionally, it is crucial to notice that oxidation of the graphene is completely reversible via thermal annealing or injection of electrons from STM tip. [5] Another possible option is to use vacuum thermal annealing process. Mattson et al. found the only epoxy groups were remained and these epoxides tended to form an ordered line pattern. [70]

Given that GO with only epoxy functional groups can be achieved, the next goal is to form linear alignment of the epoxy groups on the basal plane of GO crystal. Previously, studies on the formation mechanism of linear epoxy groups have been reported for the purpose of unzipping graphene sheets into GNRs. [2–4, 78] These studies provide many solid evidences to support that the stability of GO with ordered epoxy groups, even take the finite temperature effects into consideration. For instance, a theoretical study by Huang et al. suggested that GO with well-ordered linear pattern of epoxy groups is the ground state (or most stable) structure among approximately 17000 different GO structures tested. [72] In addition, the initial formation of linear epoxide is found attract and trap nearby oxygen adatoms to diffuse to the end of epoxide, which leads to further growth of the epoxy lines. However, it is energetically more favourable for the ordered epoxy lines to grow in three directions of the graphene symmetry (Fig. 2.4 (e)). [3]

To match the structure of GO with ordered epoxy groups as shown in Figure 2.3, it is thus necessary to control and to guide the growth direction of the epoxy lines. One possible approach is to transfer graphene onto a flexible substrate and then stretching or bending the substrate before oxidation. The applied stress or strain in graphene layer not

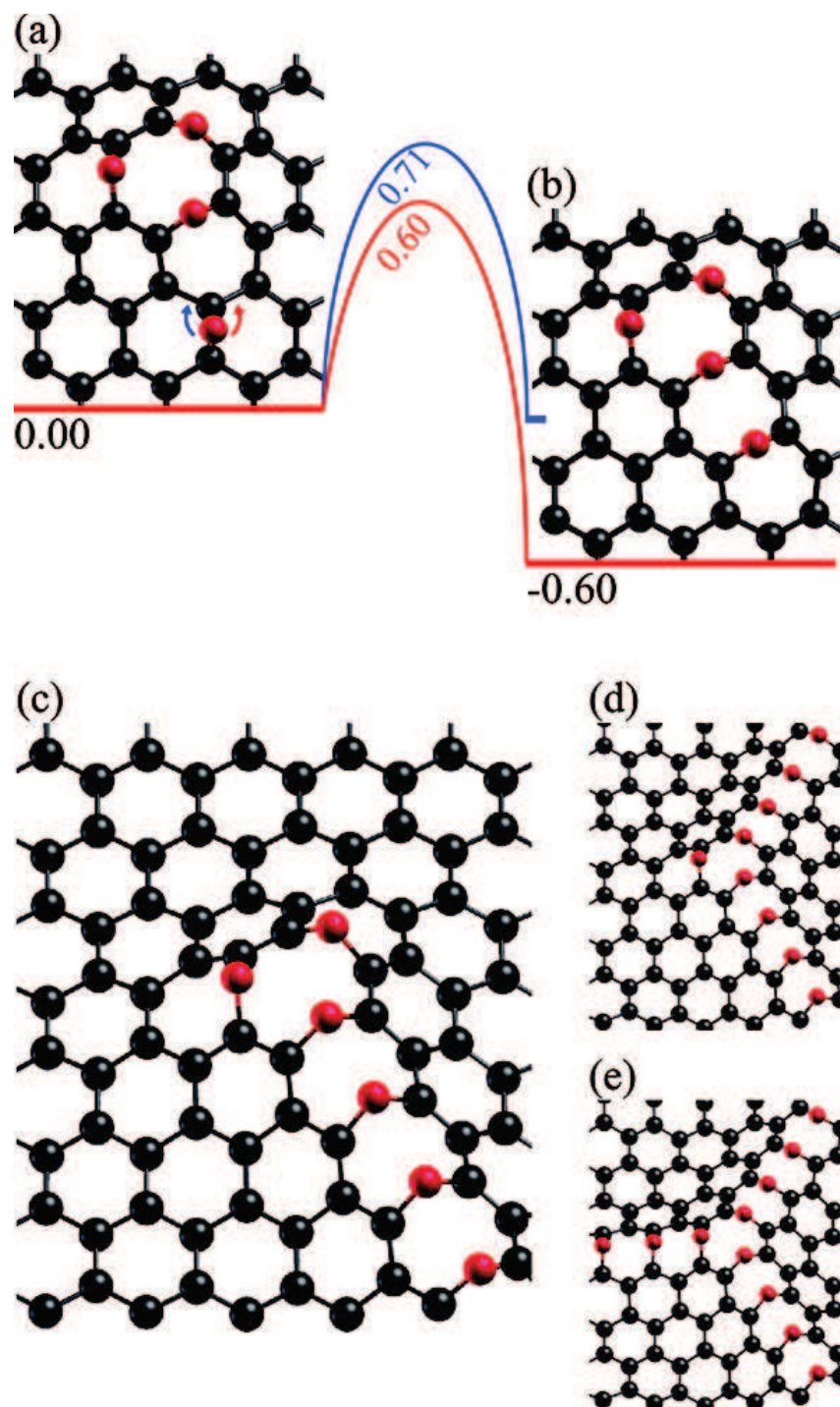


Figure 2.4: (a,b) Energetic for the formation and growth of an extended linear defect from the O diffusion to the NNN ET trimer (c,d). Schematic representation of further nucleation and growth of O-driven unzipping in graphene. Reprinted with permission from [3] Copyright (2012) American Chemical Society.

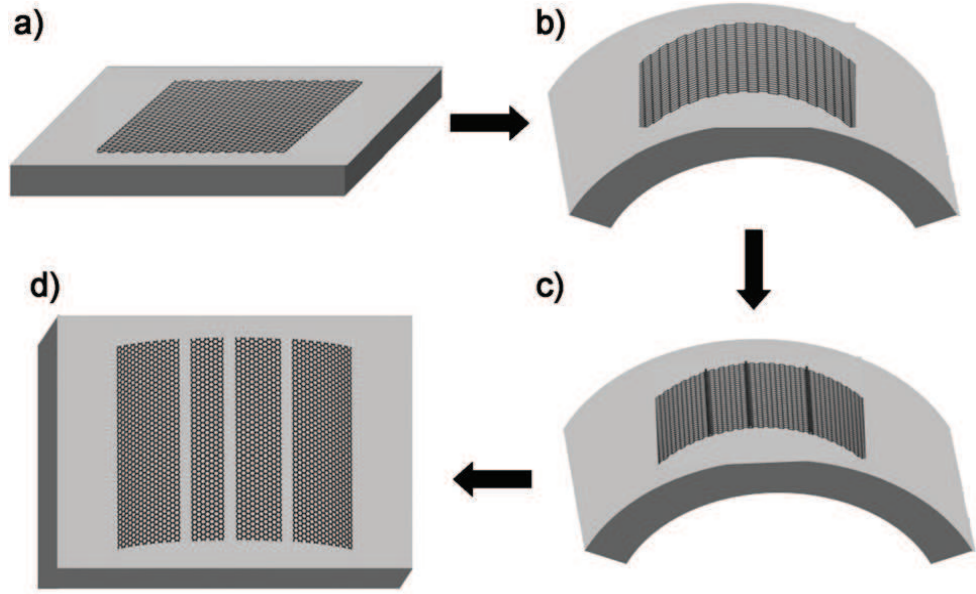


Figure 2.5: (a) Graphene monolayer transferred to a flexible polymer substrate. (b) The polymer substrate is bent and thus strain is exerted on the attached graphene sheet. (c) Annealing of adsorbed O atoms forms parallel epoxy chains on the graphene. (d) Under further oxidation, the graphene layer is unzipped into nanoribbons. Note that further oxidation in (d) is not necessary for this study. Reprinted with permission from [4] Copyright (2011) John Wiley and Sons.

only breaks the symmetry of the honeycomb graphene but also reduces the reaction energy barrier, hence serves as an external guide to promote the growth of epoxy lines. Figure 2.5 (a-c) indicates that parallel linear alignment of epoxy lines can be obtained using this concept. [4]

Similarly, well-ordered linear epoxy groups could also be achieved by periodic rippling of the graphene layer from mechanical compression. Specifically, periodic rippling of graphene can be generated upon the applied mechanical compression. The residual strain on the ripple ridges would make the C-C bond more reactive to oxygen adatom during oxidation. Subsequently, linear aligned epoxy groups could be allocated to the ripple ridges, which lead to the formation of linear epoxides pattern. The rippling wavelength can be precisely controlled down to approximately 1 nm range. [79]

Furthermore, as mentioned previously, Hossain et al. suggested that both thermal annealing and injection of electrons from STM tip can be used to fully inverse the oxidation process. It means that the chemisorbed oxygen atoms (or epoxy groups) can be selectively desorbed or relocated on the graphene surface follow a pre-determined design by STM tip (Fig. 2.6 (c)). This enables highly desired nanopatterning of epoxy groups at atomic precision using current available lithographic technologies. [5] Hence, it is plausible to use STM tips to pattern parallel epoxy groups and subsequent oxidation under high

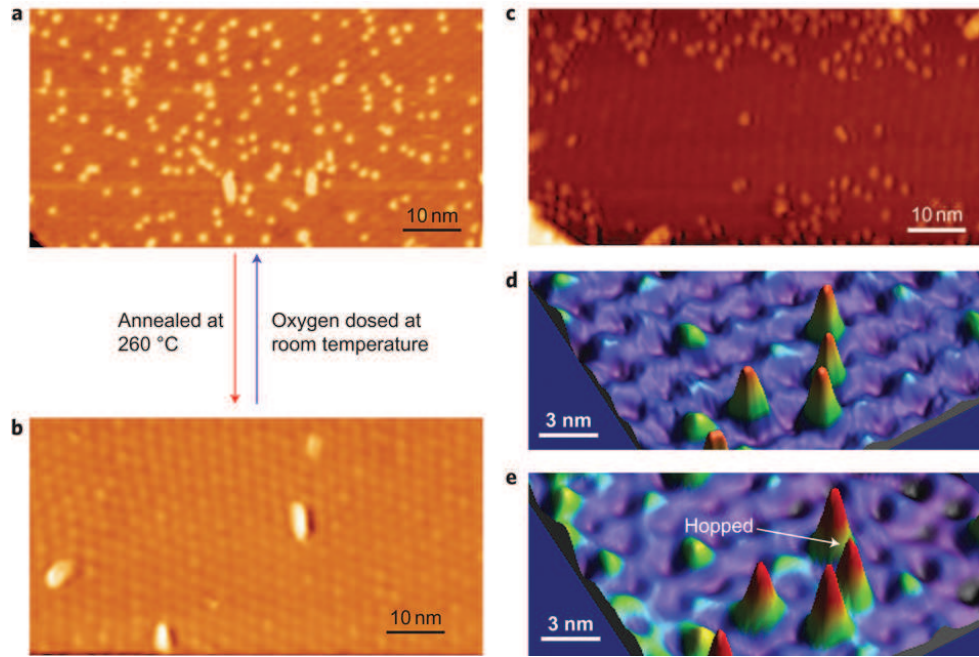


Figure 2.6: (a,b) STM images of UHV epitaxial graphene before (a) and after (b) annealing at 260 °C. (c) STM image showing a region of the UHV oxidized epitaxial graphene surface where chemisorbed oxygen has been reversibly desorbed by injection electrons from the STM tip at a sample bias of +4.0 V and tunnelling current of 1 nA. (d,e) STM images before (d) and after (e) hopping of chemisorbed oxygen on epitaxial graphene at room temperature. The displaced oxygen adatom is indicated in (e). All STM images were acquired at a sample bias of +2.4 V and a tunnelling current of 50 pA. Reprinted by permission from Macmillan Publishers Ltd: Nature Chemistry, [5] Copyright (2012).

vacuum (UHV) condition will lead to spontaneous growth of epoxy lines.

To conclude with, GO crystals with ordered epoxy groups have been observed experimentally, many theoretical works have been reported to understand the structural mechanisms, and they could be synthesized using current available technologies. Thus, it is necessary to investigate their electromechanical properties for two-dimensional actuators.

2.2 Piezoelectric Effect

Piezoelectricity can be observed in crystals which lack inversion symmetry. The root of the word 'piezo' means 'pressure' in Greek, hence piezoelectricity implied 'pressure electricity'. Upon and applied external mechanical stress, piezoelectric materials can generate electrical charges on the surface of the crystal. This is the direct piezoelectric effect discovered in single crystal quartz by the Curies brothers in 1880. Conversely, a mechanical strain can be induced by applying an external electric field. This is termed as converse piezoelectric effect, which is discovered by Gabriel Lippmann in 1881. [36,37] Originally, piezoelectric materials are all crystals (such as quartz and Rochelle salt). Until 1947, a new piezoelectric material namely barium titanate (BaTiO_3) was discovered by R.B. Gray (the father of piezoceramics). [80] This discovery directly led to the rapid development of inorganic piezoelectric materials (piezoelectric ceramics). For example, lead zirconate titanate (PZT), one of the most commonly used piezoelectric material since its discovery by B. Jaffe in 1954. [81] Piezoelectricity is not limited to inorganics, another important type of piezoelectric material is piezoelectric polymers. Such as the most widely used semi-crystalline piezoelectric polymer namely polyvinylidene fluoride (PVDF) artificially synthesized by H. Kawai in 1969. [82] More recently, the development of lead-free piezoelectric ceramics and piezoelectric composite (e.g. mixing piezoelectric polymer with ceramic to combine the advantages of both materials) has attracted extensive attentions due to the environmental and performance requirements. [37]

The piezoelectric effect follows a linear relationship between electric field and mechanical stress or strain. This unique phenomenon enables its widely usage for various electromechanical devices, such as sensor (from *direct piezoelectric effect*), actuator (from *converse piezoelectric effect*), acoustic transducers and energy harvesters. [83] To understand and describe the mechanical/electrical coupling in such devices, the fundamental knowledge on piezoelectric coefficients is necessary.

Piezoelectric strain coefficient d represents the magnitude of the induced strain by an external electric field. It has the unit of coulombs per newton (Cm^{-1}) or meters per volt (mV^{-1}). Naturally, this is the key coefficient for actuator applications. On the other hand, the electric field generated upon an external stress is represented by the piezoelectric voltage constant g , which serves as an important parameter when using piezoelectric materials for sensors. [36,37] While there are other piezoelectric coefficients defined for different purposes (for example, piezoelectric stress coefficient e and inverse piezoelectric strain coefficient h), piezoelectricity related work only considers the piezoelectric strain coefficient d for comparison reason between different piezoelectric materials since the primary aim of this thesis is to investigate electromechanical properties of graphene oxide as advanced actuators.

Two equations based on thermodynamics potential and energy exchange principles can be used to describe piezoelectricity. [84]

$$D_i = \varepsilon_0 \varepsilon_{ij}^\sigma E_j + d_{ij} \sigma_j \quad (2.1)$$

$$\delta_I = S_{IJ}^E \sigma_J + d_{Ii} E_i \quad (2.2)$$

where D is the electric displacement; E is the electric field; σ is the stress; δ is the strain; ε_0 is the free space electric permittivity; d is the piezoelectric strain coefficient; ε^σ is the material's dielectric constant at a constant stress and S^E is the material's mechanical compliance matrix; I and J are indices with values from 1–6 while i and j are indices from 1–3. D and E are (3×1) tensors indicating the three coordinate direction x , y and z . σ and δ are (6×1) tensors indicating the normal stresses or strains (elements from 1–3) and shear stresses or strain (elements from 4–6).

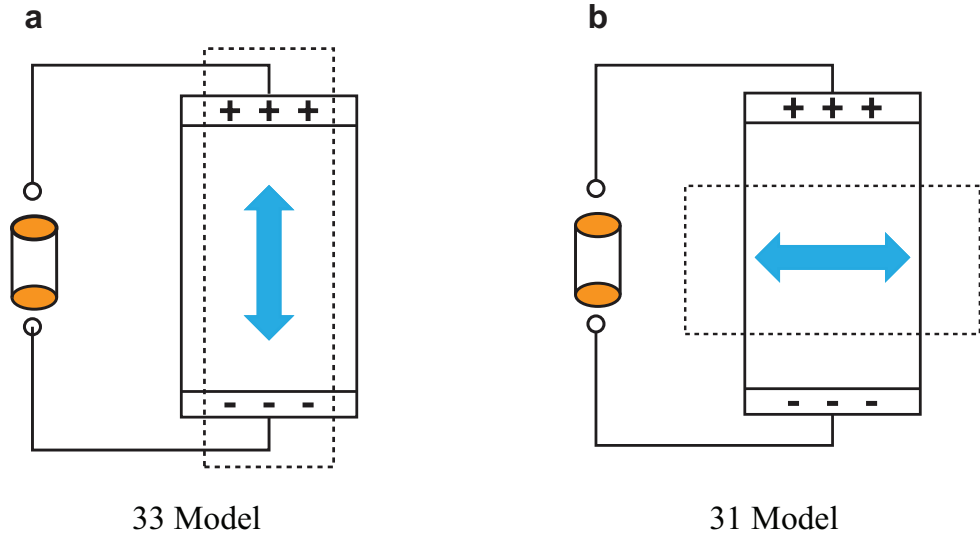


Figure 2.7: Piezoelectric transduction (a) 33 model (b) 31 model.

The piezoelectric strain coefficient d_{ij} is a (3×6) tensor, which defined as the induced mechanical strain of index J when the external electric field is applied in direction i . There could be a total 18 independent d values. However, many of them are zero in most piezoelectric materials (due to crystal symmetry), which greatly reduces the number of values of interest. [84, 85] Subscripts 4–6 represent the mechanical shear. Although it is possible to induce shear strains upon the applied electric field, these d values are not significant for piezoelectric actuators. Generally, piezoelectric strain coefficient d_{33} and d_{31} are used to compare the piezoelectric behaviours in electromechanical transducers. The corresponding two popular and commonly used transduction models, namely 33 and 31 model, are graphically demonstrated in Fig. 2.7. For actuator applications, the induced strain upon an applied electric field can be represented by the following equations:

$$\delta_1 = d_{31} E_3 \quad (2.3)$$

$$\delta_3 = d_{33}E_3 \quad (2.4)$$

where the d_{31} coefficient implies the induced mechanical strain in a direction perpendicular to the direction of the applied electric field and the d_{33} coefficient describes the induced mechanical strain in the same direction of the applied electric field.

2.2.1 Piezoelectricity at Nanoscale

In the past two decades, the combination of rapidly growing nanotechnology and piezoelectricity lead to many interesting one-dimensional, two-dimensional and zero-dimensional piezoelectric nano-structures based on commonly available piezoelectric materials. [86] Firstly, numerous one-dimensional piezoelectric nano-structures have been proposed in the form of nanowires or nanofibers (i.e. typically with a character dimension less than 100 nm and a length more than 1 mm) to enhance the piezoelectric effect and mechanical properties. For example, Zinc Oxide (ZnO) nanowires, Aluminium nitride (AlN) nanowires, PZT nanofibers, BaTiO₃ nanowires and PVDF nanofibers. [87–91] Among them, ZnO nanowires has attracted most interest thanks to the successfully utilisation of ZnO nanowire for self-power nanogenerator (conversion of mechanical energy into electricity). [87] Moreover, two-dimensional piezoelectric nano-structures (i.e. nanofilm with a nanometre thickness) have been reported. Commonly used piezoelectric nanofilms are PZT nanofilms, ZnO nanofilms, and BaTiO₃ nanofilms. Similarly, the mechanical and piezoelectric are enhanced at nanoscale. [92,93] Recent interests on piezoelectric nanofilms are focus on transfer them onto flexible substrates for the purpose of energy harvesting. [94] Furthermore, the zero-dimensional nanoparticles are fundamental the piezoelectric nanocomposites of other types of piezoelectric nano-structure, which have received extensively attentions in recent years. The nanocomposites by adding inorganic piezoelectric nanoparticles into piezoelectric polymers are popular choices to achieve desired electromechanical properties. For example, the incorporation of ZnO nanoparticles into the piezoelectric polymer matrix (PVDF thin films) enhances the piezoelectricity of the bulk film while preserving the mechanical flexibility of the polymer. [95]

When consider utilizing smart material for miniaturized actuators, electrostatic forces between charged surfaces have been implemented to actuate MEMS/NEM. [96–98] Despite this technology has successfully provided many new application possibilities, the electrostatic approach is however limited because continued down-scaling of such electromechanical devices to NEMS requires the increase of integration density, faster actuation, larger displacement and more powerful actuating elements (as discussed in Chapter 1).

Piezoelectric materials, on the other hand, possess two extremely attractive advantages in continuing down-scaling of electromechanical devices to nanoscopic scale. First and most importantly, piezoelectric materials are much more favourable in downwards scaling. For example, wurtzite-structured crystals (e.g. AlN) shows bulk piezoelectric response even down to tens of nm range. In addition, piezoelectric effect of ferroelectric materials

remains validate in nanofilms only a few unit cells in thickness. Note that piezoelectric response occurs in all ferroelectric materials. [99] The decrease of size dimension also associated with the scaling of energy density, which enables the possibility of generating usable piezoelectric actuation with very small volume nano-structures. This further leads to the decrease of complexity in NEMS, thus results in higher integration density. [85] Secondly, piezoelectric actuators have significantly higher power density than the electrostatic actuators thanks to the linear electromechanical coupling of piezoelectric materials. [36] On top of the high power density, piezoelectric materials in form of thin films (i.e. piezoelectric thin films) exhibit the free space electric permittivity ϵ_0 (Equation 2.1) exceeds that of air by factors of about 10–1000. [100] As a consequence, the required electric field (or driving voltage) to operate piezoelectric actuators to achieve a given displacement in structure of the same stiffness typically drop by at least an order of magnitude. [85]

Overall, it seems like that the piezoelectric thin films, especially nanofilms based on inorganic piezoelectric materials, are promising candidate for further development of piezoelectric actuators in NEMS. Nevertheless, there are two major constraints may significantly affect the piezoelectric response of these thin films. Firstly of all, the preparation of many nanofilms involves the transformation of films on to flexible substrate. This process may cause unwanted tensile or compressive stress due to mismatch between the film and the substrate, which may result in a higher electric field for inducing the piezoelectric response. [101, 102] More importantly, there exist a critical film thickness below which the ferroelectricity (thus piezoelectricity) would disappear. [103] This well-known phenomenon strictly restricts the development of nanoscale electromechanical devices with thickness lower than the critical value.

A question arises: *Will atomically thin materials exhibit piezoelectric effect* so that electromechanical devices could be scaled down to the thickness of a single atomic unit cell.

2.2.2 Atomically Thin Piezoelectric Materials

The answer is yes. The original investigations of piezoelectricity on atomically thin materials were started with density functional theory calculations. Many commonly studied two-dimensional materials including monolayer transition metal dichalcogenide (TMDC) (e.g. MoS₂, MoSe₂, MoTe₂, WS₂, WSe₂ and WTe₂) and hexagonal BN are predicted to exhibit piezoelectricity. The calculated piezoelectric strain coefficients d range from 0.6 pmV⁻¹ for monolayer BN to 2–10 pmV⁻¹ for the dichalcogenides. [104] While the piezoelectric strain coefficients of these two-dimensional materials still smaller than that of for lead zirconium titanate, some of these two-dimensional materials show similar or stronger piezoelectric coupling in comparison to conventional bulk piezoelectric materials, such as wurtzite structures. [105] The discovery of strong piezoelectricity in these two-dimensional materials greatly encourages researcher all over the world to explore piezoelectric two-dimensional materials experimentally. [106]

Indeed, experimental observations of two-dimensional piezoelectric materials have been reported recently. [107–109] Hangyu et al. reported a free-standing single layer of molybdenum disulphide (MoS₂) in 2014. The measured piezoelectric coefficient of e_{11} equals to 2.9×10^{-10} Cm⁻¹, which agrees well with previous simulation prediction. [107] In addition, MoS₂ flakes with only odd number of atom layers can produce piezoelectric voltage and current output upon the cyclic stretching and releasing. [108] Moreover, anomalous piezoelectricity has been studied in two-dimensional graphene nitride (C₃N₄) nanosheets. Despite C₃N₄ should be a non-piezoelectric material due to inversion symmetry, the regularly space triangular hole (non-centrosymmetric) in C₃N₄ nanosheet can lead to piezoelectric response. The predicted piezoelectric coefficient of e_{11} equals to 0.758×10^{-10} Cm⁻² is significantly larger than that of the commonly compared α -quartz. [109]

2.2.3 Graphene-based Piezoelectric Materials

For pristine graphene, however, the short answer is no. This is due to pristine graphene exhibits inversion symmetry (i.e. point group of $6/mmm$) as discussed at the beginning of this section, a key characteristic of piezoelectric material is that they belong to a non-centrosymmetric point group (a material without an inversion symmetry). [7] Graphene is an intrinsically non-piezoelectric material, and the inversion symmetry element must be broken in order to induce piezoelectricity.

Fortunately, recent studies have successfully demonstrated that piezoelectricity can be engineered into intrinsically non-piezoelectric graphene. There are two different approaches to achieve piezoelectric graphene. Firstly, the concept of all dielectric materials are capable of producing polarization under a non-uniform strain or strain gradients due to flexoelectric effect was used to induce piezoelectricity in graphene nanoribbons (GNRs) by Swaenil et al. in 2012. [6] By introducing specific in-plane defects, they proposed that even under the application of uniform stress, differences in material properties at the interface will result in the presence of strain gradient. As long as certain symmetry rules

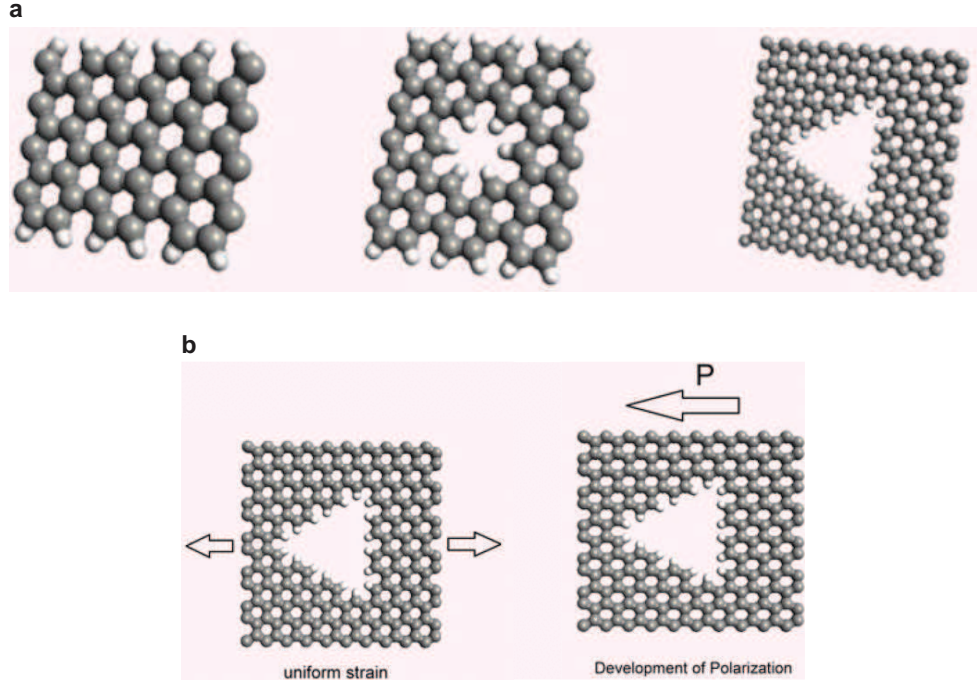


Figure 2.8: (a) Pristine GNR, circular hole GNR, and graphene sheet with triangular hole. The white colored atoms refer to hydrogen atoms which mark the termination of GNR. (b) The development of polarization for triangular-hole-graphene sheet under the action of strain. Reprinted from [6] with the permission of AIP Publishing Copyright (2012)

are followed, the net average polarization will be non-zero and the GNRs with holes will exhibit an over electromechanical coupling under uniform stress behaving like a piezoelectric material. While the pristine graphene and GNRs with circular porous did not show any piezoelectric behaviour, graphene sheet containing triangular holes developed a large amount polarization under the action of mechanical strain. (Fig. 2.8)

The second approach to break the inversion symmetry of pristine can be achieved via adatom adsorption onto the graphene surfaces (Fig. 2.9). An external electric field applied perpendicular to the graphene sheet induces an equibiaxial strain in the plane of the sheet. Comparing to pure graphene, it is clear to see that these adatoms (i.e. Li, K, H, and F) on the surface successfully break the inversion symmetry and changes the electromechanical properties. This leads to a linear electromechanical coupling between applied external electric field and induced strain (Fig. 2.9 (c)), the slope of which gives the piezoelectric coefficient d_{31} . The calculated maximum piezoelectric strain coefficient d_{31} of $3.0 \times 10^{-1} \text{ pmV}^{-1}$ is comparable to a theoretical value for wurtzite boron nitride $3.3 \times 10^{-1} \text{ pmV}^{-1}$. The piezoelectric coefficients have also been calculated to show that the piezoelectric performance of engineered piezoelectric graphene is comparable to common piezoelectric materials. [7]

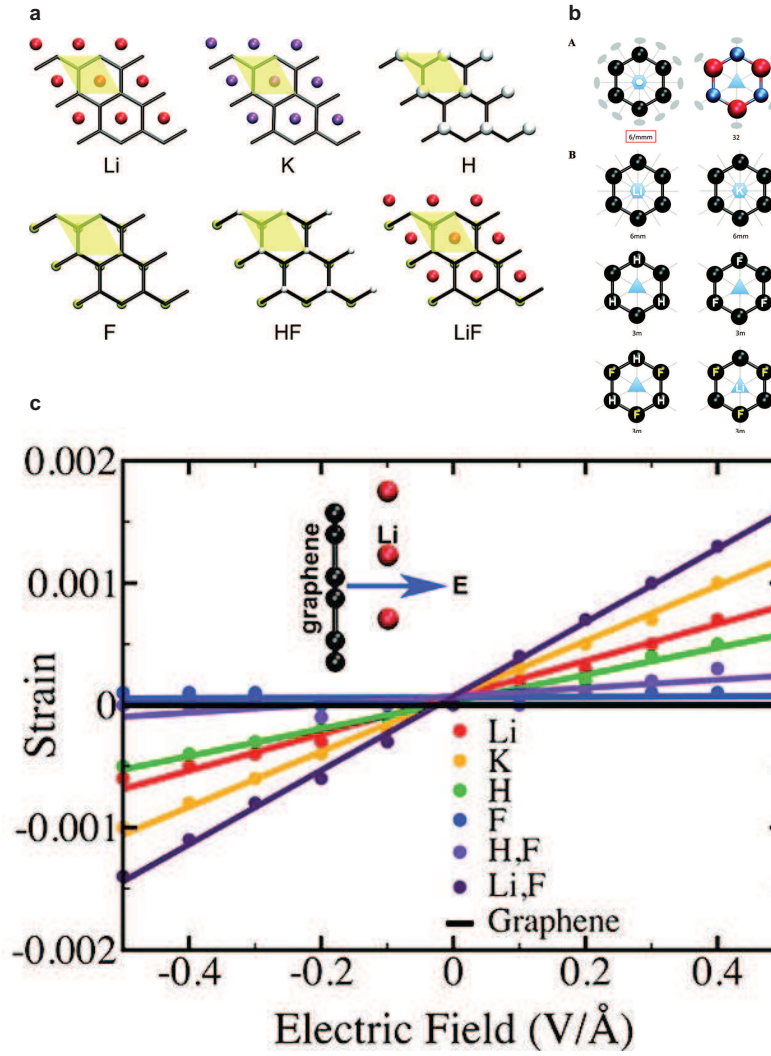


Figure 2.9: (a) Unit cells for each of the adatom cases studied are highlighted in yellow. Periodic boundary conditions are employed in all cases. (b) Point group symmetry of lattice unit cells for each case of atom adsorption considered here. In all cases, inversion symmetry is destroyed, leading to piezoelectricity. (c) An external electric field applied perpendicular to the graphene sheet induces an equibiaxial strain in the plane of the sheet. This results in a linear relationship between the electric field and strain at low fields, the slope of which gives the d_{31} piezoelectric coefficient. Reprinted with permission from [7]. Copyright (2012) American Chemical Society.

Given the bright prospects that intrinsic piezoelectric properties are found in many two-dimensional materials both theoretically and experimentally along with the ability to engineer piezoelectricity within pristine graphene utilising different approaches, it becomes natural to investigate the potential of using GO with ordered epoxy groups (discussed in 2.1.1) as atomically thin piezoelectric materials for advanced actuators in NEMS. The exploration of piezoelectric properties of graphene oxide is detailed in Chapter 3.

2.3 Shape Memory Effect

As an important member of the stimuli-responsive smart materials family, shape memory materials (SMMs) are characterized by the ability to recover their original shape from a significant or quasi-plastically deformation upon an appropriate external stimulus. [40–42] This interesting shape memory phenomenon occurs as a result of reversible phase transformation and it is well-known as the shape memory effect (SME).

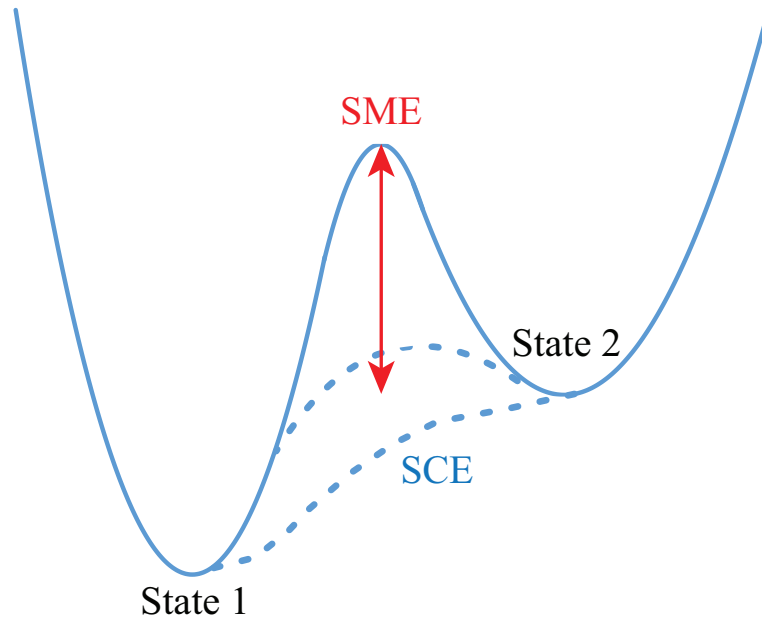


Figure 2.10: Comparison between SME and SCE from an energy point of view.

In many occasions, SME is discussed with other stimuli-responsive shape change effect (SCE), that is the phenomenon of shape change materials (SCMs) return its original shape either instantly or gradually as soon as the applied stimulus is removed. A very important feature namely programmability is generally employed to distinguish SMMs from SCMs. Specifically, it means that SMM can be programmed or fixed into different temporary shapes. Figure 2.10 explains this key feature from an energy point of view. Clearly, the difference between SME and SCE is due to the magnitude of energy barrier between state 1 and state 2, in which SME has a high energy barrier (indicated by the red arrow) and SCE has a very low or negligible barrier (represented by the dashed lines) between these two states. Consider state 1 as the original shape, the presence of external stimulus leads to the phase transformation from state 1 to state 2 thanks to the SME. Upon the removal of the external stimulus, SMM is programmed or fixed at the temporary shape (i.e. state 2) because additional energy or driving force is required to overcome this high energy barrier and return to its original state. On the other hand, SCM requires no extra energy since there is no energy barrier or the energy barrier is very small. The original state 1 of SCM can be realised instantly or gradually. [43, 110, 111] There is no programming or shape fixing step in SCE.

2.3.1 Shape Memory Materials and Shape Memory Mechanisms

The first discovery of SMA need to be traced back to Arne Olander's work in 1932. [112] However, its great potential was not recognised by public until SME was uncovered in nickel-titanium (NiTi) alloy by William Buehler and Frederick Wang in 1962. [113] After more than 50 years of development, many different types of NiTi-based, [114, 115] iron-based(Fe) [116] and copper-based [117, 118] SMAs have been implemented in various fields, range from aerospace industry to mini actuator in micro-robotics. [32, 119–121] Note that most SMAs are thermal-responsive and NiTi-based SMA is the most favourable choice due to intrinsically drawbacks of other types like instability, impracticability and poor thermos-mechanic performance. [8, 122, 123]

The shape memory mechanism of SMA need to be explained from the prospect of phase transformation (or martensitic transition). Fundamentally, there are two phases, namely martensite and austenite, exist in SMAs. Figure 2.11 shows the schematic illustration of thermal induced SME in SMA as a result of phase transformation. The temperature at which the phase transformation takes places is named the transition temperature T_{trans} . Consider martensite as the original shape, SMA is in its martensitic phase when the temperature is above the room temperature but below T_{trans} . In this range, the alloy can be easily deformed, and shape fixing can be obtained. Upon the heating, phase transformation can occur and the alloy is in its austenitic phase when temperature is above

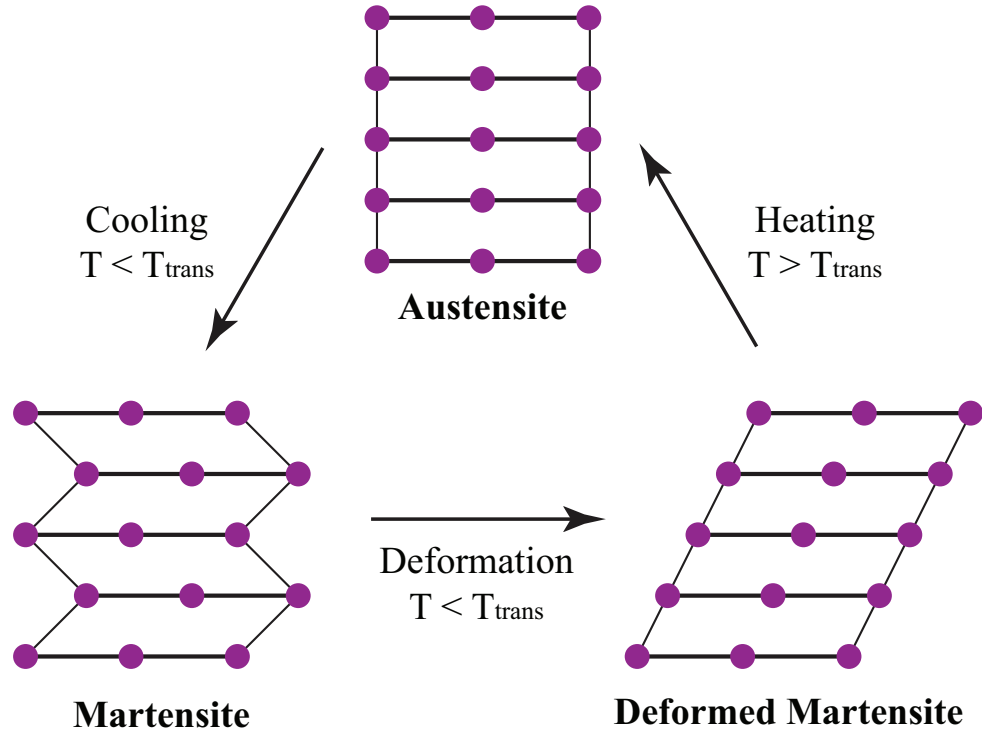


Figure 2.11: Schematic of shape memory mechanism for thermal-responsive SMA.

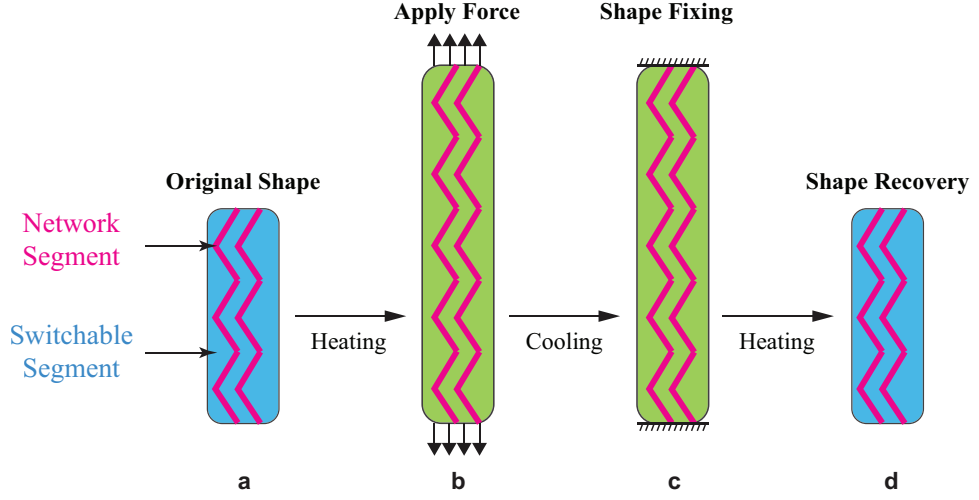


Figure 2.12: Schematic of shape memory mechanism for thermal-responsive SMP.

T_{trans} . Interestingly, cooling the SMA (i.e. below T_{trans}) leads to the second phase transformation from austenite to martensite, which obviously indicates the recovery of original shape. [8, 40, 42, 116]

Another commonly used SMM is shape memory polymer (SMP). Similar to SMA, the SME of most SMP is triggered by the temperature change. [123–125] However, the underlying shape memory mechanism of SMPs must consists a dual-segments system, which is significantly different from SMAs. Described above. The dual-segments based shape memory mechanism is presented in Fig. 2.12, the *network segment* is usually hard in order to maintain or recover the parent (or original) shape of the polymer. The *switchable segment* can be soft or ductile, that is the stiffness of SMP depending on the presence of a right stimulus. [126] Taking the thermal-responsive SMP as an example, Figure 2.12 (a) indicates that the polymer remains at its original shape when the temperature is below T_{trans} . Heating the polymer above T_{trans} , the switchable segment is activated so that the polymer can be easily deformed if a stress is applied as shown in Fig. 2.12 (b). Cooling the polymer below T_{trans} results in the shape fixing at this deformed shape even the applied stress is completely released, in another word, the programming to a temporary shape is obtained (Fig. 2.12 (c)). Finally, the temporary shape constraint can be removed by heating up the polymer again above T_{trans} . Therefore, shape recovery is achieved as illustrated in Fig. 2.12 (d). [42, 43, 126]

Depending on the selection requirements for different applications, SMAs and SMPs have their own advantages and disadvantages constitutionally. In general, SMAs inherently exhibit excellent mechanical properties, which result in high force/stress output. Nevertheless, the theoretical recoverable cycle strain is relatively small (approximately up to 8 %). [8] The performance can degrade due to fatigue and reliability issues of the alloys. Moreover, permanent plastic deformation caused by overstretching or overheating can lead

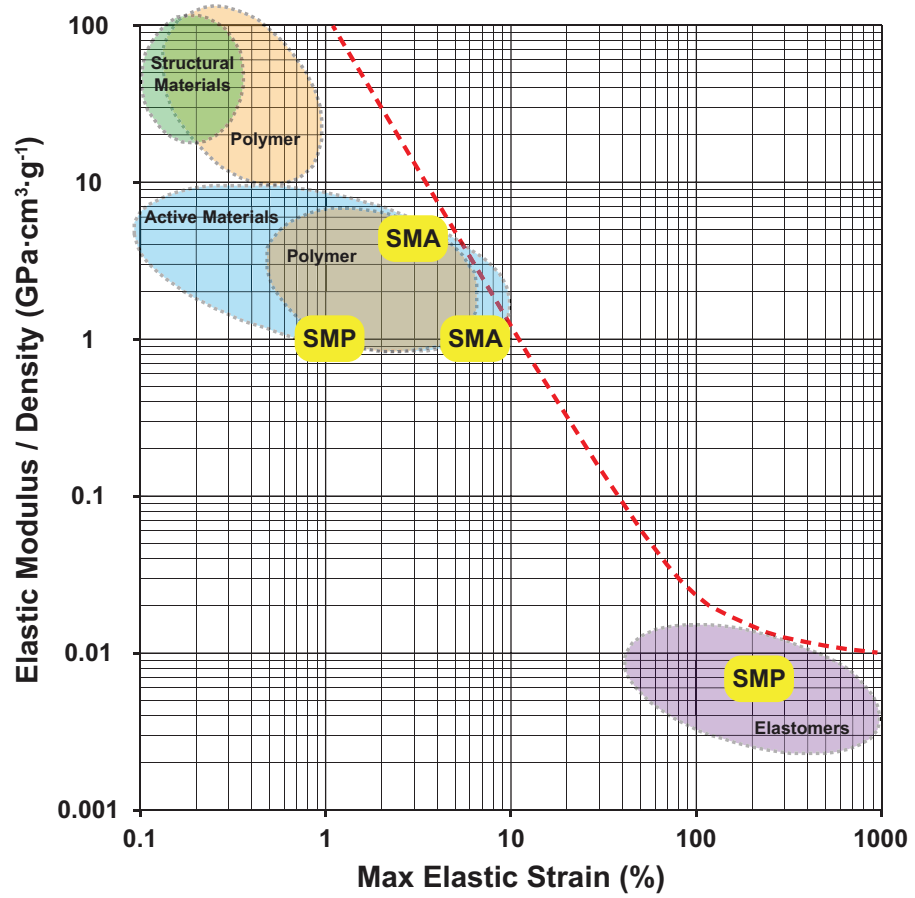


Figure 2.13: Specific modulus (ratio of elastic modulus over density) as a function of maximum recoverable elastic strain for common actuation materials (including SMA and SMP highlighted in yellow). Adapted from references [8,9].

to the failure of SMAs. Hence, it is critical to note that the actual usable strain of SMAs is mostly restricted to 4 % or less. [127] Although ultralow-fatigue SMA films have been reported recently, the strain output has to be compensated considerably. [128] SMPs, on the other hand, possess a few benefits over SMAs such as lower density (i.e. $0.9\text{--}1.25\text{ gcm}^3$) and easier in processing and in tailoring properties. The most noticeable advantage of SMPs is large attainable strain up to 400 %. However, their poor mechanical properties (i.e. lower stress/force output) have hugely limited the potential of using SMPs in real-life. [43,124]

An ideal actuator should be able to generate large deformation while maintain excellent mechanical properties for high power output and small in density for easier tailoring and integration. Thus, the specific modulus (ratio of elastic module over density) are the two major performance parameters. The actuation performance based on these parameters for current available materials including SMMs (highlighted in yellow) is shown in Fig. 2.13. Basically, an actuation material with high strain output usually has a very small specific modulus, while excellent mechanical properties always associated with small

deformation. The red dashed line indicates the upper bound for conventional actuation materials. [9] The development or discovery of new materials above this limitation line is necessary for futuristic actuator.

2.3.2 Multi-shape Memory Effect

Thanks to a much larger strain performance and a wider shape recovery temperature range, it is possible for SMPs to have more than one temporary shapes in each shape memory cycle. This phenomenon is classified as multi-shape memory effect (multi-SME). Despite the first multi-SME (or triple-SME with two temporary shapes) was only revealed in 2006 by Lendlein, [129] most research groups active in SMPs have reported multi-SMPs. [130–133] Obviously, multi-SME can provide much better controllability and programmability to enable much flexible shape morphing technology. [42, 43]

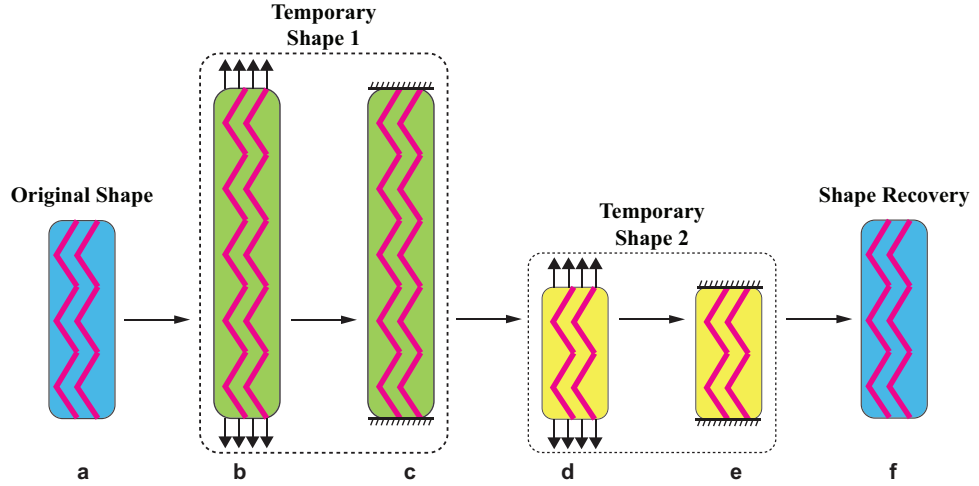


Figure 2.14: Schematic of multi-shape memory effect for thermal-responsive SMP.

The fundamental shape memory mechanism is not different from traditional SME, where the phase transformation is originated from glass transitions between a soft and hard state in SMPs. The only difference is that the switchable segment is more versatile for a multi-SMP. Take triple-SMP as an example, instead of one programming and shape fixing step, a two-step programming and shape fixing (Fig. 2.14 (b,c) and (d,e)) is required by controlling the external stimulus. [134, 135] It is essential to note that intermediate shapes along the same recovery pathway does not count as multi-SME, shape change between temporary shapes must be a discontinuous fashion. [43, 132]

2.3.3 Shape Memory Effect at Nanoscales

Stimulated by the fast growing miniaturization technology, recent interest and utilization of conventional SMMs is motivated by the increasing popularity and large potential associated with micro- and nanotechnologies. Extensive studies, especially at nanoscale, have

been reported to demonstrated micro-/nanoscopic SME at the surface of bulk SMAs and SMPs. [136–139] The shape memory mechanisms at small scales are identical to those at macroscopic scale. For example, thermal induced martensitic transformation at nanoscopic scale is observed on NiTi thin film using nanoindentation technology. The depth of nano-indents are found to be less than 100 nm. [136] For SMPs, nano-indents as small as approximately 20 nm can be created to generate glass transition induced SME through laser heating and indentation techniques. [140] These observations can be classified as shape memory surfaces.

While shape memory surfaces of conventional SMMs can be directly used for many surface morphology applications via nanopatterning, [137,141] it should be noted that the materials themselves are still at relatively large scales (e.g. macroscopic or sub-micron range). That is to say, the presence of SME is greatly depend on the sample size. It has been reported that the martensitic transformation for SMAs, thus the SME, completely vanishes when the size is smaller than several nanometres due to the influence of surface and interface energy. [142–146] Additionally, utilizing SMP based shape memory surfaces in NEMS may be extremely difficult because it is unlikely to fabricate a single piece of polymer at nanoscopic size. More recently, BiFeO₃ (BFO) with the thickness of 150 nm is found to exhibit SME as a result of martensitic-like phase transformation. However, the dissolving of phase mixture (i.e. R/T mixture) for shape memory oxide (BFO) fades away the SME when the lateral size of the sample is smaller than 10 μm . [147] Therefore, it is extremely challenge to miniaturize conventional SMMs down to approximately nm range due to their inherent constraints.

As mentioned previously, most often employed SMMs are stimulated by heat as mentioned previously. Consequently, inefficient heating and cooling processes during each shape memory cycle directly leads to low actuation frequency. [32] This is another major drawback besides the intrinsic size effect. Furthermore, the controllability of thermal-responsive SMMs is rigorously limited due to carefully monitoring and controlling are mandatory to avoid overheating and damaging. [148] Given that high actuation frequency is exceedingly desired in miniaturized actuators, it is foreseeable that SMM-based nano-actuators stimulated by heat will suffer when fast response speed is required for NEMS.

Therefore, rather than focusing on optimizing nanoscale SME in a bulk or non-nanoscale SMMs, a brand new approach by finding a shape memory nano-material or SME of a two-dimensional material is proposed in this thesis. One may expect that two-dimensional SMM that exhibits large deformation at sub-nanometer scale in conjunction with high actuation frequency will offer great potential for future nano-actuators. The findings from this investigation is detailed in Chapter 4.

2.4 Quantum Mechanical Effect

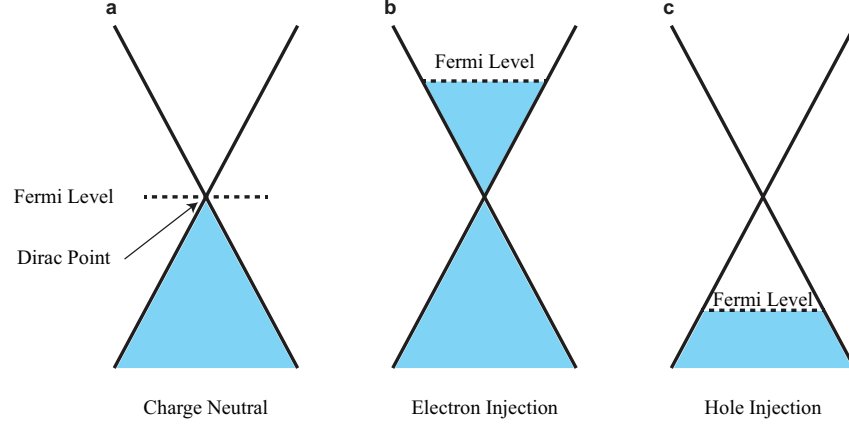


Figure 2.15: Quantum Mechanical Actuation of Graphene upon charge injection.

Actuation induced by quantum mechanical effect can be simply classified as the length change of covalent bond upon external charge injection (i.e. electron or hole injection). The underlying mechanism is originate from the changes in orbital occupation and band structure of an atom lattice. [10,14,15] Since the works of this thesis is focus on graphene oxide, quantum mechanical actuation of both electron injection and hole injection are presented here by taking monolayer graphene as an example (Fig. 2.15). When the graphene is charge neutral (Fig. 2.15 (a)), the Fermi level is at the same level as the Dirac point. Electrons have fully occupied the bonding state (below the Fermi level) and the anti-bonding state is empty at this stage. Upon the electron charge injection (Fig. 2.15 (b)), the Fermi level will shift above the Dirac point and excess electrons into the system start to fill in the anti-bonding state (or the valence band), which is unoccupied under charge neutral condition. This directly leads to a change in orbital occupation of the atomic lattice. Specifically, π orbitals of carbon atoms. Owing to the anti-bonding nature of these π orbitals, a repulsive force is generated between the π orbitals of each carbon atom and a resultant carbon-carbon covalent bond expansion can be observed. Thus, actuation of graphene along the basal plane. Alternatively, if the graphene is subjected to the hole injection (electrons are gradually removed from the system), the Fermi level will decrease below the Dirac point (Fig. 2.15 (c)). Electrons are removing from the bonding state (or conduction band), the strength of neighbouring carbon-carbon covalent bonds become weaker and weaker. Consequently, the expansion of graphene. [1,54,149]

2.4.1 Actuation of Carbon-based Materials

One of the first demonstrations of quantum mechanical actuation in carbon-based materials was reported in 1999, Baughman et al. proposed the revolutionary carbon nanotube (CNT) actuator. [10] As shown in Fig. 2.16 (a), the carbon single-walled nanotubes (SWNT) sheets were immersed in an aqueous electrolyte (blue background). Two actuation mechanisms of the CNT actuators are claimed based the charge density. For low charge densities, it

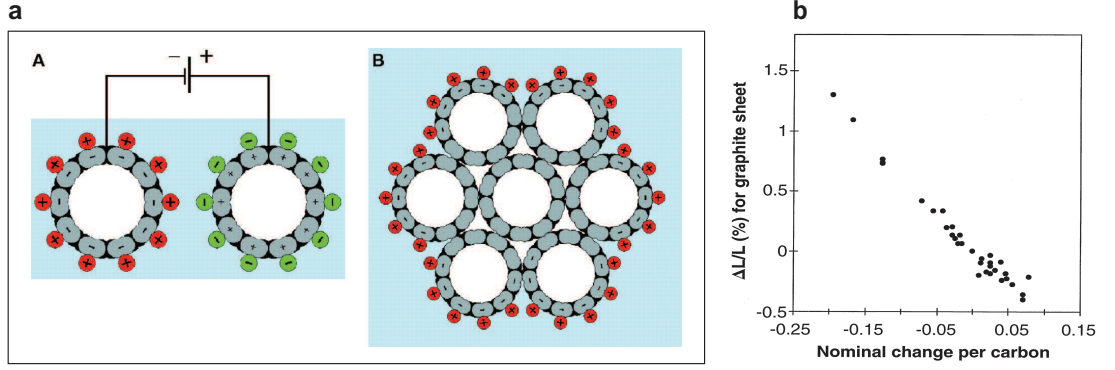


Figure 2.16: (a) Experimentally derived changes in basal plane strain as a function of nominal charge for graphite intercalation compounds. (b) Schematic illustration of charge injection in a nanotube-based electromechanical actuator and the effect of nanotube bundling. From [10]. Reprinted with permission from AAAS.

was found that the actuation strain is major induced by the quantum mechanical effect (i.e. the dimensional changes in the carbon-carbon covalent bond upon charge injection). Both expansion and contraction of the carbon-carbon bond are observed for electron injection and hole injection, respectively. This observation agrees with basal plane strain of graphite intercalation compounds upon charge injection (Fig. 2.16 (b)). For high-density charge injection, the quantum chemical effect and electrostatic-double layer (EDL) effect dominate the actuation performance, where the electrostatic repulsive force between like charges on the CNTs work against the stiff carbon-carbon bonds to elongate and expand the nanotubes. No contraction is observed for charge injection of either sign. By applying a low operation voltage of a few volts, the maximum observed strain for CNT bundle is approximately 0.2 % and the predicted strain performance of non-bundled SWNT would be about 1 % due to dramatically increase in surface area. For comparison, piezoelectric actuators only provide a strain of 0.1 % at very high voltage. On top of exceptional strain performance, the actuation frequency is greater than 1 KHz and much higher value may be achieved for single nanotube actuator. Furthermore, a close-packed SWNTs bundle are able to generate extremely high work density thanks to their inherent high modulus (0.64 TPa). Following this seminal work, many experimental works have sought to optimise this novel actuator. [150–152] From the theoretical side, density functional theory study with periodic boundary conditions suggested that asymmetric strain-charge relationship with respect to sign of charge transfer and the strain charge curves strongly depend on the nanotube type when the tube diameter is small. [153]

Inspired by the CNT actuators, great progress has been made in graphene-based actuators since its discovery in 2004. [48] Here, a few examples based on different mechanism are discussed. One of the first related study was utilising suspended exfoliated graphene sheets as electromechanical resonators by the McEuen group (Figure 2.17). The graphene sheets were mechanically exfoliated over predefined trenches etched into a SiO_2 surface and the graphene resonators were stimulated by either electrical or optical modulation. They

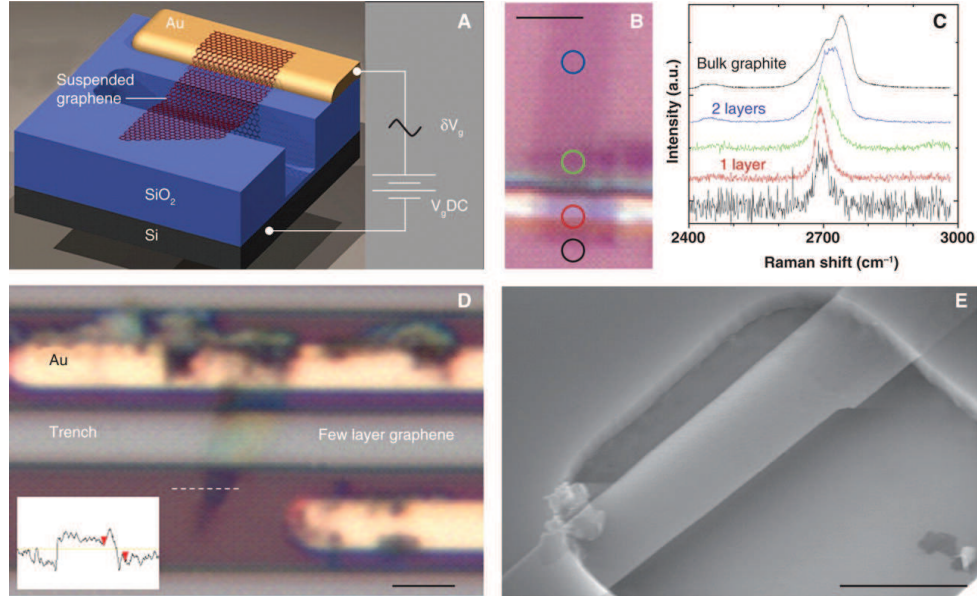


Figure 2.17: (a) Schematic of a suspended graphene resonator. (b) An optical image of a double-layer graphene sheet that becomes a single suspended layer over the trench. Scale bar, 2 μm . Each colored circle corresponds to a point where a Raman spectrum was measured. (c) Raman signal from a scan on the graphene piece. Each colored scan is data taken at each of the matching colored circles. The top scan is used as a reference and corresponds to the Raman shift of bulk graphite. (d) An optical image of few-layer (~ 4) graphene suspended over a trench and contacting a gold electrode. Scale bar, 1 μm . (Inset) A line scan from tapping mode AFM corresponding to the dashed line in the optical image. It shows a step height of 1.5 nm. (e) A scanning electron microscope image of a few-layer (~ 2) graphene resonator. Scale bar, 1 μm . From [11]. Reprinted with permission from AAAS.

found that the single-layer graphene exhibits a resonant frequency of 70.5 MHz, and the resonant frequencies (i.e. range from tens to hundreds of MHz) vary with the thickness of the graphene sheets (or number of layers). In addition, the graphene resonators give the highest modulus, greater than Si cantilevers and similar to carbon SWNT and diamond in NEMS. [154,155] Importantly, the graphene resonators show no degradation in Young's modulus with decreasing thickness unlike the ultrathin Si cantilevers. [156]

A novel unimorph electrochemical actuator based on a monolithic graphene film with asymmetrically modified surfaces was developed by Xie et al. [12] Taking the advantage of asymmetrical electrochemical responses, the actuation of graphene film was generated by treating one side of graphene surface with Hexane plasma and treating the other side with O₂ plasma (Fig. 2.18 (a)). Specifically, the asymmetric-modified graphene strip was immersed into the aqueous 1M NaClO₄ electrolyte. By applying the potential region of ± 1.2 volts, the graphene strip showed a maximum deflection of 15 mm at the tip, which reversed on reversal of the applied potential (Fig. 2.18 (b)). The untreated graphene film and the sample with both sides treated by hexane or O₂ plasma do not show significant actuation under same setup. Additionally, the length changes of graphene strips treated

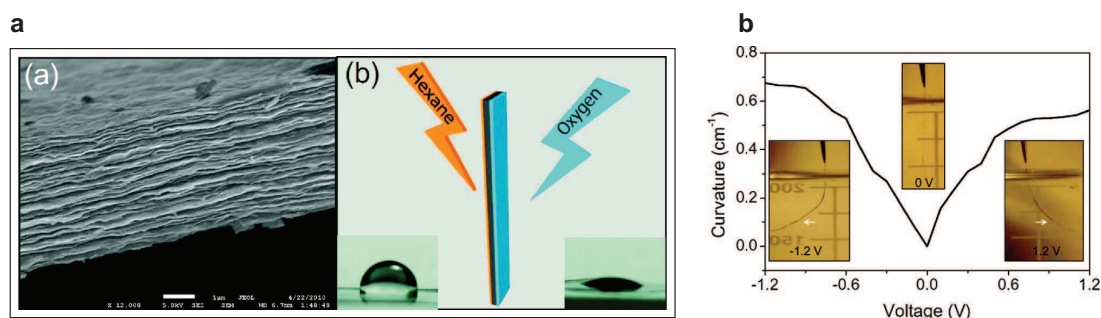


Figure 2.18: (a) Cross-section SEM image of a graphene film (scale bar: 1 μm) asymmetrically treated with hexane and oxygen plasma (schematic illustration). (b) Curvature change of an Asy-modified graphene strip as a function of applied CV potential within 1.2 V. Insets show the status of the graphene strip at 1.2, 0, and 1.2 V, respectively. Reprinted with permission from [12]. Copyright (2010) American Chemical Society.

solely with Hexane and O_2 plasma under applied potential was investigated. Similar to the CNT actuator discussed above, the electron injection causes an expansion and a contraction occurred for the hole injection. The maximum length change up to 0.2 % is obtained for O_2 plasma treated graphene strip.

In contrast with many conventional material, graphene contracts upon heating (i.e. negative coefficient of thermal expansion). [157, 158] A graphene/epoxy hybrid bimorph microactuator based on this distinctive behaviour has been reported by Zhu et al. [13] The conducting graphene films were directly heated and the organic epoxy film was warmed up by the diffused heat upon applying the electric power. The asymmetrical thermal expansion between the graphene and epoxy films is expected to cause upward deflection of the actuator upon heating the setup. Figure 2.19 (a) shows that the deflection of the cantilever increased linearly with temperature or the input voltage from 1 to 4 volts. The cantilever also produced a very rapid response even at a low input voltage because of the high thermal conductivity of graphene. For an input of 1 volt, the cantilever tip moved up to 1 μm in 0.02 s and returned to its starting position in 0.1 s. Since graphene is used for both actuation and structural support to generate a flapping and bending movement that could be controlled by the applied voltage which is in a similar form to the transparent dragonfly (Fig. 2.19 (b)), the graphene/epoxy hybrid bimorph actuator highlight its potential for biomimetic actuators. [159, 160]

2.4.2 Quantum Mechanical Effect of Graphene and Graphene Oxide with Order Epoxy Groups

Despite graphene-based materials were proven have the potential to develop high performance actuators in MEMS/NEMS, the strain contribution from individual actuation mechanism remains unclear. Thus, further studies are required to provide a comprehensive understanding of actuation mechanisms in graphene actuators fundamentally.

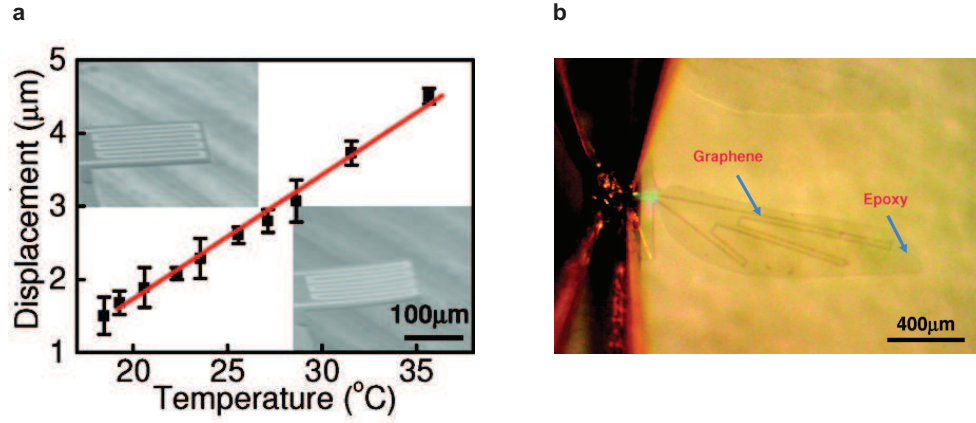


Figure 2.19: (a) Tip displacement of the cantilever beam as a function of temperature. Each data point is the average value of five measurements, and the standard deviation is shown as error bars. The solid line shows the fit to the data obtained from FEA. The insets show the SEM images of the initial position of the cantilever beam (top left) and bend up state upon applying electrical power (rightbottom). (b) Graphene-on-organic film which is in the form of a dragonfly wing. Reprinted with permission from [13]. Copyright (2011) American Chemical Society.

Recently, *ab initio* density functional theory studies were carried out by Rogers G. and Liu Z. to investigate the quantum mechanical and EDL effects in detail for monolayer layer graphene and graphene oxide. [14,15,47] Recall that the high carbon SWNT sheet strains were likely due to some two combinations of two phenomena: the quantum-mechanics and the electrostatic double-layer (EDL) that forms aside a charge surface. [10]

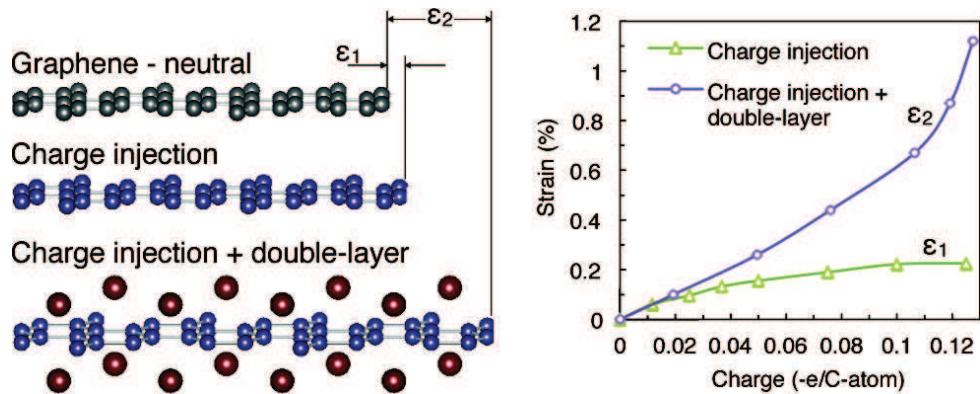


Figure 2.20: Quantum mechanical and Electrostatic Double-Layer (EDL) effects of graphene actuation. Reprinted with permission from [14] Copyright (2011) American Chemical Society.

In the case of pristine monolayer graphene (Fig. 2.20), it was shown that the formation of an EDL is the dominant actuation mechanism. The EDL induced strain (approximately 1 %) was found to exceed the quantum-mechanical strain (0.2 %) due to electron injection

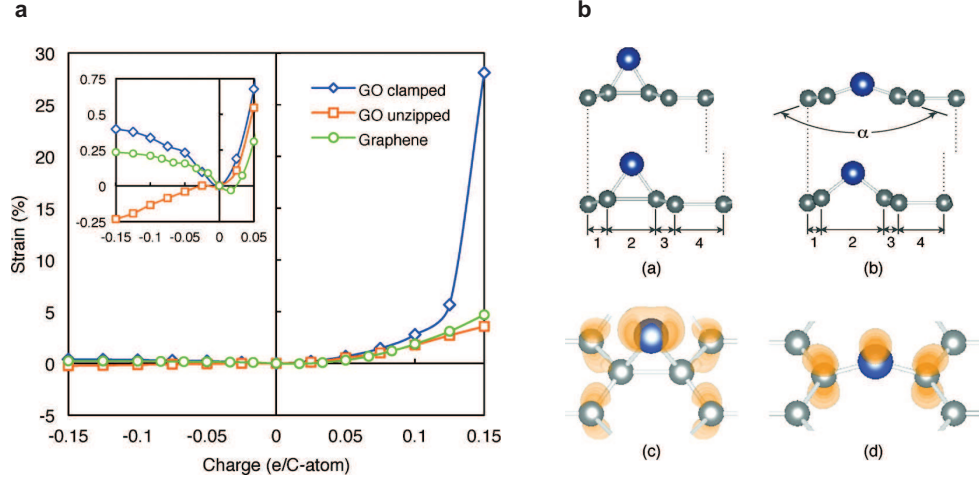


Figure 2.21: (a) Actuation of GO (clamped and unzipped) and pristine graphene due to positive (hole) and negative (electron) charge injection. Inset: close-up of the strain responses between -0.15 and $+0.05$ e per C-atom charge injection. (b) Total strain analysis and excess charge density profile of clamped and unzipped GO upon electron injection. Reprinted with permission from [15] Copyright (2012) American Chemical Society.

(charge injection of -0.12 e per C-atom). [14] Although EDL can lead to larger strain output, fast actuation frequency of quantum mechanical may still be favourable for nano-actuators since no ions diffusion is required.

For monolayer GO with ordered epoxy groups, the quantum mechanical effect of two distinct oxygen atom doping configurations of GO, metastable clamped and stable unzipped were examined. The in-plane strains due to charge injection of both GO configurations were calculated and compared with pristine monolayer graphene. Figure 2.21 (a) shows that very high strain were generated for hole injection, with the strains of 3.6 %, 4.7 % and 28.2 % for unzipped GO, pristine graphene and clamped GO. A unique contraction (-0.25 %) of unzipped GO upon electron injection was observed, while both pristine monolayer graphene and clamped GO expands 0.2 % and 0.4 %, respectively, for a -0.15 e per C-atom charge. The unique contraction behaviour was believed to be caused by the structural rippling effect of GO. The method of excess charge density distributions was used to verify the contraction origin (Fig. 2.21 (b)) It is clear to see that the extra -0.15 e per C-atom aggregates atop the O atom and also atop and beneath the O bonded C atoms. It means that the excess charge on the C atoms is repelled by that on the O atom. This repulsive force between the bonded O and C atoms produces in a torque about the O atom, which cause the bond angle α to decrease and the rippling to increase, thus the contraction of unzipped GO. In contrast, the excess injected charge aggregates aside the O atom and atop and beneath the non-O-bonded C atoms. Repulsive force acting between two non-O-bonded C atoms leads to an expansion of their C-C bond and an unchanged structural rippling of clamped GO, which is identical to the actuation of pristine graphene upon electron injection in the absence of structural rippling. Therefore, modulation of

structural rippling effect is an interesting characteristic of GO quantum mechanical actuation. [15]

Chapter 4, *Two-dimensional Shape Memory Graphene Oxide*, has identified that many GO crystals with ordered epoxy groups intrinsically exhibit two stable (or bi-stable) phases. The major structural difference of the bi-stable phases is the variation of carbon-oxygen-carbon bond angles, which directly leads to a single piece of GO crystal associated with two different structural rippling configurations. Specifically, the GO crystal structure of stable phase is much closer to a planar orientation than that of for the meta-stable phase. [17]

The natural question that arises is that:

How would these two phases with different structural rippling configurations response upon quantum mechanical effect? Would they exhibit similar or completely different actuation behaviours?

The exploration of two-way quantum mechanical actuation of graphene oxide is detailed in Chapter 5.

2.5 Density Functional Theory

Hohenberg and Kohn (1964) proved that the total energy, including exchange and correlation, of an electron gas (even in the presence of a static external potential) is a unique functional of the electron density. [161] The minimum value of the total-energy functional is the ground-state energy of the system, and the density that yields this minimum value is the exact single-particle ground-state density.

Kohn and Sham (1965) showed how to transfer the intractable complexity of many electron problems into the form of a set of self-consistent one-electron equations that is a unique functional of the electron density. Minimization of the functional with respect to the electron wavefunctions leads to the well-known Kohn-Sham equations, which are governing equations to calculate the electronic structure of the system. [162–164]

By considering an ion-electron interaction system, Kohn-Sham method expressed the electron density in terms of occupied single-particle orthonormal orbitals:

$$n(r) = \sum_i |\psi_i(r)|^2 \quad (2.5)$$

Since the velocity of electron is roughly 1000 times larger than the ion velocity in a solid and ions are much more massive than the electrons (typically m/M about $1/2000$ to $1/500000$), the electron and ion degrees of freedom can be decoupled. [165]

The electrons in each instantaneous configuration of the nuclei are always in their ground state. This is the so-called Born-Oppenheimer (BO) approximation, which allows nuclear and electronic degrees of freedom to be decoupled in *ab initio* simulations. Thus the total energy of a system can be expressed as:

$$E[\{\psi_i\}, \{R_I\}, \{\alpha_v\}] = \sum_i \int_{\Omega} d^3r \psi_i^*(r) \left[-\frac{\hbar^2}{2m} \nabla^2 \right] \psi_i(r) + U[n(r), \{R_I\}, \{\alpha_v\}] \quad (2.6)$$

- $\{R_I\}$ are the nuclear coordinates.
- $\{\alpha_v\}$ are all the possible external constraints imposed on the system, such as the volume Ω , the strain $\epsilon_{\mu\nu}$, etc.
- U contains the internuclear Coulomb repulsion and the effective electronic potential energy, including external nuclear, Hartree, and exchange and correlation contributions

The minimization of the energy functional Equation 2.6 with respect to $\psi_i(r)$ subject to the orthonormality constraint, generates the self-consistent Kohn-Sham equations to

determine the electronic structure of the system:

$$\left\{ -\frac{k^2}{2m} \nabla^2 + \frac{\delta U}{\delta n(r)} \right\} \psi_i(r) = \epsilon_i \psi_i(r) \quad (2.7)$$

The standard solution approach for Equation 2.7 had been based on repeated direct matrix diagonalization and this required a computational effort rapidly growing with the size of the problem. Furthermore, the entire procedure has to be repeated for any new atomic (nuclei) configurations. Therefore, at this stage, the structural ground state calculation completely based on the first-principles can be done for systems with only a small number of configurationally degrees of freedom. [163,166]

In 1985, R.Car and M. Parrinello adopt an entirely different approach. [167] They proposed to treat the minimization of the Kohn-Sham functional as a complex optimization problem, which can be solved using the concept of simulated annealing.

By applying so-called the dynamical simulated annealing method, the total-energy functional is the objective function and the variation parameters are the coefficients of the expansion of the Kohn-Sham orbitals in some convenient basis functions (such as plane wave), the ionic positions and/or the $\{\alpha_v\}$'s. It was found that the dynamical simulated annealing strategy based on MD not only can be applied to minimize the Kohn-Sham functional efficiently, but this approach also can be used to study of the properties of the system at finite temperature.

Recall the energy functional Equation 2.6, the parameters $[\{\psi_i\}, \{R_I\}, \{\alpha_v\}]$ were considered to be dependent on time and the Lagrangean was introduced:

$$L = \sum_i \frac{1}{2} \mu \int_{\Omega} d^3r |\dot{\psi}|^2 + \sum_I \frac{1}{2} M_I \dot{R}_I^2 + \sum_v \frac{1}{2} \mu_v \dot{\alpha}_v^2 - E[\{\psi_i\}, \{R_I\}, \{\alpha_v\}] \quad (2.8)$$

- The dot indicates time derivative.
- M_I are the physical ionic masses.
- μ and μ_v are arbitrary parameters of appropriate units.

where the ψ_i are subject to the orthonormality constraints:

$$\int_{\Omega} d^3r \psi_i^*(r, t) \psi_j(r, t) = \delta_{ij} \quad (2.9)$$

By combining Equation 2.8 with the Newtonian equations of motion of the nuclei, this approach produced a dynamics for the parameters $\{\psi_i\}$'s, $\{R_I\}$'s, and $\{\alpha_v\}$'s. This

means a set of pseudo-Newtonian equations of motion for the coupled electron-ion system:

$$\mu\ddot{\psi}_i(r, t) = -\frac{\delta E}{\delta\psi_i^*(r, t)} + \sum_k \Lambda_{ik}\psi_k(r, t) \quad (2.10)$$

$$M_I\ddot{R}_I = F_I = -\nabla_{R_I}E \quad (2.11)$$

$$\mu_v\ddot{\alpha}_v = -\left(\frac{\partial E}{\partial\alpha_v}\right) \quad (2.12)$$

- μ is a fictitious electron mass.
- Λ_{ik} are Lagrange multipliers introduced in order to satisfy the orthonormality constraints of the electronic orbitals in Equation 2.9.
- E is the total energy of the system.
- F_I is the force acting on the nuclei that coupled nuclear and electronic equations of motion.

Although the dynamics of ion in Equation 2.10–2.12 has a real physical meaning, the dynamics of electron are fictitious and have to be considered only as a tool of the dynamical simulated annealing to find the electronic ground state.

By variation of the velocities, $\left[\{\dot{\psi}_i\}, \{\dot{R}_I\}, \{\dot{\alpha}_v\}\right]$, the temperature of the system can be slowly reduced and for $T \rightarrow 0$ the dynamic equilibrium state of minimal E is reached. At the dynamic equilibrium, $\ddot{\psi}_i = 0$ and Equation 2.10 is identical within a unitary transformation to the Kohn-Sham equation Equation 2.7. Only in this case, Equations 2.10 and 2.11 describe a real physical system and the forces F_I are accurate.

In order to remain close to the ground state it is essential that the dynamics of nuclei and electrons are decoupled (the BO approximation) so that Equation 2.8 describe a real physical system whose representative point in configurationally space lies on the BO energy surface. Otherwise, the system would drift away from the BO energy surface and the calculated forces would become inaccurate. Generally, ions and electrons are effectively decoupled in semiconductors and insulators. However, metallic systems tend to drift away from the BO energy surface, special methods are required in this case. Therefore, instead of using empirical pair-potential MD approximation, it is now possible to conduct simulation of covalently bonded and metallic systems. [165]

For large systems, the electronic structure calculation by the dynamical simulated annealing approach is computationally more efficient than standard diagonalization techniques. For example, if the N occupied single-particle orbitals are expanded into M plane

waves ($M \gg N$), a standard diagonalization requires $O(M^3)$ operations, whereas Equation 2.10 requires $O(NM \ln M)$. Hence, it permits DFT simulations for much larger system.

Additionally, the iterative optimization of diagonalization, self-consistency, ionic relaxation, volume and strain relaxation are done simultaneously. As well as, the amount of classical kinetic energy can be used as a measure of the departure of a system from the self-consistent minimum of its total energy.

The algorithm proposed by R.Car and M. Parrinello has been implemented in the Car Parrinello Molecular Dynamics (CPMD) simulation code, [168] which has been widely used to simulate the physical properties of various material systems, such as metal, semiconductor and insulators. It is particularly widely used in biological systems, owing to the large size of the system.

Inspired by the initial proposed R.Car and M. Parrinello's method, the direct diagonalization of the Hamiltonian matrix was totally replaced by the iterative scheme, for example, the conjugate gradient method by Teter, Payne and Allan in 1989, [169] the efficient iterative algorithms using a plane-wave basis by Kresse and Furthmuller in 1996, [170] and so on. These algorithms have been implemented in the Vienna *Ab Initio* Simulation Package (VASP). [171] This package has been successfully applied on metallic, insulator and semiconductor systems. In addition, the projector augmented-wave method (PAW) developed by Blochl in 1994, which allows highly accurate simulation of all-electron calculations for all elements in the periodic table, [172] has also been implemented in the VASP code.

The first-principles calculations in this thesis are carried out with VASP, [171] using the projector augmented-wave method (PAW) and a plane wave basis set. The GGA exchange-correlation energy and the Monkhorst-Pack scheme is adopted throughout this thesis. [173,174]

Chapter 3

Piezoelectric Properties of Graphene Oxide

3.1 Overview

Since the discovery of piezoelectricity in many atomically thin materials, graphene (intrinsically non-piezoelectric) has been successfully engineered into piezoelectric material as discussed in Section 2.2.3. Inspired by doping adatoms onto the surface of graphene, which breaks the inversion symmetry and thus piezoelectricity, unit cell of GO with ordered epoxy groups (or chemisorption of oxygen atoms onto the graphene surface) belongs to the non-inversion symmetry point group. Hence, GO with ordered epoxy groups should exhibit piezoelectric effect just like graphene doped with adatoms. Indeed, both clamped and unzipped GO crystals are found to have piezoelectric responses upon the applied external electric field perpendicular to the basal plane of GO. The maximum in-plane strain and piezoelectric strain coefficient d_{31} are calculated to be 0.12 % and 0.24 pmV^{-1} . These values are comparable with the piezoelectric responses in graphene with some physisorbed atoms. lastly, a detailed strain analysis shows that piezoelectric strain coefficient d_{31} is depend on the oxygen doping rate (or C:O ratio).

3.2 Publication

The following publication was reprinted from [16] with the permission of AIP Publishing Copyright (2014).

Monash University

Declaration for Thesis Chapter 3

Declaration by candidate

In the case of Chapter 3, the nature and extent of my contribution to the work was the following:

Nature of contribution	Extent of contribution
Conceive the idea, design the model, run simulations, results analysis, interpretation and writing.	80%

The following co-authors contributed to the work:

Name	Nature of contribution	Extent of contribution
Dr. Jin Shang	Results Analysis	10%
Assoc. Prof. Wenyi Yan	Project Supervision	N/A
Dr. Zhe Liu	Project Supervision	N/A

The undersigned hereby certify that the above declaration correctly reflects the nature and extent of the candidate's and co-authors' contributions to this work.

Candidate's Signature:

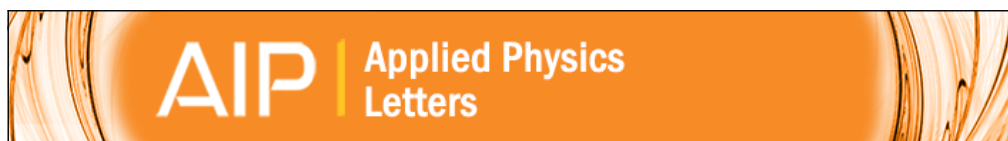
Candidate's Name: Zhenyue Chang

Date: 28th May 2016

Main Supervisor's Signature:

Main Supervisors's Name: Dr. Zhe Liu

Date: 28th May 2016

**Piezoelectric properties of graphene oxide: A first-principles computational study**

Zhenyue Chang, Wenyi Yan, Jin Shang, and Jefferson Zhe Liu

Citation: [Applied Physics Letters](#) **105**, 023103 (2014); doi: 10.1063/1.4890385View online: <http://dx.doi.org/10.1063/1.4890385>View Table of Contents: <http://scitation.aip.org/content/aip/journal/apl/105/2?ver=pdfcov>Published by the [AIP Publishing](#)

Articles you may be interested in[Hydrogen and fluorine co-decorated silicene: A first principles study of piezoelectric properties](#)J. Appl. Phys. **117**, 224304 (2015); 10.1063/1.4922404[First-principles studies on infrared properties of semiconducting graphene monoxide](#)J. Appl. Phys. **114**, 164313 (2013); 10.1063/1.4826910[The structural, dielectric, elastic, and piezoelectric properties of KNbO₃ from first-principles methods](#)J. Appl. Phys. **111**, 104107 (2012); 10.1063/1.4712052[Optical property and electronic band structure of a piezoelectric compound Ga₃P₂O₇ studied by the first-principles calculation](#)Appl. Phys. Lett. **92**, 261915 (2008); 10.1063/1.2955827[Piezoelectricity in ZnO nanowires: A first-principles study](#)Appl. Phys. Lett. **89**, 223111 (2006); 10.1063/1.2397013





Piezoelectric properties of graphene oxide: A first-principles computational study

Zhenyue Chang,¹ Wenyi Yan,¹ Jin Shang,² and Jefferson Zhe Liu^{1,a)}

¹Department of Mechanical and Aerospace Engineering, Monash University, Clayton, Victoria 3800, Australia

²Department of Chemical and Biomolecular Engineering, The University of Melbourne, Victoria 3010, Australia

(Received 6 April 2014; accepted 4 July 2014; published online 15 July 2014)

Some highly ordered compounds of graphene oxide (GO), e.g., the so-called clamped and unzipped GO, are shown to have piezoelectric responses via first-principles density functional calculations. By applying an electric field perpendicular to the GO basal plane, the largest value of in-plane strain and strain piezoelectric coefficient, d_{31} are found to be 0.12% and 0.24 pm/V, respectively, which are comparable with those of some advanced piezoelectric materials. An in-depth molecular structural analysis reveals that the deformation of the oxygen doping regions in the clamped GO dominates its overall strain output, whereas the deformation of the regions without oxygen dopant in the unzipped GO determines its overall piezoelectric strain. This understanding explains the observed dependence of d_{31} on oxygen doping rate, i.e., higher oxygen concentration giving rise to a larger d_{31} in the clamped GO whereas leading to a reduced d_{31} in the unzipped GO. As the thinnest two-dimensional piezoelectric materials, GO has a great potential for a wide range of micro/nano-electromechanical system (MEMS/NEMS) actuators and sensors. © 2014 AIP Publishing LLC.

[<http://dx.doi.org/10.1063/1.4890385>]

Actuators have been adopted in a diverse range of micro/nanoelectromechanical systems (MEMS/NEMS), including medical devices,¹ microrobotic,² artificial muscle,^{3–5} and many other smart structures.^{6,7} There has been an immense effort towards the development of advanced actuation materials in the past decade. The extensively studied electromechanical actuation has several actuation schemes.^{8,9} For example, the electrostatic force between charged objects can generate a mechanical motion, a piezoelectric strain is generated when piezoelectric materials are subject to an external electric field (i.e., the material remains charge neutral), and the electro-active actuation arises from electron or hole injection into electro-active materials (i.e., the material is charged). The piezoelectricity is widely used, because it exhibits a linear strain-electric field relation and a high response rate.^{8–10} To be applied in NEMS, the dimension of piezoelectric materials should be reduced to a nanometer scale. Two-dimensional piezoelectric materials,^{11–13} such as BN, MoS₂, MoSe₂, MoTe₂, WS₂, WSe₂, and WTe₂, are promising to address this demand. Graphene, as a representative of two-dimensional materials, have attracted a lot of interest because of its unique atomistic structure and excellent physical properties.^{14–23} It is an ideal candidate for the design of two-dimensional piezoelectric materials.

Recently, Ong *et al.* used density functional theory (DFT) calculations to study the piezoelectric properties of graphene-based materials.²⁴ It is well known that the piezoelectric effect only exists in crystalline materials with no inversion symmetry. To break the inversion symmetry of pristine graphene, Ong *et al.* introduced adatom (e.g., Li, K, H, and F) onto the graphene surface. As a result, a maximum

piezoelectric linear strain around 0.15% was generated.^{24,25} However, the main drawback of their materials is the weak interactions between the adatom and graphene surface,²⁶ which may lead to desorption at a relatively high operation temperature or under a high actuation frequency, causing potential failures of materials and devices.²⁷

Graphene oxide (GO), usually as the pre-product of synthesizing graphene, has generated huge interest for different types of applications.^{28,29} The vast diversity of GO atomistic structures gives rise to different electronic and mechanical properties that are potentially useful for actuation material designing.^{30–34} Recent experiments by Pandey *et al.* have shown highly ordered doping of oxygen (O) atoms on the hexagonal lattice of pristine graphene. Approximately 50% of the GO surfaces characterized using scanning tunneling microscope was found to comprise these periodic structures.¹⁹ There are two possible O atom doping configurations: so-called clamped and unzipped (Fig. 1).³⁵ These two types of GO compounds break the inversion symmetry of pristine graphene, therefore inducing piezoelectricity in GO. For the unzipped GO, the oxygen atoms form strong covalent bonds to two neighboring carbon atoms as shown in Fig. 1(b). For the clamped GO (Fig. 1(a)), the calculated adsorption energy of oxygen atoms at the bridging sites is 4.8 eV, which is more than three times larger than that of Li, K, and H, and about two times higher than F.²⁶ In addition, the migration energy of oxygen on a graphene surface is about 1 eV, which is much higher than that of Li and K (e.g., 0.3 eV and 0.12 eV, respectively).²⁶ It is known that if the migration energy is less than 0.5 eV, the adatom is mobile on a graphene surface at room temperature.²⁶ The ease of bulk fabrication, diversity of atomistic structures, and good stability render GO compounds good candidates for two-dimensional piezoelectric materials.

a) 

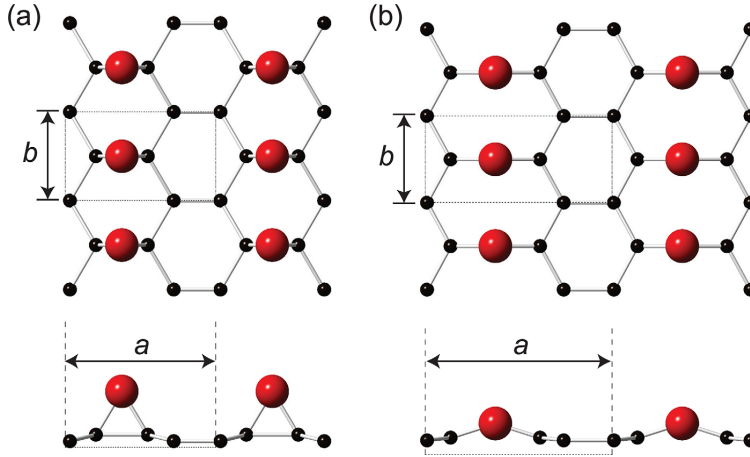


FIG. 1. Symmetrically clamped (a) and unzipped (b) GO configurations with a C/O ratio, $R_{C/O}$ of 4:1. Unit cells are depicted by dotted lines with in-plane lattice parameters shown as a and b . Black and red spheres represent the C and O atoms, respectively.

In this paper, we use first-principles calculations to investigate piezoelectric response of GO with different structural configurations. The obtained strain piezoelectric coefficients d_{31} are compared with results of the graphene with some physisorbed atoms. We also conduct an analysis to understand the structural origin of the piezoelectric strain in GO, which can explain the dependence of d_{31} on oxygen doping rate for the clamped and unzipped GO.

Figure 1 shows the unit cells of clamped and unzipped GO with a C/O ratio, $R_{C/O}$ of 4:1. For the unzipped GO, the C-C bond below oxygen atom is broken. Following the terminology from Xu and Xue, we term them as symmetrically clamped GO (sym-clamped) and symmetrically unzipped GO (sym-unzipped), respectively.³⁵ With the epoxy groups attached to one side, the crystal symmetry will be changed from a point group of $6/mmm$ for pristine graphene to a non-inversion symmetric point group of $mm2$. In this study, the clamped GO crystals with a $R_{C/O}$ of 2 and 4 are examined. Our DFT calculations show that for $R_{C/O} > 4$, the clamped GO is unstable. For the unzipped GO crystals, a $R_{C/O}$ of 4, 8, or 16 is studied. It is found that an unzipped GO crystal with $R_{C/O} < 4$ is unstable.

The Vienna *ab initio* simulation package (VASP v.5.3.3) is used to perform density functional calculations on piezoelectric responses of symmetric GO. Projector augmented wave pseudopotentials and the generalized gradient approximation are employed,^{36,37} with a plane-wave cutoff energy of 800 eV. A Monkhorst-Pack gamma-centered k -points grid of dimensions $24 \times 42 \times 1$ is adopted for the C_2O -sym-clamped and C_4O -sym-clamped cells, while a $10 \times 40 \times 1$ is used for the C_8O -sym-unzipped GO cell. As periodic boundary conditions are employed in VASP, very thick vacuum layers are included to minimize interlayer interactions. An interlayer spacing of 20 Å is used throughout, which represents a good balance between computational accuracy and efforts.³⁸ To hold this interlayer space constant, the VASP source code is modified to allow the simulation cells to relax within the plane of GO, but not in the perpendicular direction.³⁹ In all cases, the C and O atoms are allowed to relax in all directions. Prior to being subjected to an external electric field, all structures are fully relaxed to

determine their equilibrium lattice constants. The relative change of in-plane lattice constants under an applied electric field with respect to the equilibrium values are defined as piezoelectric strains.

Figure 2(a) shows the in-plane piezoelectric strains as a function of electric field strength from -0.5 to 0.5 eV/Å. A linear relation is observed for the sym-clamped GO crystals with $R_{C/O}$ of 2 and 4 and for the sym-unzipped GO crystals with $R_{C/O}$ of 4 and 8. Note that the magnitudes of the applied electric fields are experimentally achievable in graphene-based devices.⁴⁰ Overall, the sym-clamped GO has a better

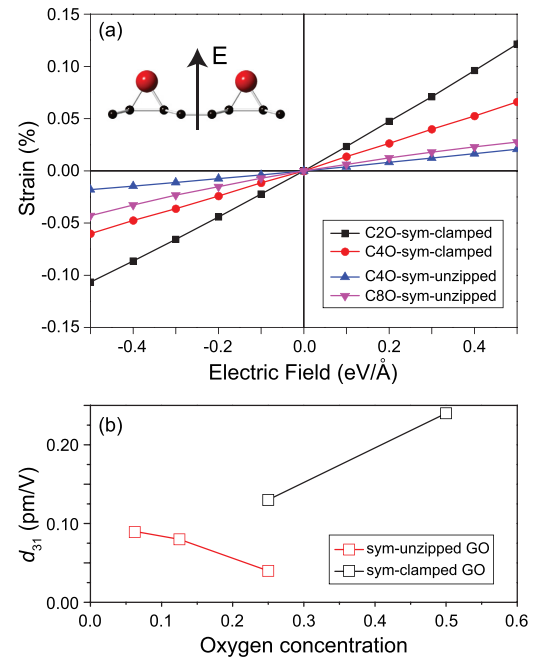


FIG. 2. (a) Piezoelectric strain of symmetric GO configurations being subject to an applied electric field perpendicular to the basal plane (inset). (b) The strain piezoelectric coefficient, d_{31} as a function of oxygen doping level for sym-clamped GO and sym-unzipped GO.

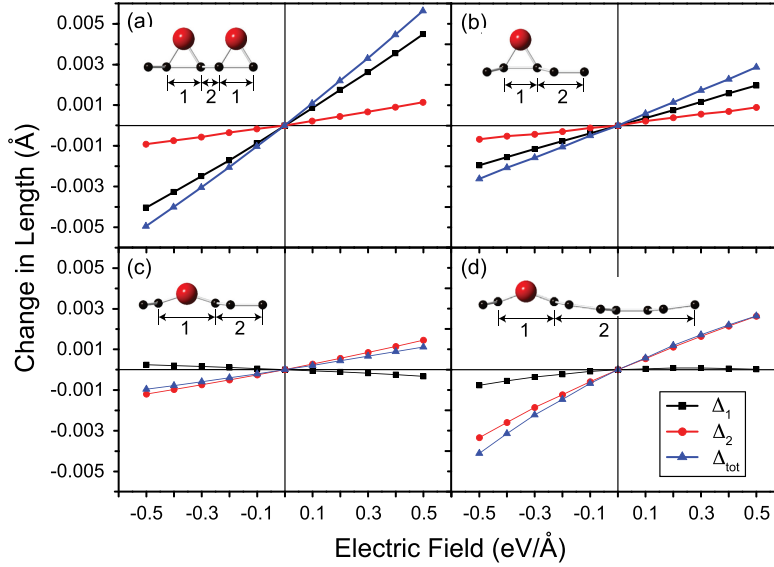


FIG. 3. Strain analysis of (a) C₂O-sym-clamped, (b) C₄O-sym-clamped, (c) C₄O-sym-unzipped, and (d) C₈O-sym-unzipped GO compounds. The change in total length, lengths of segment-1, and segment-2 of the supercells are represented by blue, black, and red symbols, respectively. Inset: side view of GO compounds with indications of segment-1 and segment-2. Black and red spheres represent the C and O atoms, respectively.

strain output than the sym-unzipped GO. The maximum strain output of 0.12% at an applied field of 0.5 eV/Å is close to the results from Ong *et al.* for graphene with some physisorbed adatoms (0.15%).²⁴

Figure 2(b) shows that the strain piezoelectric coefficient, d_{31} (i.e., the slope of strain vs. electric field curve) as a function of oxygen concentration. Overall, the d_{31} coefficients for the clamped GO are significantly larger than those of the unzipped GO. A higher oxygen concentration in sym-clamped GO leads to a larger d_{31} , whereas an opposite trend is observed for the sym-unzipped GO. The C₂O-sym-clamped GO crystal has the maximum d_{31} (i.e., 0.24 pm/V), which is comparable with the maximum d_{31} coefficient obtained for the engineered piezoelectric graphene (i.e., 0.3 pm/V)²⁴ and the d_{31} coefficients of some three dimensional piezoelectric materials such as wurtzite boron nitride⁴¹ and wurtzite GaN⁴² (0.33 pm/V and 0.96 pm/V, respectively). But the d_{31} value is far smaller than the most widely used piezoelectric ceramics, Lead Zirconate Titanate (PZT), 119 pm/V.⁴³ It should be noted that for piezoelectric ceramic thin films with a thickness lower than 10 nm, the depolarization field generated by the accumulated surface charges will completely suppress the piezoelectric effects. Our proposed piezoelectric GO will not suffer this problem, giving rise to great potentials in NEMS applications.

To gain an in-depth understanding of piezoelectric properties of sym-clamped and sym-unzipped GO, we decomposed the in-plane deformation of GO crystals into two contributions. As shown in the insets of Fig. 3, the in-plane projection of interatomic distance of the two carbon atoms bonded by the oxygen atoms is defined as segment-1. The segment-2 is the in-plane projection of rest of the crystal. The total deformation, Δ_{tot} as shown in Fig. 3, is the summation of the length change in segment-1 and segment-2. For the sym-clamped cases (Figs. 3(a) and 3(b)), it is evident that the length change of segment-1, Δ_1 dominates the overall piezoelectric strain output. It appears that Δ_1 for C₂O-sym-clamped

is almost twice of that of C₄O-sym-clamped GO, which is consistent with increase of oxygen concentration (or the increase of portions of segment-1). The length change in segment-2, Δ_2 is approximately the same for the two clamped GO crystals. Thus, it is reasonable to understand that the strain output as well as the strain piezoelectric coefficient d_{31} is nearly doubled in C₂O-sym-clamped GO when comparing with the results of C₄O-sym-clamped GO (Fig. 2). In contrast, for the unzipped GO (Figs. 3(c) and 3(d)), Δ_1 is virtually negligible and the deformation mainly comes from segment-2. The increase of oxygen concentration reduces the proportion of segment-2 in the unzipped GO, thus leading to a reduction of d_{31} in Fig. 2(b).

With the oxygen concentration of GO reduced to 0.0625 (i.e., $R_{C/O} = 16$), some distinctive electromechanical properties were observed. Figure 4 shows the in-plane electromechanical strain as a function of the applied external electric

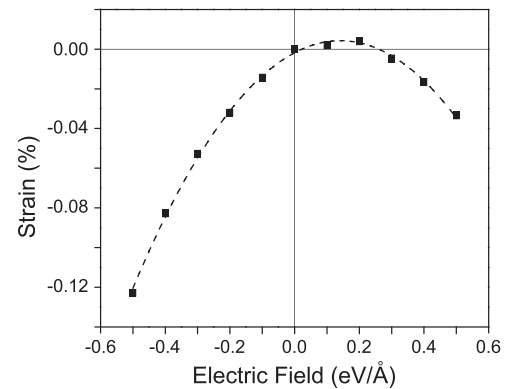


FIG. 4. In-plane strain of C₁₆O-sym-unzipped GO as a function of applied electric field perpendicular to the basal plane. The dashed line represents a second order polynomial fitting result.

field. It appears to be a parabolic relation with a clear shift toward the side of positive electric fields. We believe that the observed strain should originate from a combination of the electrostriction and piezoelectric effects. Fitting the non-linear strain-electric field relationship using a second order polynomial yields $\varepsilon_{11} = -0.00303E_3^2 + 0.0009E_3 - 1.79 \times 10^{-5}$, in which ε_{11} is the in-plane strain and E_3 is the strength of electric field along the perpendicular direction. The linear term arises from the piezoelectric effect. The deduced coefficient $d_{31} = 0.09 \text{ pm/V}$ is shown in Fig. 2(b), which is consistent with the d_{31} results of other GO compounds. The electrostriction effect⁴⁴ shows $\varepsilon_{11} = M_{13}E_3^2$, from which the electrostriction coefficient M_{13} is determined as $-3 \times 10^{23} \text{ m}^2/\text{V}^2$. The results shown in Figure 4 indicate that the electrostriction dominates the electromechanical strains of C_{16}O -sym-unzipped GO. In contrast to most electrostrictive polymers, our GO crystal has a negative M_{13} coefficient. In other words, our C_{16}O -sym-unzipped GO crystal shows a contraction in the transverse direction upon the application of a perpendicular electrical field, whereas most electrostrictive polymers exhibit a transverse elongation. Physical origins for this distinctive electrostriction effect are not clear, which is worth of future investigations.

It is known that bulk materials without a band gap cannot exhibit piezoelectricity because a conductor is unable to produce sufficient electric polarization. Our DFT simulations show that only C_2O -sym-clamped and C_4O -sym-clamped GO have a band gap, i.e., 2.9 eV and 1.5 eV, respectively, whereas other compounds have a zero band gap. It appears that the observed piezoelectricity of our GO compounds with a zero band gap is contradictory to the well-accepted knowledge. However, it is worth to note that the GO crystals are only conducting in the basal plane of the sheet. Upon an applied electric field in the perpendicular direction to the basal plane, polarization can be induced and thus piezoelectricity can exist. This is a unique feature of two-dimensional materials, which is recognized by Ong *et al.*²⁴ Note that in VASP calculations, being subject to an electric field parallel to GO basal plane, indeed no piezoelectric effect is observed (i.e., $d_{11} = 0$). We also notice that the insulators (sym-clamped GO) have a larger d_{31} than the conductors (sym-unzipped GO) (Fig. 2(b)). But due to the limited results, it is hard to conclude this correlation.

In summary, piezoelectric properties of GO with different structural configurations and oxygen concentration are studied using the first-principles density functional calculations. The maximal values of in-plane strain and strain piezoelectric coefficient are obtained for C_2O -sym-clamped GO, i.e., a strain of up to 0.12% and $d_{31} = 0.24 \text{ pm/V}$. An increase of oxygen concentration in the clamped GO enhances the piezoelectric strain output and the d_{31} coefficient, whereas an opposite trend is observed for the unzipped GO. Through an in-depth structural analysis, we find that the deformation of the oxygen-doped region dominates the piezoelectric strain of the clamped GO. On the contrary, deformation from the "graphene" region without oxygen dopant makes the major contribution to the piezoelectric strain of the unzipped GO. Interestingly, at a low oxygen concentration, the GO exhibits a much more profound electrostrictive deformation than the piezoelectric deformation. A negative electrostriction coefficient, M_{13} , is obtained for

C_{16}O -sym-unzipped GO, in contrast to most of the electrostrictive polymers. Due to the excellent piezoelectric properties, the robust molecular structures, and an atomic thickness, GO crystals are promising two-dimensional piezoelectric materials for MEMS/NEMS actuators and sensors.

The authors acknowledge the Engineering Faculty of Monash University for providing a seed grant and acknowledge National Computational Infrastructure at Australian National University and Monash Sun Grid high-performance computing facility for providing the computational resources.

- ¹J.-H. Jeon, T.-H. Cheng, and I.-K. Oh, "Snap-through dynamics of buckled IPMC actuator," *Sens. Actuators, A: Phys.* **158**, 300–305 (2010).
- ²S.-W. Yeom and I.-K. Oh, "A biomimetic jellyfish robot based on ionic polymer metal composite actuators," *Smart Mater. Struct.* **18**, 085002 (2009).
- ³G. W. Rogers and J. Z. Liu, "Monolayer graphene oxide as a building block for artificial muscles," *Appl. Phys. Lett.* **102**, 021903 (2013).
- ⁴J. Lu, S.-G. Kim, S. Lee, and I.-K. Oh, "A biomimetic actuator based on an ionic networking membrane of poly(styrene-alt-maleimide)-incorporated poly(vinylidene fluoride)," *Adv. Funct. Mater.* **18**, 1290–1298 (2008).
- ⁵R. H. Baughman, "Conducting polymer artificial muscles," *Synth. Met.* **78**, 339–353 (1996).
- ⁶U. Kim, J. Kang, C. Lee, H. Y. Kwon, S. Hwang, H. Moon, J. C. Koo, J.-D. Nam, B. H. Hong, J.-B. Choi, and H. R. Choi, "A transparent and stretchable graphene-based actuator for tactile display," *Nanotechnology* **24**, 145501 (2013).
- ⁷S.-E. Zhu, R. Shabani, J. Rho, Y. Kim, B. H. Hong, J. H. Ahn, and H. J. Cho, "Graphene-based bimorph microactuators," *Nano Lett.* **11**, 977–981 (2011).
- ⁸J. Z. Liu, G. W. Rogers, and J. Hughes, "Electromechanical actuation of pristine graphene and graphene oxide: Origin, optimization and comparison," in *Carbon Nanotubes for Actuators* (Springer, 2014).
- ⁹M. Tabib-Azar, *Microactuators* (Kluwer Academic Publishers, the Netherlands, 1997).
- ¹⁰C. R. de Lima, S. L. Vatanabe, A. Choi, P. H. Nakasone, R. F. Pires, and E. C. Nelli Silva, "A biomimetic piezoelectric pump: Computational and experimental characterization," *Sens. Actuators, A: Phys.* **152**, 110–118 (2009).
- ¹¹K.-A. N. Duerloo, M. T. Ong, and E. J. Reed, "Intrinsic piezoelectricity in two-dimensional materials," *J. Phys. Chem. Lett.* **3**, 2871–2876 (2012).
- ¹²D. Wickramaratne, F. Zahid, and R. K. Lake, "Electronic and thermoelectric properties of few-layer transition metal dichalcogenides," *J. Chem. Phys.* **140**, 124710 (2014).
- ¹³H. J. Conley, B. Wang, J. I. Ziegler, R. F. Haglund, Jr., S. T. Pantelides, and K. I. Bolotin, "Bandgap engineering of strained monolayer and bilayer MoS_2 ," *Nano Lett.* **13**, 3626–3630 (2013).
- ¹⁴K. S. Novoselov, A. K. Geim, S. V. Morozov, D. Jiang, Y. Zhang, S. V. Dubonos, I. V. Grigorieva, and A. A. Firsov, "Electric field effect in atomically thin carbon films," *Science* **306**, 666–669 (2004).
- ¹⁵A. K. Geim, "Graphene: Status and prospects," *Science* **324**, 1530–1534 (2009).
- ¹⁶P. Avouris, Z. Chen, and V. Perebeinos, "Carbon-based electronics," *Nat. Nanotechnol.* **2**, 605–615 (2007).
- ¹⁷C. Lee, X. Wei, J. W. Kysar, and J. Hone, "Measurement of the elastic properties and intrinsic strength of monolayer graphene," *Science* **321**, 385–388 (2008).
- ¹⁸T. J. Booth, P. Blake, R. R. Nair, D. Jiang, E. W. Hill, U. Bangert, A. Bleloch, M. Gass, K. S. Novoselov, M. I. Katsnelson, and A. K. Geim, "Macroscopic graphene membranes and their extraordinary stiffness," *Nano Lett.* **8**, 2442–2446 (2008).
- ¹⁹D. Pandey, R. Reifengerger, and R. Piner, "Scanning probe microscopy study of exfoliated oxidized graphene sheets," *Surf. Sci.* **602**, 1607–1613 (2008).
- ²⁰J.-A. Yan, L. Xian, and M. Chou, "Structural and electronic properties of oxidized graphene," *Phys. Rev. Lett.* **103**, 086802 (2009).
- ²¹R. H. Baughman, C. Cui, A. A. Zakhidov, Z. Iqbal, J. N. Barisci, G. M. Spinks, G. G. Wallace, A. Mazzoldi, D. D. Rossi, A. G. Rinzier, O. Jaschinski, S. Roth, and M. Kertesz, "Carbon nanotube actuators," *Science* **284**, 1340–1344 (1999).
- ²²J. S. Bunch, A. M. van der Zande, S. S. Verbridge, I. W. Frank, D. M. Tanenbaum, J. M. Parpia, H. G. Craighead, and P. L. McEuen, "Electromechanical resonators from graphene sheets," *Science* **315**, 490–493 (2007).

023103-5 Chang *et al.*Appl. Phys. Lett. **105**, 023103 (2014)

- ²³X. Xie, L. Qu, C. Zhou, Y. Li, J. Zhu, H. Bai, G. Shi, and L. Dai, "An asymmetrically surface-modified graphene film electrochemical actuator," *ACS Nano* **4**, 6050–6054 (2010).
- ²⁴M. T. Ong and E. J. Reed, "Engineered piezoelectricity in graphene," *ACS Nano* **6**, 1387–1394 (2012).
- ²⁵R. K. Prasad, *Quantum Chemistry* (New Age Science, Tunbridge Wells, 2010).
- ²⁶K. Nakada and A. Ishii, "DFT calculation for adatom adsorption on graphene," in *Graphene Simulation* (InTech, Rijeka, 2011).
- ²⁷M. Viefhues, S. Manchanda, T.-C. Chao, D. Anselmetti, J. Regtmeier, and A. Ros, "Physisorbed surface coatings for poly(dimethylsiloxane) and quartz microfluidic devices," *Anal. Bioanal. Chem.* **401**, 2113–2122 (2011).
- ²⁸V. C. Tung, M. J. Allen, Y. Yang, and R. B. Kaner, "High-throughput solution processing of large-scale graphene," *Nat. Nanotechnol.* **4**, 25–29 (2008).
- ²⁹G. Eda, G. Fanchini, and M. Chhowalla, "Large-area ultrathin films of reduced graphene oxide as a transparent and flexible electronic material," *Nat. Nanotechnol.* **3**, 270–274 (2008).
- ³⁰J. W. Suk, R. D. Piner, J. An, and R. S. Ruoff, "Mechanical properties of monolayer graphene oxide," *ACS Nano* **4**, 6557–6564 (2010).
- ³¹J. Oh, M. E. Kozlov, J. Carretero-González, E. Castillo-Martínez, and R. H. Baughman, "Thermal actuation of graphene oxide nanoribbon mats," *Chem. Phys. Lett.* **505**, 31–36 (2011).
- ³²D. W. Boukhvalov and M. I. Katsnelson, "Modeling of graphite oxide," *J. Am. Chem. Soc.* **130**, 10697–10701 (2008).
- ³³G. W. Rogers and J. Z. Liu, "Graphene actuators: Quantum-mechanical and electrostatic double-layer effects," *J. Am. Chem. Soc.* **133**, 10858–10863 (2011).
- ³⁴G. W. Rogers and J. Z. Liu, "High-performance graphene oxide electromechanical actuators," *J. Am. Chem. Soc.* **134**, 1250–1255 (2012).
- ³⁵Z. Xu and K. Xue, "Engineering graphene by oxidation: A first-principles study," *Nanotechnology* **21**, 045704 (2009).
- ³⁶G. Kresse and J. Furthmüller, "Efficient iterative schemes for *ab initio* total-energy calculations using a plane-wave basis set," *Phys. Rev. B* **54**, 11169–11186 (1996).
- ³⁷G. Kresse and D. Joubert, "From ultrasoft pseudopotentials to the projector augmented-wave method," *Phys. Rev. B* **59**, 1758–1775 (1999).
- ³⁸G. Sun, M. Kertesz, J. Kürti, and R. Baughman, "Dimensional change as a function of charge injection in graphite intercalation compounds: A density functional theory study," *Phys. Rev. B* **68**, 125411 (2003).
- ³⁹VASP source code "*constr_cell_relax.F*" was modified in order to relax the *simulation supercell* in the GO basal plane only.
- ⁴⁰Y. Zhang, T.-T. Tang, C. Girit, Z. Hao, M. C. Martin, A. Zettl, M. F. Crommie, Y. R. Shen, and F. Wang, "Direct observation of a widely tunable bandgap in bilayer graphene," *Nature* **459**, 820–823 (2009).
- ⁴¹K. Shimada, "First-principles determination of piezoelectric stress and strain constants of wurtzite III-V nitrides," *Jpn. J. Appl. Phys., Part 2* **45**, L358–L360 (2006).
- ⁴²A. Hangleiter, F. Hitzel, S. Lahmann, and U. Rossow, "Composition dependence of polarization fields in GaInN/GaN quantum wells," *Appl. Phys. Lett.* **83**, 1169 (2003).
- ⁴³M. Dekkers, H. Boschker, M. van Zalk, M. Nguyen, H. Nazeer, E. Houwman, and G. Rijnders, "The significance of the piezoelectric coefficient $d_{31,eff}$ determined from cantilever structures," *J. Micromech. Microeng.* **23**, 025008 (2012).
- ⁴⁴R. C. DORF, *The Electrical Engineering Handbook* (CRC Press, Inc., Boca Raton, 1997).

Chapter 4

Two-dimensional Shape Memory Graphene Oxide

4.1 Overview

Section 2.3 clearly described that shape memory effect is caused by phase transformation. That is to say, a material should inherently exhibit at least two stable phases to enable the possibility of generating shape memory effect. During the structural analysis of GO crystals, we found that asymmetric C₈O GO exhibits two stable (or bi-stable) phases intrinsically. In addition, these bi-stable phases are separated by a significantly energy barrier, similar to Fig. 2.10 that used to illustrate shape memory effect from an energy point of view. One may expect that shape memory effect in the C₈O GO if reversible phase transformation between these two phases can be achieved upon an appropriate external stimulus.

In Chapter 3, we successfully demonstrated piezoelectric responses in various symmetric GO crystals upon the applied external electric field. In this Chapter, external electric field (perpendicular to the basal plane) is subjected to the asymmetric C₈O GO. Impressively, shape memory effect of two-dimensional GO is discovered as the result of phase transformation. The maximum recoverable strain output equals 14.5 %. This value is significantly larger than that of for commonly implemented shape memory alloys. Meanwhile, the mechanical properties is vastly better than that of for shape memory polymers. Overall, the actuation performance is beyond the limit of conventional actuation materials (Fig. 2.13). Furthermore, we also demonstrated the signature programmability feature in the C₈O GO, which suggests that C₈O GO is a two-dimensional shape memory material.

4.2 Publication

This manuscript has been officially accepted for publication by Nature Communications on 17th of May 2016 [DOI:10.1038/ncomms11972]. [17]

Monash University

Declaration for Thesis Chapter 4

Declaration by candidate

In the case of Chapter 4, the nature and extent of my contribution to the work was the following:

Nature of contribution	Extent of contribution
Conceive the idea, design the model, run simulations, results analysis, interpretation and writing.	70%

The following co-authors contributed to the work:

Name	Nature of contribution	Extent of contribution
Dr. Junkai Deng	Run simulations, results analysis	10%
Ganaka G. Chandrakumara	Run simulations, results analysis	10%
Assoc. Prof. Wenyi Yan	Project Supervision	N/A
Dr. Zhe Liu	Project Supervision	N/A

The undersigned hereby certify that the above declaration correctly reflects the nature and extent of the candidate's and co-authors' contributions to this work.

Candidate's Signature:

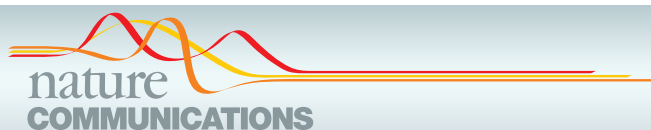
Candidate's Name: Zhenyue Chang

Date: 28th May 2016

Main Supervisor's Signature:

Main Supervisors's Name: Dr. Zhe Liu

Date: 28 May 2016



ARTICLE

Received 18 Dec 2015 | Accepted 17 May 2016 | Published xx xxx 2016

DOI: 10.1038/ncomms11972

OPEN

Two-dimensional shape memory graphene oxide

Zhenyue Chang^{1,2}, Junkai Deng³, Ganaka G. Chandrakumara^{1,2}, Wenyi Yan¹ & Jefferson Zhe Liu^{1,2}

Driven by the increasing demand for micro-/nano-technologies, stimuli-responsive shape memory materials at nanoscale have recently attracted great research interests. However, reducing the size of conventional shape memory materials down to approximately nanometre range, the shape memory effect diminishes. Here, using density functional theory calculations, we report the discovery of shape memory effect in a two-dimensional atomically thin graphene oxide crystal with ordered epoxy groups, namely C₆O. A maximum recoverable strain of 14.5% is achieved as a result of reversible phase transition between two intrinsically stable phases. Our calculations conclude co-existence of the two stable phases in a coherent crystal lattice, giving rise to the possibility of constructing multiple temporary shapes in a single material, thus, enabling highly desirable programmability. With an atomic thickness, excellent shape memory mechanical properties and electric field stimulus, the discovery of a two-dimensional shape memory graphene oxide opens path for the development of exceptional micro-/nano-electromechanical devices.

¹Department of Mechanical and Aerospace Engineering, Monash University, Clayton, Victoria 3800, Australia. ²Monash Centre for Atomically Thin Materials, Monash University, Clayton, Victoria 3800, Australia. ³State Key Laboratory for Mechanical Behaviour of Materials, Xi'an Jiaotong University, Xi'an 710049, China. Correspondence and requests for materials should be addressed to J.Z.L. (email: zhe.liu@monash.edu).

Shape memory materials (SMMs) are featured by the ability to recover their original shape from a significant quasi-plastic deformation upon an appropriate external stimulus¹. This interesting shape memory phenomenon occurs as a result of reversible phase transition, known as the shape memory effect (SME)². The recoverable mechanical deformation from SMMs, for example, ~0.5–8% strain from shape memory alloys (SMAs)³, 10% strain from shape memory ceramics (SMCs)⁴ and up to 400% strain from shape memory polymers (SMPs)⁵, endows them with an indispensable role in various applications such as actuators, sensors, mechanical joints, dampers and morphing devices^{3,5–8}. More interestingly, the most important feature of SMM, namely programmability, has been explored as a novel device design concept, so-called material-as-machine⁹, in which SMM can be programmed for actuation/motion following a pre-determined sequence, just like machines but with greater intelligence and flexibility whereby the material can sense and react accordingly¹⁰. This is particularly desirable for mechanical devices at a smaller size scale.

Indeed, recent interest and utilization of conventional SMMs (that is, SMAs, SMPs and SMCs) are motivated by the increasing popularity and large potential associated with micro- and nanotechnologies. Several studies have successfully demonstrated micro-/nanoscopic SME by introducing micro-/nanostructures at the surfaces of bulk SMAs and SMPs^{11–13}. Nevertheless, it should be noted that the materials themselves are still at relatively large scales (for example, macroscopic or sub-micron). Further miniaturization of conventional SMMs down to the nanometre range is hampered by their inherent constraints. For instance, recent studies on nanometre-sized SMA demonstrated that martensitic phase transformation (physical origin of the SME) completely diminishes below a critical size (4–60 nm), resulting from the influence of surface and interface energy^{14–17}. SMAs also experience other issues, such as oxidation and instability at nanoscale. In SMC film, the free charges at the surface lead to a depolarized electric field (E-field). It has been reported that by reducing the film thickness below a critical value (for example, ~20 nm), SMCs lose ferroelectricity, thus, the SME¹⁸. To date, there has been no reported study regarding SMPs down to the nanometre range, which could be attributed to fabrication challenges at this scale. In addition, the requirement of thermal stimulation that is commonly employed with conventional SMMs could restrict their implementation in nano-devices because of difficulties of precise control of the heating and cooling process and a low actuation frequency (about 1 Hz)³.

Here, using first-principles density functional theory (DFT) calculations, we report the discovery of SME in a two-dimensional atomically thin graphene oxide (GO) crystal (namely C₈O), triggered by a combination of E-field and mechanical force stimuli. In depth analysis, reveals a unique intra-molecular chemical interaction between oxygen *sp*² lone pair (*lp*) and carbon π orbitals as the structural origin for the SME. We also theoretically demonstrate the programmability (a key attribute of SMM) of C₈O, enabling C₈O as an advanced SMM at nanometre scale. This shape memory C₈O has superior shape memory mechanical properties well above the upper bound drawn in a recent survey of mechanical properties among available SMMs¹⁹. It is noteworthy that the E-field and mechanical force stimuli could overcome the limitations of commonly employed thermal stimuli at small size scales.

Results

Bi-stable phases of C₈O with ordered epoxy groups. GO inherits a diverse range of crystal structures with excellent physical, chemical and mechanical properties. Such outstanding

properties of GO have stimulated researchers to investigate its usage in a broad range of applications, such as energy storage, filtration membranes, actuators, sensors and transistors^{20–28}. Extensive studies in last decade identified epoxy and hydroxyl groups as two major functional groups on the basal plane of GO^{29,30}. Depends on the choice of synthesis methods under different conditions^{31–39}, various GOs structures are observed. For example, hydroxyl groups dominant the GO surface under hydrogen-rich environment³⁴. On the other hand, recent experimental progress suggests it is possible to produce GO with only epoxy groups under well-controlled experimental conditions^{33,36}.

Interestingly, some experimental studies show the existence of ordered line patterns of epoxy groups on the graphene basal plane with various C:O ratio^{37–39}. Pandey *et al.* used a scanning tunnelling electron microscope to capture atomic images of highly ordered GO structure with linearly aligned epoxy groups in a region that covers over 50% of the total scanned area³⁷. Fujii and Enoki observed regularly spaced line defects on chemically oxidized graphene sheets with length of ~100 nm using non-contact atomic force microscope, which were identified as the linear arrangement of epoxide groups³⁸. Meanwhile, many theoretical studies were carried out to investigate the formation mechanism of the ordered epoxy lines in experiments^{39,40,41}. In general, the presence of epoxy groups severely strains the graphene lattice. A cooperative alignment of epoxy groups in rows can efficiently reduce the strain. In addition, the aligned epoxy groups are able to unzip the C–C bonds beneath the oxygen atoms and reduce the energy further by ~1.2 eV per bond, which was believed to cause the faulty lines in graphene observed via dark-field optical microscope images³⁹.

Figure 1a shows an unzipped GO structure that closely resembles the one observed in Fujii's experiments³⁸. We studied two different C/O ratio cases, namely C₄O and C₈O. The adjacent rows of epoxy groups are placed on opposite sides of graphene basal plane. Such a configuration has been reported to be more stable as compared with the case with epoxy groups on a single side^{41,42}. In Fig. 1a, lattice constant *a* represents the unit cell length in *x* axis and α measures carbon–oxygen–carbon (C–O–C) bond angle of the epoxy group. Intriguingly, the unzipped C₈O has two local minimum points in the relative total energy as a function of *a*, separated by an energy barrier of ~100 meV (Fig. 1b). They represent two stable (or bi-stable) phases, denoted as phase 1 (P1) and phase 2 (P2). Besides the lattice constant, the most noticeable structural difference is the C–O–C bond angle α equal to 133° for P1 and 104° for P2 in Fig. 1f,g. Both P1 and P2 show the unzipped characteristics, because the C–C bonds underneath the oxygen atoms, having a length greater than 2.2 Å, are clearly ruptured.

Supplementary Fig. 1 shows the phonon density of states (DOSs) for both phases⁴³. Based on harmonic approximate, we estimated the free energies of P1 and P2 at 300 K are –158.2925 eV and –158.1958 eV, respectively. P1 is the more stable phase and the free energy difference is 97 meV, moderately increased from 76 meV at zero K (Fig. 1b).

To investigate physical origins of the bi-stable phases, the electronic DOSs of P1 and P2 are shown in Supplementary Fig. 2a,b. There are no obvious differences. A close inspection of the projection density of state (PDOS) of the oxygen atom and its two neighbouring carbon atoms reveals distinctive features near the *E*_F in these two phases. Figure 1e and Supplementary Fig. 2 show clearly overlapped density peaks of *s*- and *p*-electrons at –0.5 eV below the *E*_F in P2, suggesting chemical interactions among the oxygen and its two neighbouring carbon atoms. In contrast, P1 only shows a *p*-electrons density peak of the C atoms near –0.5 eV, instead a similar overlap appears at +0.5 eV above the *E*_F (Fig. 1d).

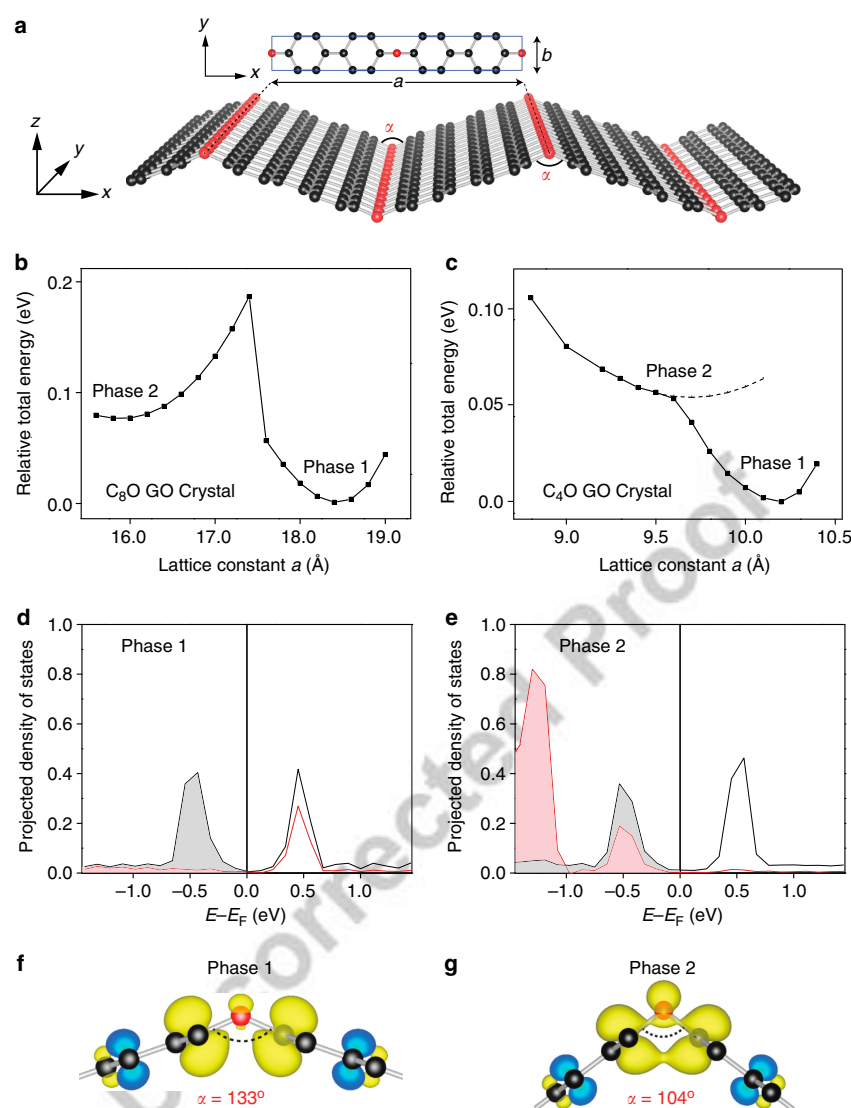


Figure 1 | Bi-stable phases of atomically thin C_8O with ordered epoxy groups. (a) Crystal structure of C_8O with a and b as the lattice constant in x and y axes (rectangular supercells are used). Black and red spheres represent the carbon (C) and oxygen (O) atoms, respectively. Angle α measures the bond angle of oxygen atom and its two neighbouring carbon atoms. The C_8O GO crystal unit cell contains 16 carbon atoms and 2 oxygen atoms. (b) The relative total energy as a function of lattice constant a for C_8O . The two local minimum points represent the two stable phases: phase 1 and phase 2. The lattice constant a of phase 1 and phase 2 C_8O is 18.384 and 15.718 Å, respectively. The lattice constant in y -direction is 2.475 Å for both cases. (c) For a comparison, the relative total energy versus lattice constant a for a similar C_4O crystal. (d,e) The projection density of state (PDOS) results for the two stable phases of C_8O . The black curves represent p-electrons DOS of the carbon atoms and the red curves represent p-electrons DOS of the oxygen atom. The vertical lines represent the Fermi level (E_F). Below E_F , red- and grey-shaded areas indicate occupation of electrons on the p-orbitals of oxygen and carbon atoms, respectively. (f,g) Partial charge density surrounding the oxygen and its neighbouring carbon atoms (within the energy range from -1.0 to 0.0 eV with reference to E_F) for both phase 1 and phase 2 C_8O .

Supplementary Table 1 lists the partial charge density for the oxygen and carbon atoms within an energy range from -20 to 0 eV referenced to E_F . The oxygen atom shows sp^2 hybridization in both phases (Supplementary Note 1). Its two half-filled sp^2 orbitals interact with those of carbon atoms to form two σ bonds. The oxygen atom also has one sp^2 lp distributed within, and one p_y lone pair distributed perpendicular to the C–O–C plane, respectively. Figure 1f,g shows the partial charge density within

the energy range from -1 to 0 eV (with reference to E_F) for both phases. P1 shows strong π orbitals surrounding carbon atoms, which is consistent with the PDOS results in Fig. 1d. In contrast, as shown in Fig. 1g, P2 exhibits a clear mixing/merging between the oxygen sp^2 lp orbital and the carbon π orbitals (lp - π interaction). Based on these evidences, we believe that reducing angle α in P1 (thus the shorter C–C distance beneath the oxygen) promote interactions of π orbitals of the two C atoms

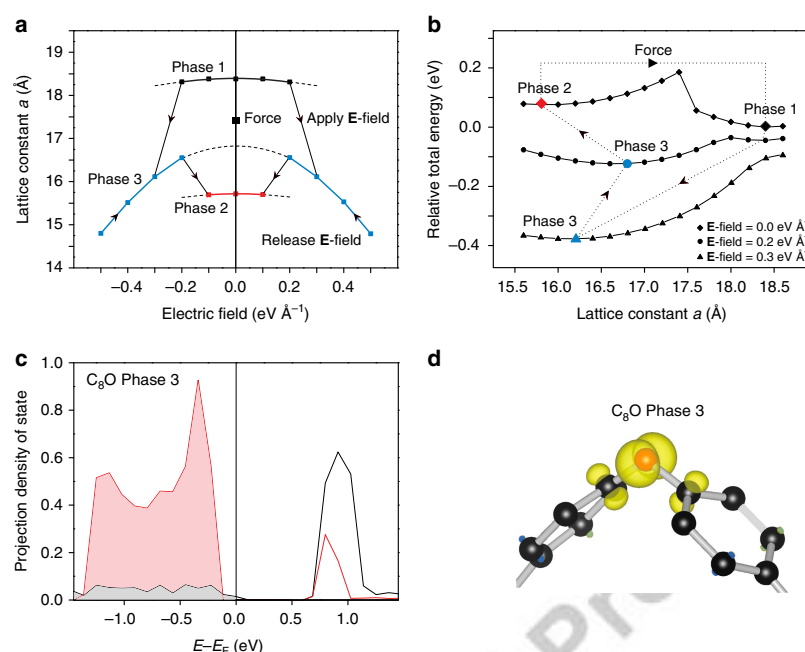


Figure 2 | Reversible phase transition of C₈O triggered by a combination of external E-field and mechanical force. (a) Lattice constant a as a function of the strength of an E-field that is applied perpendicular to the basal plane (that is, z axis in Fig. 1a). The black, blue and red lines represent the phase 1, phase 3 and phase 2, respectively. Black dashed lines indicate the parabolic electrostriction effect of each phase upon external E-field. Applying and releasing an E-field will cause phase transition from P1 to P2. Applying a mechanical force (stretching) will transform C₈O back to P1. (b) Relative total energy as a function of lattice constant a under E-field strength of 0, 0.2 and 0.3 eV Å⁻¹, respectively, to help understand the phase transition from the energetic perspective. The black, red and blue dots represent the fully relaxed crystal structures of P1, P2 and P3 upon applied E-field. The dotted lines with arrows show the cycle of corresponding reversible phase transition. (c) The PDOS results of the oxygen atoms (red) and its neighbouring carbon atoms (black) of C₈O phase 3. The vertical lines represent the E_F . Below E_F , red- and grey-shaded areas indicate occupation of electrons on the p -orbitals of oxygen and carbon atoms, respectively. (d) Partial charge density surrounding the oxygen and its neighbouring carbon atoms within the energy range from -1.0 to 0.0 eV with reference to E_F for phase 3 C₈O. These results are distinctive from those of phase 1 and phase 2 shown in Fig. 1 and Supplementary Fig. 2.

and the empty sp^{2*} lp orbital of oxygen atom (above E_F) in Fig. 1d. A charge transfer takes place from the carbon π orbitals to the oxygen lp orbital, evidenced by a shift of the oxygen p -electron DOS from above the E_F in P1 to below the E_F in P2 (and thus overlaps with the carbon π DOS peaks). Because there are no other notable differences in the DOS and the partial charge density of both phases, we believe that this lp - π interaction stabilizes the P2 phase.

The lp - π interaction is different from the well-known C–O–C ether group (with a bond angle $\alpha \sim 110^\circ$), in which the oxygen atom exhibits sp^3 hybridization. It should also be distinguished from the weak inter-molecular lp - π interaction that has attracted lots of attention in the past two decades owing to its crucial role in several essential phenomena in biological systems, such as protein folding, DNA/RNA stacking and drug–receptor interactions^{44–46}, where the inter-molecular lp - π interaction takes place between π -deficient aromatic rings and lone pair-containing species. The unique lp - π interaction in C₈O exists within a single crystal/molecule and it stems from the π -sufficient carbon interacting with the empty oxygen sp^{2*} lp orbital. We will term it as intra-molecular lp - π bond. Its bond energy can be approximated as the calculated energy barrier value 76 meV (Fig. 1b).

Figure 1c and Supplementary Fig. 3 show the relative total energy versus a , PDOS and partial charge density for the C₄O. The C₄O shares a similar crystal structure as C₈O. The lp - π

interaction is also observed in C₄O (Supplementary Fig. 3b), which tends to stabilize the second phase (Fig. 1c). But it appears not strong enough, as there is no energy barrier to separate P1 and P2 in Fig. 1c. Nevertheless, these results confirm critical role of the lp - π interaction in GO crystals with aligned epoxy groups.

Reversible phase transitions of C₈O and C₄O. Interestingly, our DFT simulations show that applying an external E-field and a mechanical force can lead to a reversible phase transition. In our calculations, the E-field is applied perpendicular to the basal plane (that is, z axis in Fig. 1a) with a magnitude varying from -0.5 to $+0.5$ eV Å⁻¹, which has been demonstrated to be achievable in devices fabricated using two-dimensional graphene-based materials in experiments^{47,48}. The structure is allowed to relax in the x - y plane.

Figure 2a shows the change of the in-plane lattice constant a with varying E-field strength for C₈O. The lattice constant b (y axis) exhibits a negligible change under different E-fields (Supplementary Fig. 4). P1 shrinks in x -direction under a weak E-field, showing a nearly parabolic relation. This could be attributed to the electrostriction effect⁴⁹. At around 0.2 eV Å⁻¹, the lattice constant a has a sudden drop. Beyond this point, the lattice constant a decreases, following another parabolic relation. A subsequent release of the E-field sees a gradual increase of a till ~ 0.2 eV Å⁻¹. Surprisingly, at this critical point, lattice constant

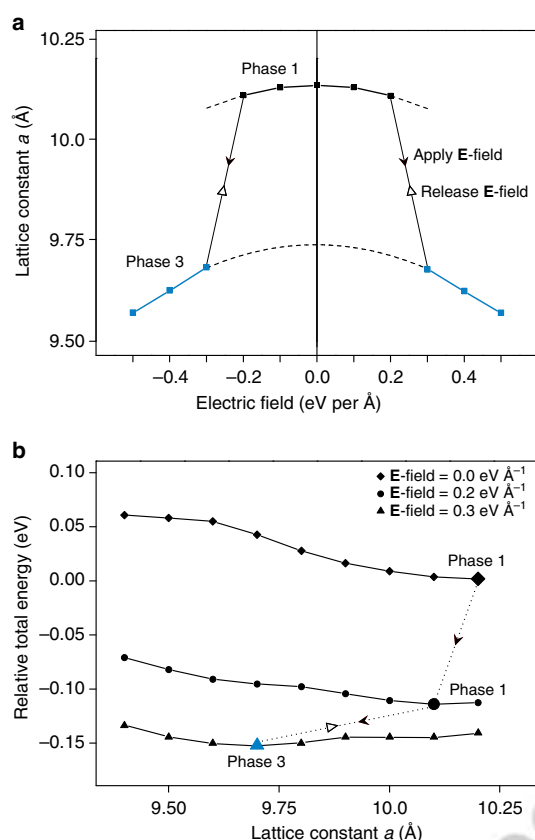


Figure 3 | Phase transition of C₄O triggered by E-field. (a) Lattice constant a as a function of applied E-field strength. The black and blue lines represent phase 1 and phase 3, respectively. Black dashed lines indicate the parabolic electrostriction effect of each phase upon external E-field. Applying E-field on P1 induces a phase transition to P3. Upon releasing the E-field, the C₄O reverts to P1. (b) Relative total energy as a function of lattice constant a under E-field strength of 0, 0.2 and 0.3 eV Å⁻¹, respectively. The black and blue dots represent the fully relaxed crystal structures of P1 and P3 upon applied E-field. The phase 2 is not stable, which is consistent with the result in Fig. 1b. The dotted lines with arrows show the corresponding phase transition.

a drops again and C₈O transits to P2 till completely releasing the E-field. Applying a positive or negative E-field leads to the same results (Fig. 2a) because of the crystal symmetry of C₈O. Then applying a stretching force to P2 gives rise to a phase transition back to P1, closing the loop of a reversible phase transition (Fig. 2a). Applying a stretching force to a two-dimensional material is feasible in experiments⁵⁰.

It is a surprise to observe three parabolic curves in Fig. 2a. The top and bottom curves represent P1 and P2, respectively. The middle one appears to be the third phase. Indeed, the DOS (Supplementary Fig. 5), PDOS and partial charge density (Fig. 2c,d) distinguish it from both P1 and P2. It is thus termed as P3. The band gap of P3, ~0.5 eV, is clearly larger than that of P1 and P2 (Supplementary Fig. 2a,b). From Fig. 2c,d, we find that there is no π orbital of C atoms just below E_F and the π^* orbital is notably more profound than that of P1 and P2. Our DFT results did not show P3 under a zero E-field (Fig. 1b). P3 may be stable only under certain E-fields (Supplementary Note 2).

Through a comparison of the PDOS results of these three phases, P3 appears as a transition state from P1 to P2. The external E-field pushes the E_F to a lower energy level, tending to empty the π orbitals of P1. At the critical point (P1 transition to P3), the emptied π orbital would merge with the π^* orbital, manifested as the more profound π^* orbital in P3. With the release of E-field back to the critical point (P3 transition to P2), electrons would start to refill both π^* orbital of C atoms and the oxygen lp orbital (because they share same energy levels in Fig. 2c), thus forming the $lp-\pi$ bond and stabilizing the P2.

To understand the reversible transition from an energetic perspective, Fig. 2b shows the relative total energy versus a of C₈O under an E-field strength of 0, 0.2 and 0.3 eV Å⁻¹, respectively. Overall, the applied E-field pushes up energy of P1 with respect to another phase. Above the critical E-field strength of 0.2 eV Å⁻¹, the energy barrier starts to disappear. The lower local minimum point at 0.2 eV Å⁻¹ is P3 instead of P2. At 0.3 eV Å⁻¹, the energy barrier diminishes and a spontaneously phase transition takes place as observed in Fig. 2a. Figure 2b also shows that further increasing E-field moves the local minimum energy point of P3 towards a smaller lattice constant, which is consistent to the reduction of a for P3 (Fig. 2a). Then, with releasing the E-field till 0.2 eV Å⁻¹, the lattice constant of P3 increases (Fig. 2a). The local minimum energy points of P3 and P2 are always located to the left of the energy barrier. Re-establishment of the energy barrier as a result of releasing E-field will prevent C₈O from recovering P1 but instead transit to P2.

Same analysis was carried out for C₄O to further verify our understanding of the phase transition. The change of lattice constant a with varying E-field strength is shown in Fig. 3a. Figure 3b summarizes the relative total energy versus a under some typical E-field strength. Like the C₈O (Fig. 2), C₄O P1 gradually shrinks under a small E-field strength. It then undergoes a sudden phase transition to a new phase P3 upon an E-field greater than 0.2 eV Å⁻¹. The DOS and PDOS results of C₄O P3 (Supplementary Fig. 5c,d) are similar to those of C₈O P3. But upon releasing the E-field, the C₄O reverts to P1, owing to the lack of an energy barrier. These consistent evidences reveal common features of structural and electronic properties of these GO crystals with orderly aligned epoxy groups, and the potential of utilizing an E-field to trigger the phase transition.

It is clear that on-or-off state of the $lp-\pi$ bond/interaction determines the reversible phase transition in C₈O. The overall similarity of DOS/PDOS results of both phases (Supplementary Fig. 2 and Supplementary Table 1) and the localized partial charge density near the C–O–C groups in P2 (Fig. 1g) evidently indicate the local nature of this unique bond. It is thus reasonable to observe the local crystal structure changes during a phase transition. This is utterly different from SMAs and SMCs, in which the whole crystal lattice undergoes a transformation, usually resulting in distinctive crystal symmetry and electronic structures of the two phases³. Interestingly, the local intramolecular $lp-\pi$ bond is analogous to state-of-the-art design concept of SMPs—molecular switch⁵¹ in which switching on-or-off some local inter-molecular bonds in polymer networks enables fixing of temporary shapes or recovery of the original shape. Thus, we term the $lp-\pi$ bond as $lp-\pi$ switch, which could provide fresh ideas in the design of SMMs at nanometre scale, benefiting from the knowledge obtained in SMP research field.

Shape memory C₈O. This reversible phase transition in C₈O enables the highly desirable SME. A shape memory cycle is divided into two steps, namely shape fixing and shape recovery¹⁹. Figure 4 demonstrates these two steps for C₈O. Taking P1 as the permanent shape (Fig. 4a), the E-field can be used as the external

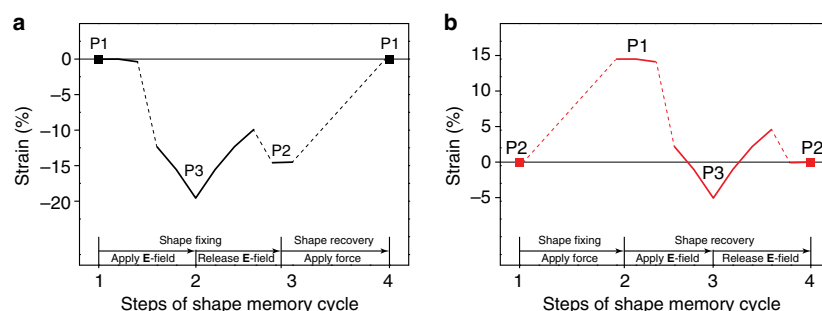


Figure 4 | A full shape memory cycle for C_8O . (a) Case 1: taking P1 as the permanent phase. An **E**-field is used as stimuli for shape fixing, where mechanical force is applied for shape recovery. The horizontal line represents zero strain with reference to P1. The maximum recoverable contraction strain is 14.5% and the maximum intermediate contraction is 19.4% that takes place at **E**-field strength of $0.5 \text{ eV } \text{\AA}^{-1}$. (b) Case 2: taking P2 as permanent phase. An applied stretching force is used to fix temporary shape (P1) and an **E**-field triggers the shape recovery. The horizontal line represents zero strain with reference to P2. The maximum recoverable expansion strain is $\sim 17\%$. It is worth noting that the recovery step shows a discontinuous shape change, which is a signature of the multi-SME. The dashed lines connect different phases at different steps as a guide for the shape memory cycle.

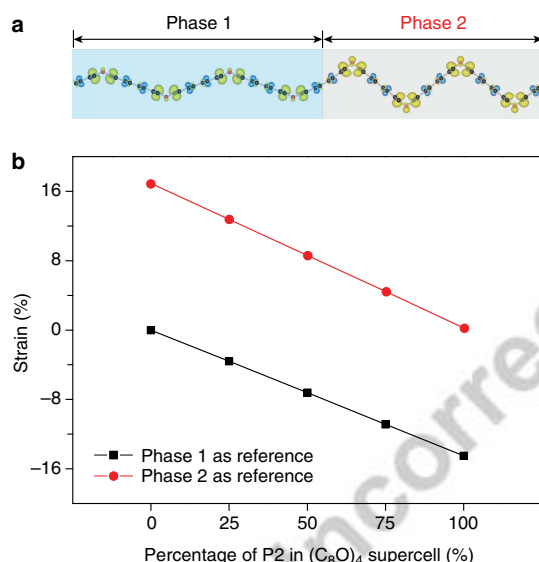


Figure 5 | Stable co-existence of P1 and P2 in one supercell from DFT simulations, implying multiple temporary shapes achievable in one piece of material—programmability. (a) A stable four-unit supercell in DFT simulations that includes two units of P1 and two units of P2. The signature partial charge density of the local $lp-\pi$ bonds in P2 can be clearly seen.

Other P1/P2 mixing cases in this four-unit supercell are presented in Supplementary Fig. 6. (b) The recoverable strain results of all possible temporary shapes from a four-unit supercell via programming the percentage of P2 (Supplementary Table 2a). The strain value is calculated corresponding to the two cases represented in Fig. 4, where the first case takes P1 as the permanent shape and the second case takes P2 as the permanent shape.

stimuli to fix the temporary shape (P2). The recoverable contraction strain arising from this shape-fixing step is $\sim 14.5\%$. This value is much higher than most of the SMAs (less than 8%)³. The shape recovery can be activated by a mechanical stretching force. In novel applications such as material-as-machine at nanometre scale, using **E**-field for temporary shape fixing is more practical in comparison with other common stimuli like mechanical force.

Most SMMs can only memorize one temporary shape in one shape memory cycle. A current research interest is to develop multi-SME that can exhibit more than one distinctive shape change in the recovery step. The resultant multi-SME provides much better controllability and more flexible shape morphing ability^{51,52}. Thanks to its three different phases, C_8O could have a triple-SME. As illustrated in Fig. 4b, taking P2 as the permanent shape, C_8O can be pre-stretched and fixed to its first temporary shape P1 using a mechanical force. In the recovery step, applying and releasing an **E**-field will observe a lattice reduction, then an expansion and finally a reduction to the final permanent shape. Such a discontinuous shape change is recognized as signature of the multi-SME⁵¹. The triple-SME C_8O could enable rich design possibilities in practices.

The most important feature to distinguish SMMs from other stimuli-responsive shape change material is the programmability⁵¹. In other words, one piece of SMM can be programmed/fixed into different temporary shapes. The co-existence of different phases and variants in one SMM is the key to achieve programmability, because different types and ratio of combinations allow tailoring the microstructures for multiple temporary shapes. On this wise, the co-existence of both P1 and P2 were carefully examined in our DFT simulations. Several supercells were created to incorporate different numbers and distribution patterns of P1 and P2 (Fig. 5 and Supplementary Fig. 6). As an example, Fig. 5a illustrates the supercell including two units of P1 and two units of P2 (2/2). Our DFT calculations conclude stability of all these coherently mixed P1/P2 phases. The signature partial charge density of $lp-\pi$ bonds can be observed in the supercells, further confirming its local nature. The stability of various P1/P2 mixing can be attributed to this local chemical bond.

We propose that in applications at nanoscale, an STM or AFM tip can be employed to apply a local **E**-field or local point force to tune different mixtures of P1/P2 for the desirable temporary shapes. As a simple illustration, Fig. 5b and Supplementary Table 2a summarize the lattice constants of all possible temporary shapes of a supercell including four unit cells of C_8O (different P2 percentage) and the programmable recoverable strain results. Larger supercells including six unit cells of C_8O are also examined and results are summarized in Supplementary Fig. 7 and Supplementary Table 2b. All these evidences confirm the programmability of C_8O SMM.

The maximum elastic strain and specific modulus (ratio of elastic modulus over mass density) are often chosen as the key

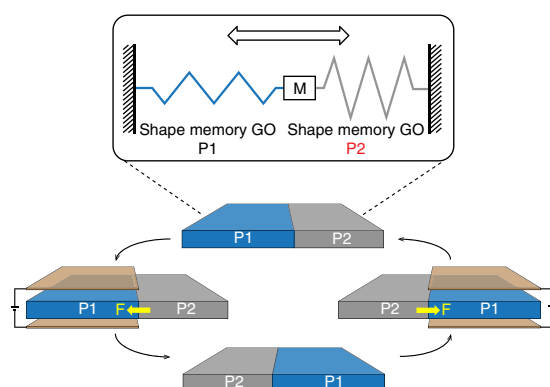


Figure 6 | A simple prototype design of a two-way actuator using shape memory C_8O . The actuator includes one mass element (M) and two segments of shape memory C_8O . The two phases P1 and P2 are indicated as blue and grey region, respectively. Applying an **E**-field on the P1 segment will cause a phase transition to P2, generating a shrinkage deformation and thus a stretching force to the P2 segment. As long as the force is large enough (for example, $0.5 \text{ eV } \text{\AA}^{-1}$), a simultaneous phase transition from P2 to P1 will take place (Supplementary Fig. 9). Element M in the middle may move back and forth if applying the **E**-field alternatively on either segment, as indicated by the arrow.

parameters to assess the mechanical properties of materials. Leng *et al.* surveyed available SMMs in a review article¹⁹. Generally, a SMM with a large maximum recoverable strain usually had a low specific modulus and thus concluded an upper bound (Supplementary Fig. 8). At its maximum recoverable strain of 14.5%, our C_8O has a specific modulus about ten times higher than the upper bound. Given the same specific modulus $4.3 \text{ GPa cm}^3 \text{ g}^{-1}$, C_8O has a maximum recoverable strain approximately threefold larger than the upper bound. Another important practical consideration is the actuation frequency. Commonly used thermal-responsive SMMs exhibit small actuation frequencies $\sim 1 \text{ Hz}$, which is recognized as a bottleneck, severely restricting their applications. The required external stimuli of C_8O SMM (that is, **E**-field and mechanical force) should, in principle, allow much higher actuation frequencies.

At the end of this section, we propose a simple prototype design of two-way actuator based on C_8O SMM (Fig. 6). In this design, two segments of C_8O (one in P1 and the other one in P2) are connected to the opposite sides of a mass element M, whereas the other end is fixed. Applying a local **E**-field to the P1 C_8O (left segment in Fig. 6) will cause it to contract and consequently generate a stretching force **F** on M and then to the P2 C_8O (right segment in Fig. 6). As long as the applied **E**-field strength is sufficiently high, for example, $0.5 \text{ eV } \text{\AA}^{-1}$ (Supplementary Fig. 9), the generated force can transform the right segment from P2 to P1. As a result, phases of the left and right segments swap as illustrated in Fig. 6. Applying the **E**-field alternatively on either segment can generate a repeated back and forth linear motion of element M (Supplementary Note 3). A clear advantage of this design is that only an **E**-field is required to trigger the shape memory cycle and operate this actuator, which is feasible and highly desirable for designs of nano-mechanical devices.

Discussion

From a practical perspective, it is imperative to discuss the finite temperature effects. Using molecular dynamics simulations, Huang *et al.* simulated the thermal fluctuation of a C_8O structure

with linear alignment of epoxy groups on single side of graphene layer at 1,500 K and concluded no structural destruction³⁵. Our C_8O has a lower total energy than that in Huang's study. It should have good structural stability at room temperature. In addition, thermal fluctuation causes out-of-plane distortion of a suspended two-dimensional materials, which could compromise the control of in-plane strain in applications of our SMM C_8O . This effect can be controlled by appropriate designs. Xu *et al.* reported that thermally excited out-of-plane distortion of a suspended graphene or chemically functionalized graphene depended on its length-to-width ratio. At room temperature, for a graphene layer with an edge length of 50 nm and an aspect ratio of one, the out-of-plane displacement is on the order of 2 \AA (ref. 53). In Huang's simulations, thermally induced out-of-plane ripple in a C_8O periodic supercell (aspect ratio close to 1 and supercell edge length approximately 41 \AA) was around 2.5 \AA at 1500 K (ref. 35), from which the distortion can be estimated as 1 \AA at 300 K. Fasolino *et al.* used molecular dynamics simulations to study the intrinsic thermally excited ripples in a sufficiently large graphene supercell and found a ripple magnitude of 0.7 \AA and a wave length of $\sim 80 \text{ \AA}$ (ref. 54). These out-of-plane displacements are small in comparison with the lateral size or ripple wave length. Thus, control of the aspect ratio is a very convenient means to suppress this distortion. Another option is to use a substrate, which will be discussed later.

To examine the structure and phase stability of our C_8O SMM in atmosphere, four types of gas molecules, O_2 , CO_2 , H_2O and N_2 , were added in the supercells of P2 C_8O . The P2 C_8O was selected because its weak $lp-\pi$ bond could be affected by the gas molecules. The crystal structure and partial charge density results in Supplementary Fig. 10a–d demonstrate negligible effects. We, therefore, expect that the SME remains valid in atmosphere. Nevertheless, despite the negligible effect of water molecules on the $lp-\pi$ bonds, the hydrogen-rich or humid environment should be avoided because hydrogen can transform epoxy groups to hydroxyl groups^{32,34}.

A substrate is required in many applications. Supplementary Fig. 11 shows the equilibrium crystal structure and partial charge density results of P1 and P2 on top of a graphene nano-ribbon substrate. In comparison with Fig. 1, there are no notable differences. In addition, our DFT results show that the energetic order of these two structures is swapped by applying an external **E**-field of $0.3 \text{ eV } \text{\AA}^{-1}$. The **E**-field induced phase transition, therefore, should take place (Supplementary Note 4).

The bi-layered structures were also investigated in our DFT simulations. Bi-stable phases are observed (Supplementary Fig. 12). The P1 crystal structure resembles the monolayer case. Interestingly, two types of C–O–C angles, 130.3° and 106.3° , are distributed alternatively along the x axis in the metastable phase. Together with the partial charge analysis, we can conclude this metastable phase consisting of both P1 and P2 components of the monolayer C_8O . The total energy difference of these two phases (128 meV) is close to the monolayer C_8O (76 meV). These evidences suggest that **E**-field and stress could lead to phase transition and thus the SME in bi-layered C_8O .

Next, we consider the influence of some typical defects. First, previous studies suggested that a mixing pattern of C_8O and C_4O could exist^{35,41}. A supercell was then constructed to include one unit cell of C_8O and C_4O in x axis direction (Supplementary Fig. 13). Our DFT calculations identified two stable structures. We also found that tuning the **E**-field could change the energetic order of these two structures, suggesting a phase transition triggered by **E**-field.

Regarding the epoxy lines, there are two common defects: oxygen vacancy and redundant oxygen adatom. These two types of defects were produced in supercells of perfect P1 and P2 phases

ARTICLE

NATURE COMMUNICATIONS | DOI: 10.1038/ncomms11972

of a size of 1×5 , 1×7 and 1×9 , respectively, to account for different defect concentrations (20%, 15% and 11%, respectively). The oxygen vacancy was generated by removing one epoxy group from the supercells (Supplementary Fig. 14). The redundant oxygen adatom was introduced in the supercells to form either epoxy pair or carboxyl pair (Supplementary Fig. 15). These defects cause local structural distortions only up to the first nearest-neighbour epoxy group. The P1 and P2 supercells remain stable as long as the defect concentration is lower than 20% (or epoxy line is longer than 1.2375 nm). The signature $lp-\pi$ bonds appear in partial charge density of the P2 supercells (beyond the first nearest neighbour of defects). Supplementary Note 5 provides detailed descriptions. We can expect that at a reasonable defect density (for example, smaller than 20%), these defects should have negligible influences on the SME of our C_8O SMM.

In the following, we will discuss possible fabrication routes of C_8O SMM in experiments. The first step is to achieve homogeneous functionalization of epoxy groups on graphene. The widely used Hummers method usually leads to chemical inhomogeneity of oxygen functional groups, making this choice unfavourable. There are two promising alternative ways. Recently, Hossain *et al.* reported that oxidation of epitaxial graphene using atomic oxygen in ultrahigh-vacuum produced uniform epoxy functionalization³⁶. Another route is to use vacuum thermal annealing process to remove functional groups other than epoxy³³.

The next step is to realize the linear alignment of epoxy groups. This topic has attracted many studies in the past for the purpose of unzipping graphene layers^{38,39,55–57}. DFT simulations indicated that linear alignment could effectively reduce strains in a graphene layer caused by the epoxy groups. Huang *et al.* employed DFT calculations and cluster expansion approach to explore a configuration space including $\sim 17,000$ different GO structures. Interestingly, they concluded that a C_8O crystal structure with well-ordered linear pattern of epoxy group is the ground-state structure provided that graphene is oxidized in one side³⁵. These theoretical studies provide a solid thermodynamic ground for fabricating GO with well-ordered epoxy lines. In their study of growth mechanisms, Sun *et al.* found that the formation of an epoxy linear trimer would attract and trap nearby oxygen adatom to diffuse to the end of trimer, leading to the growth of an epoxy line⁵⁵. To guide growth direction, there are several options. One possibility is to apply uniaxial strain in graphene layer to break symmetry of the honeycomb structure. This can be done by placing a pristine graphene on a flexible substrate and then either stretching or bending the substrate. Ma *et al.* found that the uniaxial strain can reduce the reaction energy barrier to promote growth of epoxy lines along certain directions⁵⁷. The second option is to generate periodic rippling in graphene layers via mechanical compression. Residual strain on the ripple ridges would make the C–C bonds more reactive to oxygen adatoms to form the linear epoxy chains. Our recent theoretical study showed that the rippling wavelength could be controlled down to 1 nm range, which can match the periodicity of C_8O (ref. 58). The third option is to take advantage of the experimental techniques from Hossain *et al.*, in which STM tips were used to induce desorption of chemisorbed oxygen, move oxygen adatoms and thus pattern the epoxy groups at atomic precision on graphene layers³⁶. It is plausible to use STM tips to pattern parallel epoxy trimmers and subsequent oxidation will lead to spontaneous growth of epoxy lines. All three options can be combined with the vacuum oxidation setup from Hossain *et al.* The first and second option could be combined with the vacuum annealing method from Mattson *et al.*³³.

Note that in these previous studies^{38,39,55–57}, some further steps were required to unzip the GO with linear epoxy chains into

nano-ribbons. For instance, Fujii's experiment used an AFM tip to press the oxidized graphene layers and the resultant local stress led to the structural rupture. Ma *et al.* suggested that further oxidation of the epoxy chains would lead to unzipping⁵⁷. Clearly, these extra experimental steps are not needed for our case.

In summary, this paper reports a two-dimensional shape memory C_8O triggered by E-field and mechanical force. A unique chemical bond, $lp-\pi$ interaction, is revealed as the physical origin of the SME. Besides traditional single SME, an interesting triple SME is also achievable. The overall mechanical properties of the shape memory C_8O are significantly better than those of currently available SMMs. In addition, the E-field and mechanical force stimuli could overcome the limitations (such as, actuation frequency only about 1 Hz) of commonly employed thermal stimuli at small size scales.

Methods

The Vienna *ab initio* simulation package (VASP v.5.3.3) was used to perform DFT calculations in this study. Projector augmented wave method and the generalized gradient approximation were employed^{59,60}. A plane-wave cutoff energy was set as 800 eV. A Monkhorst-Pack gamma-centred k -points mesh of $42 \times 6 \times 1$ was adopted for C_8O unit cell (Fig. 1a). A similar k point mesh density was adopted for other supercells. As periodic boundary conditions were employed in VASP, thick vacuum layers were included to minimize interlayer interactions. An interlayer spacing of 20 Å was used throughout, which represents a good balance between computational accuracy and efforts. To hold this interlayer space constant, the VASP source code (constr_cell_relax.F) was modified to allow the cells to relax within the basal plane only. In all cases, the atomic positions were allowed to relax in all directions. Before being subjected to an external E-field, all structures were fully relaxed to determine their equilibrium lattice constants. The relative change of in-plane lattice constants under an applied E-field with respect to the equilibrium values were defined as deformation strain. The dipole and quadrupole corrections were adopted for all our simulations. We used VASP and Phonopy-1.10 to calculate phonon frequency⁴³.

Data availability. The data that support the findings of this study are available from the corresponding author upon request.

References

- Otsuka, K. & Wayman, C. M. *Shape Memory Materials* (Cambridge Univ., 1999).
- Wu, X. *et al.* Mechanisms of the shape memory effect in polymeric materials. *Polymers* **5**, 1169–1202 (2013).
- Jani, J. M., Leary, M., Subic, A. & Gibson, M. A. A review of shape memory alloy research, applications and opportunities. *Mater. Design* **56**, 1078–1113 (2014).
- Zhang, J. *et al.* A nanoscale shape memory oxide. *Nat. Commun.* **4**, 2768 (2013).
- Hager, M. D., Bode, S., Weber, C. & Schubert, U. S. Shape memory polymers: past, present and future developments. *Progr. Polymer Sci.* **49**, 3–33 (2015).
- Behl, M., Kratz, K., Zotzmann, J., Nöchel, U. & Lendlein, A. Reversible bidirectional shape-memory polymers. *Adv. Mater.* **25**, 4466–4469 (2013).
- Sun, L. *et al.* Stimulus-responsive shape memory materials: a review. *Mater. Design* **33**, 577–640 (2012).
- Liu, Y., Du, H., Liu, L. & Leng, J. Shape memory polymers and their composites in aerospace applications: a review. *Smart Mater. Struct.* **23**, 023001 (2014).
- Bhattacharya, K. & James, R. D. The material is the machine. *Science (Washington)* **307**, 53 (2005).
- Huang, W. *et al.* Shape memory materials. *Mater. Today* **13**, 54–61 (2010).
- Shaw, G. A., Stone, D. S., Johnson, A. D., Ellis, A. B. & Crone, W. C. Shape memory effect in nanoindentation of nickel–titanium thin films. *Appl. Phys. Lett.* **83**, 257 (2003).
- Wang, Z. *et al.* Programmable, pattern-memorizing polymer surface. *Adv. Mater.* **23**, 3669–3673 (2011).
- Shah, A. A., Schultz, B., Zhang, W., Glotzer, S. C. & Solomon, M. J. Actuation of shape-memory colloidal fibres of Janus ellipsoids. *Nat. Mater.* **14**, 117–124 (2015).
- Zhang, Z. *et al.* Nonhysteretic superelasticity of shape memory alloys at the nanoscale. *Phys. Rev. Lett.* **111**, 145701 (2013).
- Asaka, K., Hirotsu, Y. & Tadaki, T. Structure of nanometer-sized Au–Cd alloy particles near equiatomic compositions at room temperature. *Mater. Sci. Engin. A* **312**, 232–236 (2001).
- Waitz, T., Kazykhanov, V. & Karnthaler, H. Martensitic phase transformations in nanocrystalline NiTi studied by TEM. *Acta Mater.* **52**, 137–147 (2004).

17. Seki, K., Kura, H., Sato, T. & Taniyama, T. Size dependence of martensite transformation temperature in ferromagnetic shape memory alloy FePd. *J. Appl. Phys.* **103**, 063910 (2008).
18. Lines, M. E. & Glass, A. M. *Principles and Applications of Ferroelectrics and Related Materials* (Oxford Univ., 1977).
19. Leng, J., Lan, X., Liu, Y. & Du, S. Shape-memory polymers and their composites: stimulus methods and applications. *Prog. Mater. Sci.* **56**, 1077–1135 (2011).
20. Novoselov, K. S. *et al.* Electric field effect in atomically thin carbon films. *Science* **306**, 666–669 (2004).
21. Lee, C., Wei, X., Kysar, J. W. & Hone, J. Measurement of the elastic properties and intrinsic strength of monolayer graphene. *Science* **321**, 385–388 (2008).
22. Suk, J. W., Piner, R. D., An, J. & Ruoff, R. S. Mechanical properties of monolayer graphene oxide. *ACS Nano* **4**, 6557–6564 (2010).
23. Geim, A. K. Graphene: status and prospects. *Science* **324**, 1530–1534 (2009).
24. Raccichini, R., Varzi, A., Passerini, S. & Scrosati, B. The role of graphene for electrochemical energy storage. *Nat. Mater.* **14**, 271–279 (2015).
25. Joshi, R. *et al.* Precise and ultrafast molecular sieving through graphene oxide membranes. *Science* **343**, 752–754 (2014).
26. Rogers, G. W. & Liu, J. Z. High-performance graphene oxide electromechanical actuators. *J. Am. Chem. Soc.* **134**, 1250–1255 (2011).
27. Chandrakumara, G. G. *et al.* Tuning the oxygen functional groups in reduced graphene oxide papers to enhance the electromechanical actuation. *RSC Adv.* **5**, 68052–68060 (2015).
28. Trung, T. Q. *et al.* A flexible reduced graphene oxide field-effect transistor for ultrasensitive strain sensing. *Adv. Funct. Mater.* **24**, 117–124 (2014).
29. Cai, W. *et al.* Synthesis and solid-state NMR structural characterization of ¹³C-labeled graphite oxide. *Science* **321**, 1815–1817 (2008).
30. Casabianca, L. B. *et al.* NMR-based structural modelling of graphite oxide using multidimensional ¹³C solid-state NMR and ab initio chemical shift calculations. *J. Am. Chem. Soc.* **132**, 5672–5676 (2010).
31. Bagri, A. *et al.* Structural evolution during the reduction of chemically derived graphene oxide. *Nat. Chem.* **2**, 581–587 (2010).
32. Zhou, S. & Bongiorno, A. Origin of the chemical and kinetic stability of graphene oxide. *Sci. Rep.* **3**, 2484 (2013).
33. Mattson, E. C. *et al.* Evidence of nanocrystalline semiconducting graphene monoxide during thermal reduction of graphene oxide in vacuum. *ACS Nano* **5**, 9710–9717 (2011).
34. Kim, S. *et al.* Room-temperature metastability of multilayer graphene oxide films. *Nat. Mater.* **11**, 544–549 (2012).
35. Huang, B., Xiang, H., Xu, Q. & Wei, S.-H. Overcoming the phase inhomogeneity in chemically functionalized graphene: the case of graphene oxides. *Phys. Rev. Lett.* **110**, 085501 (2013).
36. Hossain, M. Z. *et al.* Chemically homogeneous and thermally reversible oxidation of epitaxial graphene. *Nat. Chem.* **4**, 305–309 (2012).
37. Pandey, D., Reifenger, R. & Piner, R. Scanning probe microscopy study of exfoliated oxidized graphene sheets. *Surface Sci.* **602**, 1607–1613 (2008).
38. Fujii, S. & Enoki, T. Cutting of oxidized graphene into nanosized pieces. *J. Am. Chem. Soc.* **132**, 10034–10041 (2010).
39. Li, J.-L. *et al.* Oxygen-driven unzipping of graphitic materials. *Phys. Rev. Lett.* **96**, 176101 (2006).
40. Lahaye, R., Jeong, H., Park, C. & Lee, Y. Density functional theory study of graphite oxide for different oxidation levels. *Phys. Rev. B* **79**, 125435 (2009).
41. Xu, Z. & Xue, K. Engineering graphene by oxidation: a first-principles study. *Nanotechnology* **21**, 2 (2010).
42. Boukhvalov, D. W. & Katsnelson, M. I. Modeling of graphite oxide. *J. Am. Chem. Soc.* **130**, 10697–10701 (2008).
43. Togo, A. & Tanaka, I. First principles phonon calculations in materials science. *Scripta Mater.* **108**, 1–5 (2015).
44. Stollar, E. J. *et al.* Unconventional interactions between water and heterocyclic nitrogens in protein structures. *Proteins* **57**, 1–8 (2004).
45. Egli, M. & Sarkhel, S. Lone pair-aromatic interactions: to stabilize or not to stabilize. *Acc. Chem. Res.* **40**, 197–205 (2007).
46. Mooibroek, T. J., Gamez, P. & Reedijk, J. Lone pair- π interactions: a new supramolecular bond? *CrystEngComm* **10**, 1501–1515 (2008).
47. Zhang, Y. *et al.* Direct observation of a widely tunable bandgap in bilayer graphene. *Nature* **459**, 820–823 (2009).
48. Ong, M. T. & Reed, E. J. Engineered piezoelectricity in graphene. *ACS Nano* **6**, 1387–1394 (2012).
49. Chang, Z., Yan, W., Shang, J. & Liu, J. Z. Piezoelectric properties of graphene oxide: a first-principles computational study. *Appl. Phys. Lett.* **105**, 023103 (2014).
50. Perez Garza, H. H., Kievit, E. W., Schneider, G. F. & Stauffer, U. Controlled, reversible, and nondestructive generation of uniaxial extreme strains (>10%) in graphene. *Nano Lett.* **14**, 4107–4113 (2014).
51. Zhao, Q., Qi, H. J. & Xie, T. Recent progress in shape memory polymer: new behavior, enabling materials, and mechanistic understanding. *Prog. Polymer Sci.* **49**, 79–120 (2015).
52. Xie, T. Tunable polymer multi-shape memory effect. *Nature* **464**, 267–270 (2010).
53. Xu, Z. & Buehler, M. J. Geometry controls conformation of graphene sheets: membranes, ribbons, and scrolls. *ACS Nano* **4**, 3869–3876 (2010).
54. Fasolino, A., Los, J. & Katsnelson, M. I. Intrinsic ripples in graphene. *Nat. Mater.* **6**, 858–861 (2007).
55. Sun, T. & Fabris, S. Mechanisms for oxidative unzipping and cutting of graphene. *Nano Lett.* **12**, 17–21 (2011).
56. Li, Z., Zhang, W., Luo, Y., Yang, J. & Hou, J. G. How graphene is cut upon oxidation? *J. Am. Chem. Soc.* **131**, 6320–6321 (2009).
57. Ma, L., Wang, J. & Ding, F. Strain-Induced Orientation-Selective Cutting of Graphene into Graphene Nanoribbons on Oxidation. *Angew. Chem. Int. Ed.* **51**, 1161–1164 (2012).
58. Ren, M., Liu, Y., Liu, J. Z., Wang, L. & Zheng, Q. Anomalous elastic buckling of layered crystalline materials in the absence of structure slenderness. *J. Mech. Phys. Solids* **88**, 83–99 (2016).
59. Kresse, G. & Furthmüller, J. Efficient iterative schemes for ab initio total-energy calculations using a plane-wave basis set. *Phys. Rev. B* **54**, 11169 (1996).
60. Kresse, G. & Joubert, D. From ultrasoft pseudopotentials to the projector augmented-wave method. *Phys. Rev. B* **59**, 1758 (1999).

Acknowledgements

J.Z.L., Z.C., G.G.C. and W.Y. gratefully acknowledge support from the Australian Research Council. J.D. thanks the support from the 973-Project of China (grant No. 2012CB619401), National Science Foundation of China (grant Nos. 51471126, 51320105014, 51321003, 51431007) and the MOE innovation team (grant No. IRT13034) from Ministry of Education of China. The simulation work was carried out using high-performance computing facilities from the National Computational Infrastructure through the NCMAS scheme.

Author contributions

J.Z.L. and Z.C. conceived this project. Z.C., J.D. and G.G.C. conducted the simulation and analysis. The manuscript was prepared by Z.C. and J.Z.L. with inputs from J.D., G.G.C. and W.Y.

Additional information

Supplementary Information accompanies this paper at <http://www.nature.com/naturecommunications>

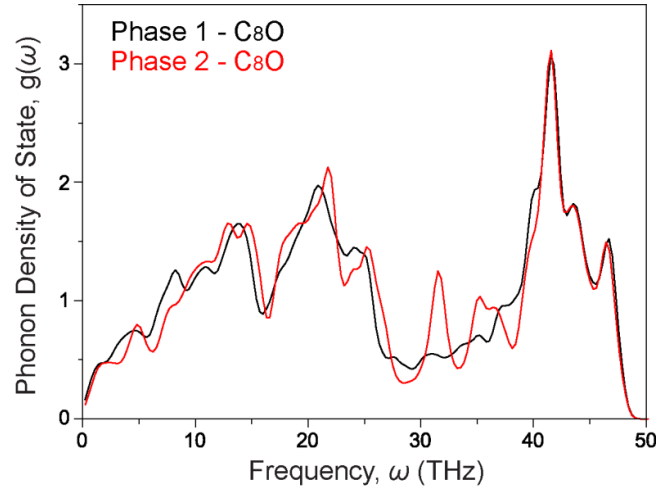
Competing financial interests: The authors declare no competing financial interests.

Reprints and permission information is available online at <http://npg.nature.com/reprintsandpermissions/>

How to cite this article: Chang, Z. *et al.* Two-dimensional shape memory graphene oxide. *Nat. Commun.* **7**:11972 doi: 10.1038/ncomms11972 (2016).

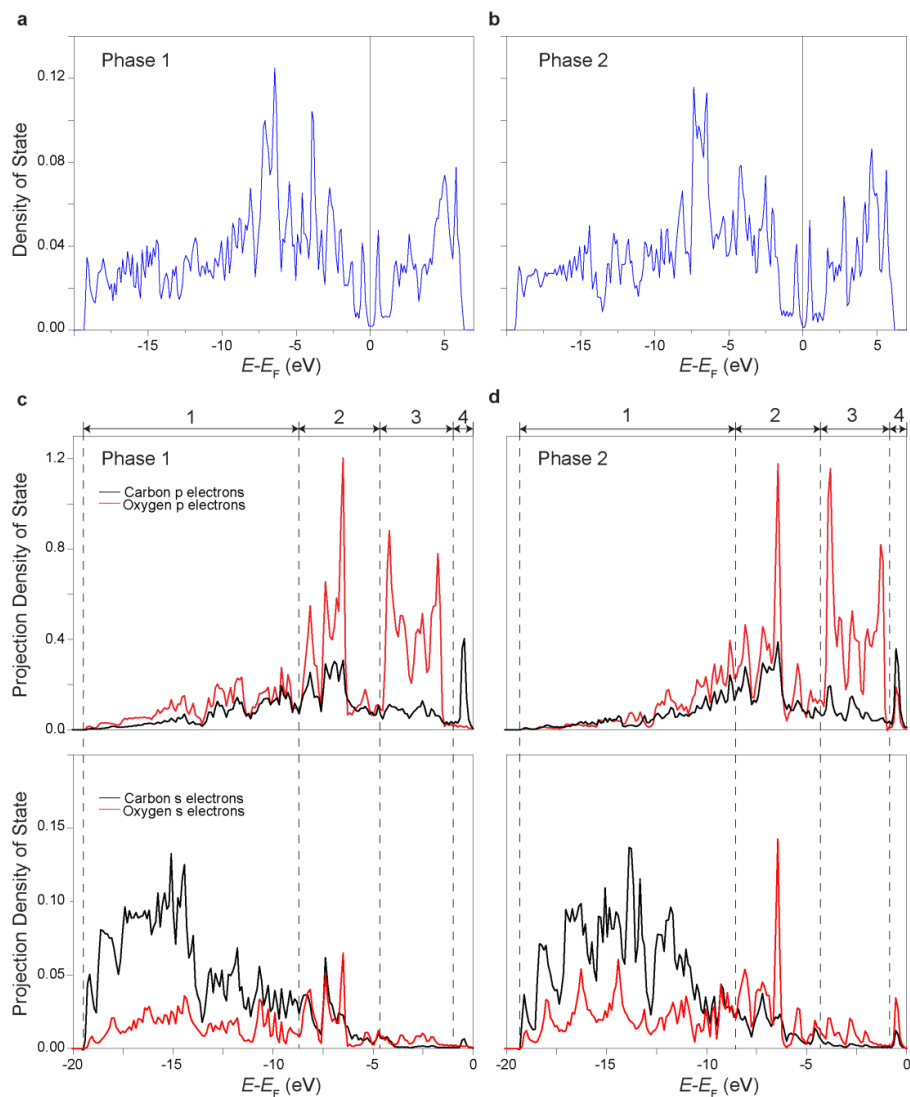


This work is licensed under a Creative Commons Attribution 4.0 International License. The images or other third party material in this article are included in the article's Creative Commons license, unless indicated otherwise in the credit line; if the material is not included under the Creative Commons license, users will need to obtain permission from the license holder to reproduce the material. To view a copy of this license, visit <http://creativecommons.org/licenses/by/4.0/>

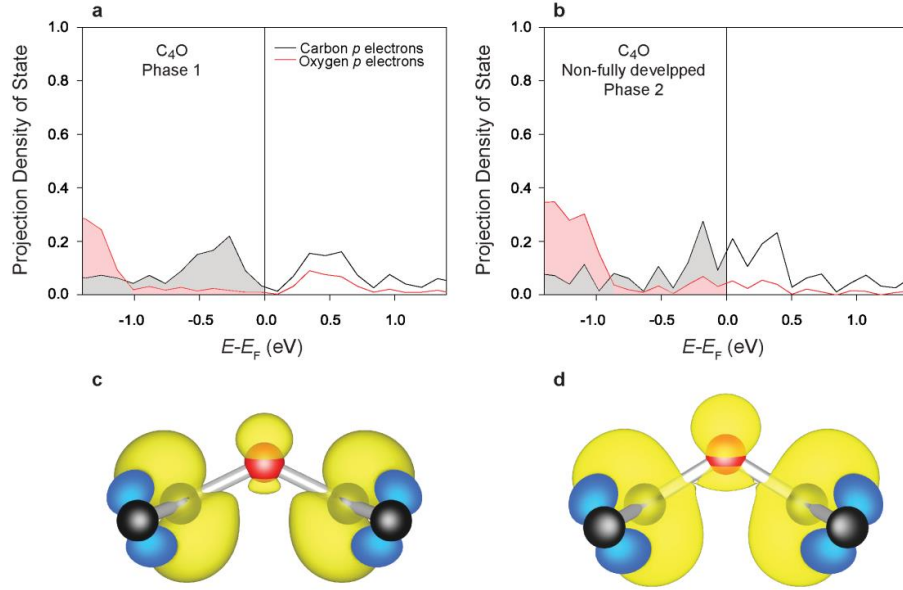


Supplementary Figure 1: Phonon density of states ($g(\omega)$) vs. frequency(ω). As indicated, the black and red lines represent for P1 and P2-C₈O GO. Based on Supplementary Equation 1 shown below,¹ the calculated phonon free energy using harmonic approximation is -0.836 and -0.816 eV, respectively.

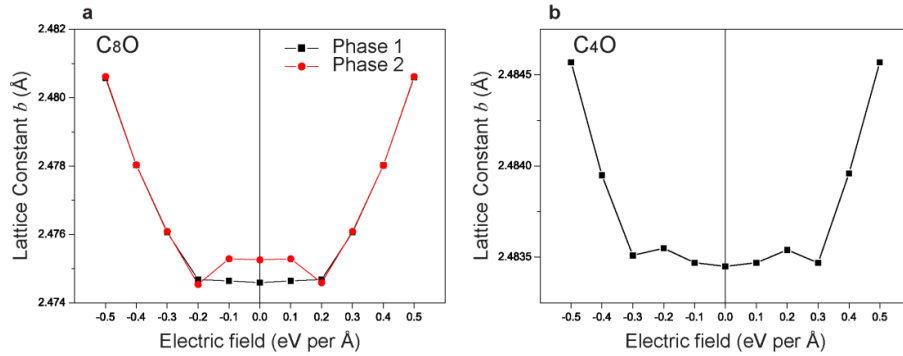
$$E_{\text{free}} = Nk_B T \int_0^{\omega_{\text{max}}} \ln \left[2 \sinh \left(\frac{\hbar \omega}{2k_B T} \right) \right] g(\omega) d\omega \quad \text{Supplementary Equation 1}$$



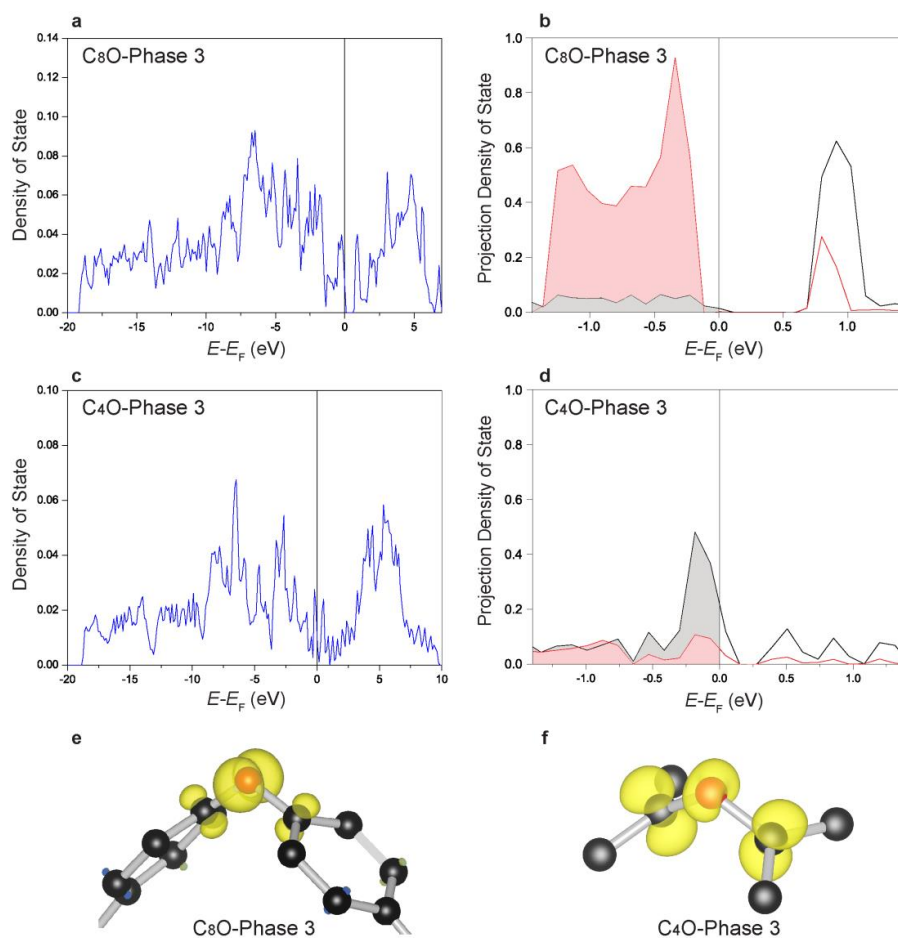
Supplementary Figure 2: The density of state (DOS) and projection density of state (PDOS) for bi-stable phases of CsO. (a, b) DOS of Phase 1 and Phase 2, respectively. (c, d) The *p*-electrons and *s*-electrons PDOS of oxygen atom (red) and its neighbouring carbon atoms (black) of Phase 1 and Phase 2, respectively. The energy levels are divided into four regions (separated by the dashed lines) with reference to E_F , indicated as 1, 2, 3 and 4 in (c, d). The partial charge density of these four regions is shown in Supplementary Table 1.



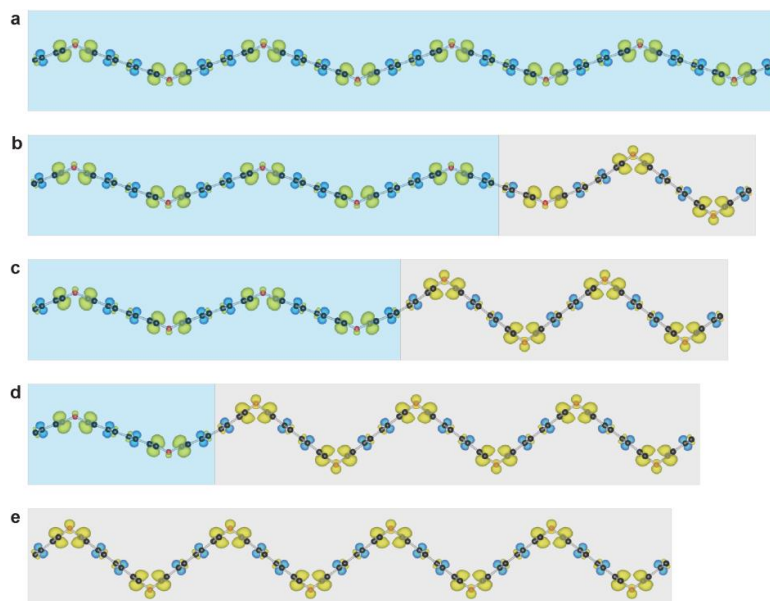
Supplementary Figure 3: The PDOS and partial charge density distribution of C_4O crystal. (a) The p -electrons of oxygen atom (red) and its neighbouring carbon atoms (black) of Phase 1. (b) The p -electrons of oxygen atom (red) and its neighbouring carbon atoms (black) of non-fully developed Phase 2. The vertical lines represent the Fermi level (E_F). Below E_F , red and grey shaded areas indicate occupation of electrons on the p -orbitals of oxygen and carbon atoms, respectively. (c) and (d) Partial charge density of the corresponding PDOS within the energy range from -1.0 to 0.0 eV with reference to E_F .



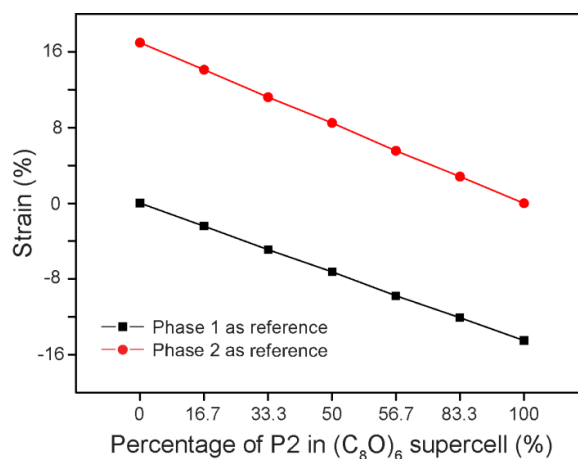
Supplementary Figure 4: Lattice constant b as a function of the applied E-field for C_8O and C_4O . (a) C_8O : The black line is for Phase 1 and the red line is for Phase 2. The calculated maximum strain of lattice constant b is 0.242% at E-field of 0.5 eV per Å. (b) C_4O : The calculated maximum strain of lattice constant b is 0.045% at E-field of 0.5 eV per Å.



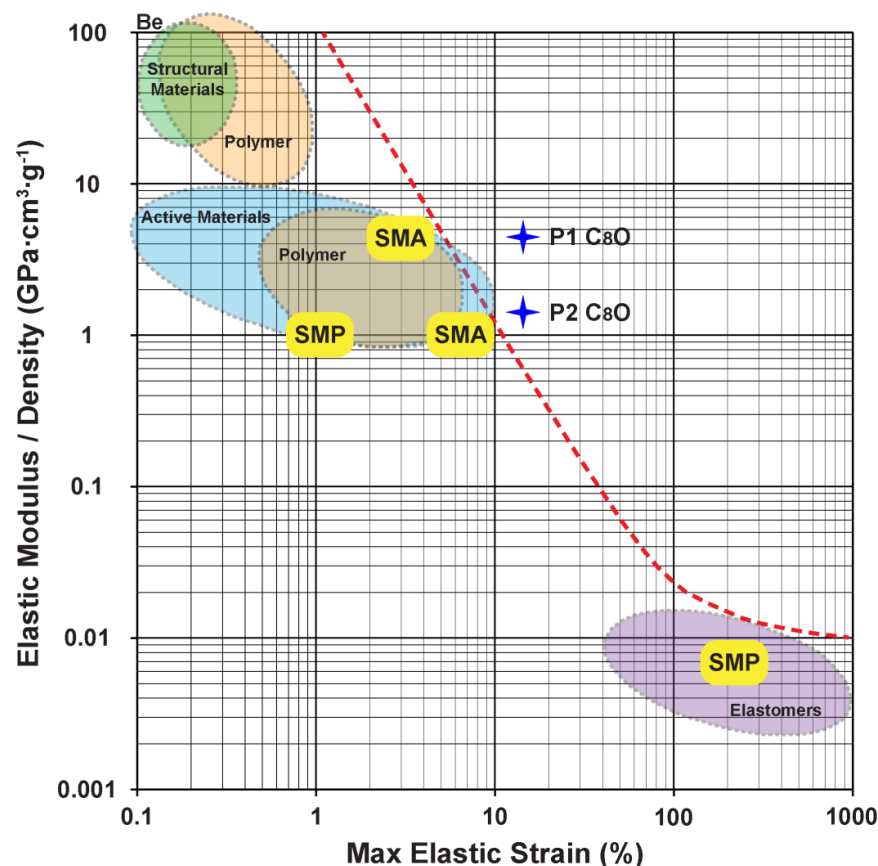
Supplementary Figure 5: Evidences of Phase 3 for C₈O and C₄O at E-field of 0.3 eV per Å (a) The DOS results of C₈O Phase 3. (b) The PDOS results of the oxygen atoms (red) and its neighbouring carbon atoms (black) of C₈O Phase 3. (c) The DOS results of C₄O Phase 3. (d) The PDOS results of the oxygen atom (red) and its neighbouring carbon atoms (black) of C₄O Phase 3. The vertical lines represent E_F . Below E_F , red and grey shaded areas indicate occupation of electrons on the p -orbitals of oxygen and carbon atoms, respectively. (e) and (f) Partial charge density surrounding the oxygen and its neighbouring carbon atoms within the energy range from -1.0 to 0.0 eV with reference to E_F , for C₈O Phase 3 and C₄O Phase 3, respectively. These results are distinctive from those of Phase 1 and Phase 2 shown in Fig. 1, Supplementary Figure 2 and Supplementary Figure 3.



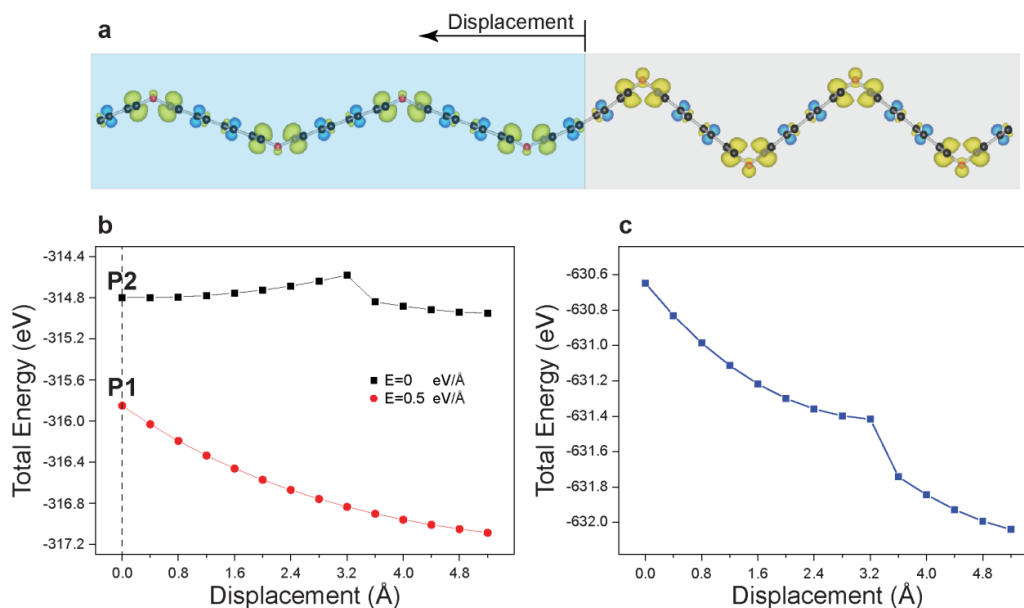
Supplementary Figure 6: Equilibrium atomistic structures of $(\text{C}_8\text{O})_4$ supercells including different types of phase mixtures. The Blue shaded region represents Phase 1 and grey shaded regions represent Phase 2. The P1:P2 ratios from (a) to (e) are 4:0, 3:1, 2:2, 1:3 and 0:4, respectively. The atomistic structures have been fully relaxed in DFT simulations. These results conclude that Phase 1 and Phase 2 can stably co-existed in a single crystal. The equilibrium constants are summarised in Supplementary Table 2.



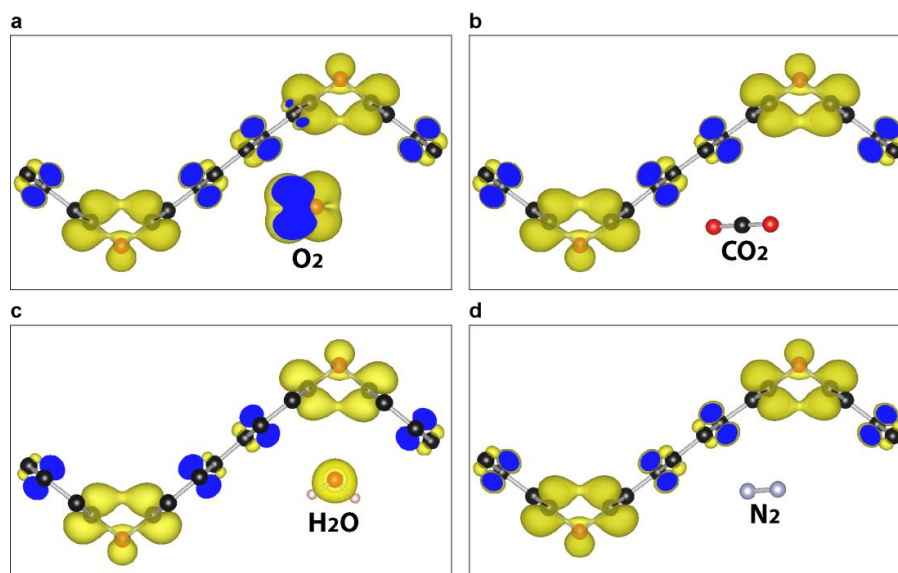
Supplementary Figure 7: Recoverable strain outputs arising from programming the percentage of Phase 2 in $(\text{C}_8\text{O})_6$ six-unit supercells. A maximum in-plane strain of -14.5% can be obtained if set the supercell with pure Phase 1 as the reference state (black line). If taken the supercell with pure Phase 2 as a reference (red line), a maximum in-plane strain of 17% can be obtained. Although the maximum recoverable strain is identical to the four-unit supercells, a larger supercell can be programmed into more temporary shapes and thus more recoverable strain outputs.



Supplementary Figure 8: A comparison of actuation performance between conventional actuation materials and two-dimensional shape memory CsO. The specific modulus (ratio of elastic modulus over density) and maximum recoverable elastic strain are two key performance parameters. The performances of common materials (including SMMs highlighted in yellow) are adapted from Supplementary Ref. 2 and 3. An actuation material with a high maximum elastic strain usually has a small specific modulus. The red dashed line denotes the upper bound for conventional actuation materials. Two major shape memory materials, shape memory alloy and shape memory polymer, are noted as SMA and SMP in this figure, respectively. Martensite-austenite phase transformation is the underlying mechanism for SMA and shape memory effect of SMP is originate from glass transition between a hard to a soft phase. Blue stars represent the Phase 1 and Phase 2 of the shape memory CsO. The calculated recoverable strain and specific modulus is 14.5% and 4.3 $\text{GPa}\cdot\text{cm}^3\cdot\text{g}^{-1}$, respectively.

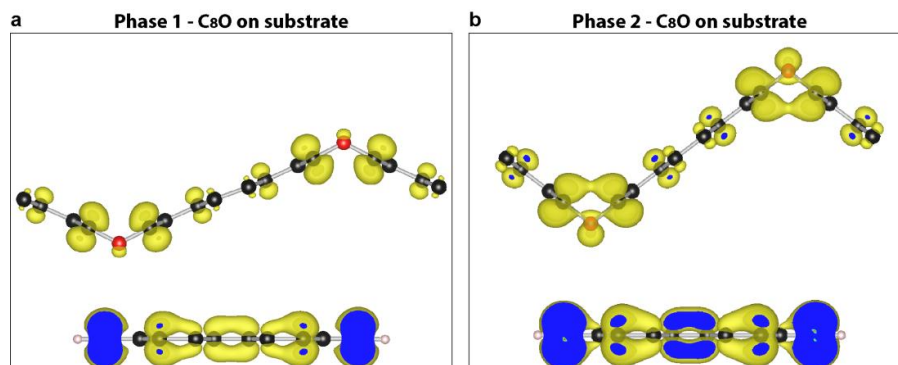


Supplementary Figure 9: Total energy vs. displacement of the mid-point for a $(C_8O)_4$ supercell with P1/P2 ratio of 2:2. (a) Atomistic structure of the $(C_8O)_4$ four-unit supercell. The mid-point is located at the interface between P1 and P2. Displacement of the mid-point is labelled. (b) Total energy of the P2 segment (right) and P1 segment (left) as a function of displacement (d) under a zero E -field and an E -field strength of 0.5 eV per Å, respectively. The dashed line represents zero displacement. (c) Total energy of the whole system as a function of d when the P1 segment (left) is being subject to a local external E -field strength of 0.5 eV per Å. This result is obtained by summarizing the two curves in (b).

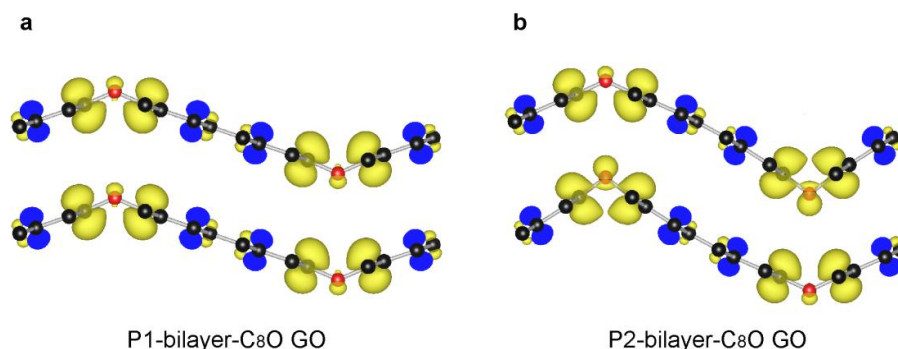


Supplementary Figure 10: Examining the influence of atmosphere. (a) – (d) Fully relaxed $P2$ C_8O supercells with oxygen, carbon dioxide, water and nitrogen molecules added. Partial charge density

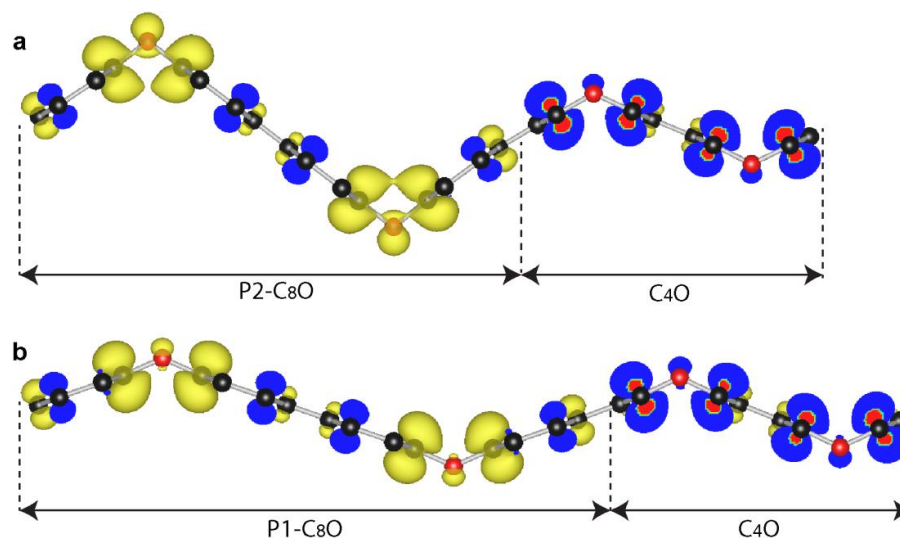
results (within the energy range from -1.0 to 0.0 eV with reference to E_F) show intact $lp-\pi$ bonds. This suggests that these molecules have nearly no effect on the phase stability of P2 C₈O.



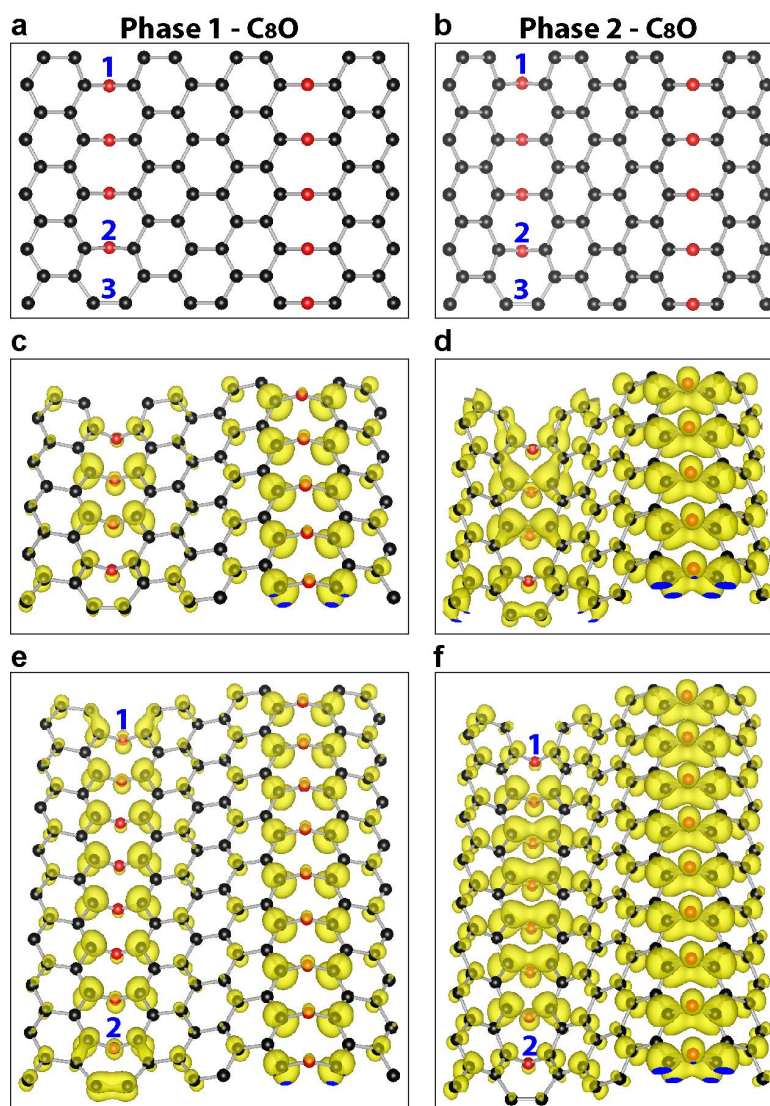
Supplementary Figure 11: Examining influences of a substrate. A layer of graphene nanoribbon was placed underneath C₈O GO crystals as a substrate in this simulation. Its edges were terminated by hydrogen atoms. Crystal structure and partial charge density (within the energy range from -1.0 to 0.0 eV with reference to E_F) of fully relaxed P1-C₈O (a) and P2-C₈O (b) with an identical graphene substrate. The calculated total energy of P1/P2-C₈O GO crystals on graphene substrate are -250.359 and -250.350 eV, respectively. Under an **E**-field of 0.3 eV per Å, the total energy values change to -250.428 and -250.626 eV, respectively. The P2-C₈O crystal on substrate becomes energetically more stable (phase transformation can be triggered even C₈O GO crystals are transformed onto a substrate). The swap of energetic order caused by **E**-field suggests the P1 to P2 phase transition should take place.



Supplementary Figure 12: Bi-stable phases of bilayer C₈O GO. Partial charge density of fully relaxed P1-bilayer- C₈O (a) and P2-bilayer- C₈O GO (b) within the energy range from -1.0 to 0.0 eV with reference to E_F . The lattice constant a is found to be 18.4 and 17.2 Å, respectively. The calculated total energy of these two stable phases are -314.977 and -314.849 eV (that is total energy difference of 128 meV). The maximum recoverable strain is about 6.5%.

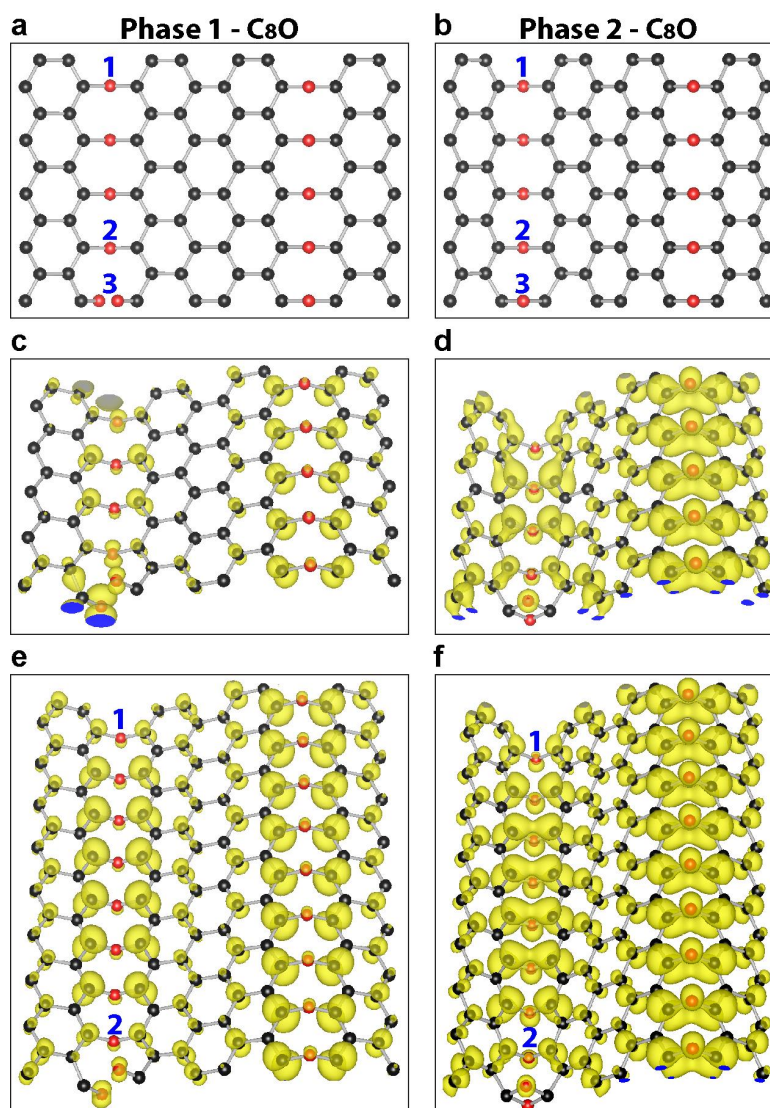


Supplementary Figure 13: Stable co-existence of C₄O and C₈O GO mixtures. Structural configurations and partial charge density of fully relaxed phase 2 (a) and phase 1 (b) of C₈O GO mixed with C₄O GO within the energy range from -1.0 to 0.0 eV with reference to E_F . The mixture ratio is 1:1 (*i.e.* P1-C₈O/C₄O and P2-C₈O/C₄O). The C-O-C angle and partial charge density results indicate that the first structure consist of one C₈O P1 unit and one C₄O P1 unit. The second structure consists of one C₈O P2 unit and one C₄O P1 unit. P1-C₈O/C₄O crystal is more stable at zero **E**-field, the calculated total energy of P1 and P2-C₈O/C₄O crystal is -241.002 and -240.867 eV, respectively. At **E**-field of 0.3 eV per Å, the corresponding total energy values are -241.044 and -241.108 and eV, which suggests that P2-C₈O/C₄O crystal becomes energetically more stable (that is phase transformation from P1 to P2) upon an appropriate external electric field.



Supplementary Figure 14: Phase 1 and phase 2 C₈O GO supercells with oxygen vacancy defects by removing one oxygen atom from the epoxy line. One oxygen atom is removed at site 3 in the P1 supercells (a) and P2 supercells (b). The perfect epoxy line length is measured by the length between site 1 and site 2. Note that the lattice constant a for perfect P1&P2-C₈O GO is 18.384 and 15.718 Å. (c) and (e) Partial charge density results of P1-C₈O 1x5 and 1x9 supercells (within the energy range from -1.0 to 0.0 eV with reference to E_F), respectively. It appears like that a sp^2 carbon-carbon bond forms at site 3 upon removal of the oxygen atom (i.e. the defect rate of 20% and 11%). The fully relaxed lattice constant a is 17.934 and 18.223 Å, respectively. (d) and (f) Partial charge density results of P2 1x5 and 1x9 supercells (within the energy range from -1.0 to 0.0 eV with reference to E_F), respectively. The signature $lp-\pi$ orbital charge density can be seen beyond the first nearest neighbour of defect. The fully relaxed lattice constant a is 15.374 and 15.510 Å, respectively. The crystal structure and partial charge density results indicate that this defect only affect the structure locally and it almost has no effects as long as concentration lower than 20% (the length of perfect epoxy line equals or

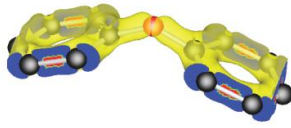
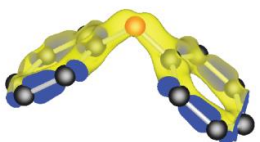
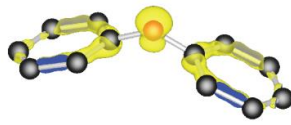
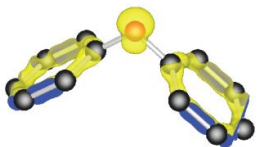
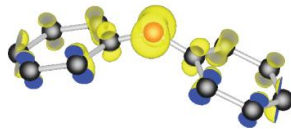
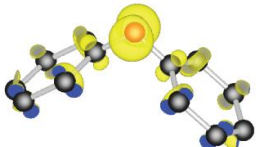
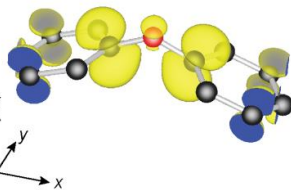
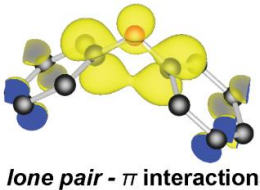
larger than 9.9 Å). The length of perfect epoxy line is measured to be 9.9 or 17.723 Å for these two different size supercells.



Supplementary Figure 15: Phase 1 and phase 2 C₈O GO with defects by introducing excess oxygen atoms on the epoxy line. The excess doping position is at site 3 for Phase 1 supercells (a) and Phase 2 supercells (b). The perfect epoxy line length is measured by the length between site 1 and site 2. Note that the lattice constant a for perfect P1&P2-C₈O GO is 18.384 and 15.718 Å. (c) & (e) Partial charge density results of P1-C₈O 1x5 and 1x9 supercells (within the energy range from -1.0 to 0.0 eV with reference to E_F), respectively. Clearly a carboxyl pair forms at site 3. The fully relaxed lattice constant a is 18.341 and 18.352 Å, respectively. (d) and (f) Partial charge density results of P2-C₈O supercells (within the energy range from -1.0 to 0.0 eV with reference to E_F), respectively. At site 3, an epoxy pair is formed instead. The fully relaxed lattice constant a is 15.654 and 15.679 Å,

respectively. The signature $lp-\pi$ orbital charge density can be seen beyond the first nearest neighbour of defect. The crystal structure and partial charge density results indicate that this defect only affect the structure locally and it almost has no effects as long as concentration lower than 20% (the length of perfect epoxy line equals or larger than 9.9 Å). The length of perfect epoxy line is measured to be 9.9 and 17.723 Å for these two different size supercells.

Supplementary Table 1: Analysis of chemical bonding in the bi-stable phases CsO. The orbital hybridization of oxygen and its neighbouring carbon atoms; Partial charge density correspond to the four energy level regions in the DOS of Phase 1 and Phase 2 (as shown in Supplementary Figure 2 (c, d)). The isosurface value is in unit of electron per bohr.

	Orbital Hybridization	Phase 1	Phase 2
1	<p>Oxygen: sp^2 for C-O bond</p> <p>Carbon: sp^2 for C-O bond sp^2 for C-C bond</p> <p>Isosurface level: 0.02</p>		
2	<p>Oxygen: sp^2 lone pair</p> <p>Carbon: sp^2 for C-C bond</p> <p>Isosurface level: 0.02</p>		
3	<p>Oxygen: p_y lone pair</p> <p>Carbon: π orbitals</p> <p>Isosurface level: 0.01</p>		
4	<p>Oxygen: sp^2 lone pair</p> <p>Carbon: π orbitals</p> <p>Isosurface level: 0.003</p>		 <p><i>lone pair - π interactions</i></p>

Supplementary Table 2: Equilibrium lattice constant a and interface energy values of $(\text{C}_8\text{O})_4$ and $(\text{C}_8\text{O})_6$ supercells with different types of Phase 1 and Phase 2 mixing. (a) Five different phase mixture cases in $(\text{C}_8\text{O})_4$ supercells. (b) Seven different phase mixture cases in $(\text{C}_8\text{O})_6$ supercells. Note that C_8O is a two-dimensional material. It is controversial to define its thickness. Thus, the interface energy value is expressed as energy per unit length.

a

4 supercells	Crystal	Interface Energy (meV per Å)	Lattice Constant a
1	$4 \times P1$		73.53
2	$3 \times P1 + 1 \times P2$	12.69	70.90
3	$2 \times P1 + 2 \times P2$	12.67	68.22
4	$1 \times P1 + 3 \times P2$	12.35	65.54
5	$4 \times P2$		62.87

b

6 supercells	Crystal	Interface Energy (meV per Å)	Lattice Constant a
1	$6 \times P1$		110.30
2	$5 \times P1 + 1 \times P2$	10.53	107.62
3	$4 \times P1 + 2 \times P2$	8.21	104.88
4	$3 \times P1 + 3 \times P2$	11.81	102.30
5	$2 \times P2 + 4 \times P2$	11.61	99.52
6	$1 \times P1 + 5 \times P2$	8.73	96.96
7	$6 \times P2$		94.31

Supplementary Note 1: Analysis of chemical bonding in the bi-stable phases C₈O.

Energy level region 1:

- Two half-filled sp^2 orbitals of oxygen atom interact with sp^2 orbitals of its neighbouring carbon atoms to form C-O σ bond.
- sp^2 orbitals of carbon atoms interact with each other to form C-C bond.

Energy level region 2:

- Isolated sp^2 lone pair of oxygen within the C-O-C plane.
- Weak sp^2 orbitals of carbon atoms interact with each other to form C-C bond.

Energy level region 3:

- Isolated p_y lone pair of oxygen perpendicular to the C-O-C plane.
- π bond of carbon atoms.

Energy level region 4:

- Phase 1 - Isolated sp^2 lone pair of oxygen and π orbitals of carbon atoms.
- Phase 2 - sp^2 lone pair of oxygen interacts with π orbitals of its neighbouring carbon atoms.

Supplementary Note 2: Evidences of Phase 3 for C₈O and C₄O at E-field of 0.3 eV per Å.

For C₈O (Supplementary Figure 5a and 5b), the DOS of P3 suggests that there is a clear band gap near the E_F , which is different from the DOS results of P1 and P2 as shown in Supplementary Figure 2a and 2b. The PDOS and partial charge density of P3 also indicates an entirely different electronic structure in comparison to P1 and P2 shown in Fig. 1d and 1e. It is worth to point out that P3 only exists under E-fields. When a sufficiently large E-field is applied to the crystal, it seems that the grey shaded π electrons peak of oxygen-bonded carbon atom in P1 shifted to the right and became empty π^* electrons above E_F . The π^* electrons of oxygen-bonded carbon atoms is then found to overlap with sp^2 lp^* of oxygen atom in the LUMO region as long as $E > 0.2$ eV per Å. Different from both P1 and P2, Supplementary Figure 5e reveals that oxygen atom of P3 has strong p_y orbital in the HOMO region.

Similarly, the DOS, PDOS and partial charge density results (Supplementary Figure 5c, 5d and 5f) also suggest the existence of P3 for C₄O upon the applied E-field.

Supplementary Note 3: Total energy vs. displacement of the mid-point of a (C₈O)₄ supercell with P1/P2 ratio of 2:2.

This section is devoted to prove feasibility of the two-way actuator design in the main text. In Fig. 6, we propose that the E-field induced contraction of P1 could generate adequate mechanical force to stretch P2 and trigger phase transition from P2 to P1 simultaneously. In DFT simulations, it is impossible to apply local E-field to one portion of a supercell. Therefore, a theoretical model is presented here.

As shown in Supplementary Figure 9, the supercell (C₈O)₄ includes P1 and P2 segments. Total energy of the whole system should be a summation of the total energy of both segments and the interface energy. By assuming an E-field strength of 0.5 eV per Å is locally applied to the P1 segment,

the energy of P1 segment as a function of its length shrinkage d (i.e., displacement of the interface) is shown in Supplementary Figure 9b, which is obtained by a separated DFT calculation of a $(\text{C}_8\text{O})_2$ supercell including only P1 under an \mathbf{E} -field strength of 0.5 eV per Å. The total energy of the P2 segment as a function of d can be obtained from Fig. 1b. Note that the result in Fig. 1b is for C_8O unit cell, whereas the P2 segment of supercell in Supplementary Figure 9 includes two C_8O units. Thus, the total energy in Fig. 1b should be doubled to obtain the results in Supplementary Figure 9b. Adding these two curves in Supplementary Figure 9b together, we should obtain total energy of the whole system as a function of d . Here the interface energy is assumed a constant and it will not change the trend of total energy vs. d relation. The energy monotonously decreases with the increase of d , indicating that the motion of mid-point should spontaneously happen. There is no energy barrier to prevent the phase transition from P2 to P1. In others words, by applying an \mathbf{E} -field locally to the P1 segment, the resultant phase transition from P1 to P2 can supply sufficient mechanical force to trigger simultaneous phase transition from P2 to P1 of the P2 segment.

Supplementary Note 4: Substrate effects on shape memory properties.

Supplementary Figure 11 shows the supercells including P1 and P2 phases of C_8O and a graphene ribbon substrate. After fully relaxation in DFT calculation, both structure are stable. The lattice constant values are 17.8 and 15.6 Å, which are very close to the P1 and P2 of C_8O . The partial charge also reveals negligible difference. The total energy of these two cases are -250.359 and -250.350 eV, respectively. A single point calculation under an external \mathbf{E} -field of 0.3 eV per Å yield their total energy values of -250.428 eV and -250.626 eV, respectively. The energetic order is swapped. This calculation confirms that phase transition between P1 and P2 of C_8O crystals with substrate can be triggered by the external electric field and thus leads to the shape memory effect.

Supplementary Note 5: Influence of defects on the epoxy lines.

To examine the influences of defects such as oxygen vacancy and redundant oxygen adatom on the structure stability, supercells of P1 and P2 C_8O with size of 1x5, 1x7, and 1x9 were created. They were fully relaxed in our DFT calculations. Supplementary Figure 14 and 15 show the relaxed crystal structure for the 1x5 and 1x9 cases. Note that the 1x7 supercells have very similar results to those of 1x9 cases. Supplementary Figure 14 and 15 (a and b) shows the top view of the 1x5 supercells, in which the position and configuration of the two types of defects are depicted. Supplementary Figure 14 shows that by removing one oxygen atom in the P2 supercell a C-C bond is formed (bond length approximately 1.43 Å), whereas the C-C bond is elongated to 1.45 Å in the P1 supercell. For the oxygen redundant case, the P2 supercell has an epoxy pair, while a carboxyl pair is formed in P1 supercell. Supplementary Figure 14 and 15 (c-f) summarises the partial charge density of P1 and P2 supercells. Clearly beyond the first nearest neighbour of the defect, the partial charge profiles of the C-O-C angles share the similar features to the perfect P1 and P2 phases. The lattice constants of the supercells, which are listed in the caption of Supplementary Figure 14 and Figure 15, are becoming closer to those of perfect P1 and P2 unit cells along x -axis with the reduction of defect concentration, the difference within 1% at defect concentration of 11%. Note that smaller supercells of 1x3 were also tested and we found the P1 phase is not stable in the oxygen vacancy case. Therefore, we can conclude that these two typical defects have limited effects on the structural stability of P1 and P2 at a defect density smaller than 20%.

Supplementary References

- 1 Dove, Martin T. Introduction to lattice dynamics, Cambridge university press. (1993).
- 2 Leng, J., Lan, X., Liu, Y. & Du, S. Shape-memory polymers and their composites: stimulus methods and applications. *Progress in Materials Science* **56**, 1077-1135 (2011).
- 3 Henry, C., McKnight, G., Enke, A., Bortolin, R. & Joshi, S. 3D FEA simulation of segmented reinforcement variable stiffness composites. *Proceedings of SPIE* **6929**, 692920X1- 69290X12 (2008).

Chapter 5

Two-way Quantum Mechanical Actuation of Graphene Oxide

5.1 Overview

Basically, two previous studies lead to the exploration of two-way quantum mechanical actuation of graphene oxide.

The first one is detailed in Chapter 4, the discovery two-dimensional shape memory graphene oxide. [17] It is necessary to emphasis again that phase transformations between two or more phases trigger the shape memory effect. C_8O GO crystal exhibits two stable phases, namely stable and meta-stable phase. Secondly, it has been reported that structural rippling effect of GO crystal can cause significant difference in actuation performance due to quantum mechanical effect (discussed in 2.4.2).

It is obvious to notice that the two stable phases of C_8O GO crystal lead to two crystal configurations with different rippling, which could result in new phenomenon in quantum mechanical actuation. Indeed, our density functional theory calculations show that a single piece of GO crystal can expand or contract depends on which phase the electron is injected into. An in-plane contraction is observed for the stable phase, however, an in-plane expansion is obtained for the meta-stable phase under the same charge condition (e.g. maximum electron injection of -0.12 e per atom). Moreover, this study also revealed that many other GO crystals exhibit bi-stable phases. Generally, a GO crystal with bi-stable phases can actuate in two-way, that is contraction and expansion, upon the same amount electron injection. Therefore, the ability of having two-way quantum mechanical actuation in a single piece of GO crystal may offer brand new opportunities in designing actuators that require easy in controlling and tuning.

5.2 Publication

The following manuscript has been submitted and currently under review with Applied Physics Letters, an AIP Publishing journal.

Monash University

Declaration for Thesis Chapter 5

Declaration by candidate

In the case of Chapter 5, the nature and extent of my contribution to the work was the following:

Nature of contribution	Extent of contribution
Conceive the idea, design the model, run simulations, results analysis, interpretation and writing.	70%

The following co-authors contributed to the work:

Name	Nature of contribution	Extent of contribution
Dr. Junkai Deng	Results analysis, writing	10%
Ganaka G. Chandrakumara	Results analysis, writing	10%
Assoc. Prof. Wenyi Yan	Project Supervision	N/A
Dr. Zhe Liu	Project Supervision	N/A

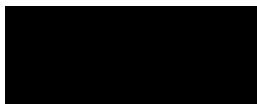
The undersigned hereby certify that the above declaration correctly reflects the nature and extent of the candidate's and co-authors' contributions to this work.

Candidate's Signature:

Candidate's Name: Zhenyue Chang

Date: 28th May 2016

Main Supervisor's Signature:



Main Supervisors's Name: Dr. Zhe Liu

Date: 28 May 2016

Two-way Actuation of Graphene Oxide arising from Quantum Mechanical Effects

Zhenyue Chang^{1,3}, Junkai Deng², Ganaka G. Chandrakumara^{1,3}, Wenyi Yan¹, and Jefferson Zhe Liu^{1,3}



¹Department of Mechanical and Aerospace Engineering, Monash University, Clayton, VIC 3800, Australia

²State Key Laboratory for Mechanical Behavior of Materials, Xi'an Jiaotong University, Xi'an 710049, China

³Monash Centre for Atomically Thin Materials, Monash University, Clayton, VIC 3800, Australia.

Abstract

Using density functional theory calculations, two stable phases were found for several graphene oxide (GO) crystals with linearly aligned epoxy groups. Upon electron injection, they exhibit two-way actuation behavior. This two-way actuation is named by the observations that one piece of monolayer GO crystal is able to expand or contract upon electron injection, namely, contraction of the stable phase, and expansion of the meta-stable phase. The obtained maximum in-plane strains are as high as 8% and -5%. Such large deformation in opposite directions obtained from a single piece GO material offers new opportunities in designing highly tunable and integrated actuators for microelectromechanical or nanoelectromechanical systems (MEMS/NEMS).

Owing to excellent down scalability, miniaturized actuators based on functional materials are now broadly implemented in various types of micro/nanomechanical systems (MEMS/NEMS).¹⁻⁵ For instance, piezoelectric materials are capable of generating linear motion with high response frequency at the nanoscopic scale.⁶ Shape memory actuators at nanoscopic scale can produce significantly larger strain output.^{7,8} Recently, graphene-based actuators arising from various actuation mechanisms have been proposed.⁹⁻¹¹ Exploration and comprehensive understanding of the underlying mechanisms become essential for designing novel high performance graphene-based actuators.

The most closely related graphene-based material is graphene oxide (GO), an atomic thin oxidized graphene, which has been realized as an excellent candidate for myriad applications¹²⁻¹⁷ thanks to its excellent electronic, and mechanical properties associated with a diverse range of possible crystal structures produced by oxygen functional groups.¹⁸⁻²¹ The epoxy and hydroxyl groups are generally accepted as the two major oxygen functional groups on the basal plane of GO.^{20,22} While hydroxyl groups dominate the surface of GO under hydrogen-rich environment,²³ recent experiments suggest it is possible to synthesize GO with only epoxy groups under some well-controlled experimental conditions.²⁴⁻²⁶ Notably, experimental observations of ordered epoxy lines on the basal plane of GO crystal (e.g. Fig.1) have triggered many interesting investigations, including the formation mechanisms of such linear epoxy groups and utilizing this mechanism in unzipping graphene.²⁷⁻³²

We have previously reported that monolayer GO crystals with ordered epoxy groups exhibit many extraordinary electromechanical properties, including quantum mechanical (QM),^{33,34} piezoelectric,³⁵ and shape memory effects.³⁶ These interesting observations enable enormous potential of using monolayer GO crystals as two-dimensional actuators. Here, we report the discovery of two-way QM actuation of GO crystals upon electron injection. Our DFT simulations show that electron injection into two stable phases of a single piece of GO crystal can induce either in-plane contraction or expansion. The calculated maximum expansion and contraction are approximately 8 and 5 %, respectively. On top of high strain outputs, the demonstration of one single GO crystal can actuate in two different ways endows the possibility of designing multifunctional GO actuators in NEMS.

GO crystals studied in this work are divided into two groups based on their structural configurations. Figure 1a shows a symmetric GO (Sym) with C/O ratio of 8, in which only one side of graphene basal plane is available to form the linear epoxy groups.^{35,37} Alternatively, an asymmetric GO (Asym) with a C/O ratio of 8 is shown in Fig. 1b when epoxy groups are located on both sides of graphene basal plane.^{29,37} Lattice constants a and b represent the unit cell length in x -axis and y -axis, where α and β measure carbon-oxygen-carbon (C-O-C) bond angle of the epoxy groups attached on the symmetric and asymmetric GO crystals. In total, six monolayer GO crystals (i.e. C₈O-Sym, C₁₂O-Sym, C₁₆O-Sym, C₈O-Asym, C₁₂O-Asym, and C₁₆O-Asym) were generated by assigning C/O ratio of 8, 12, and 16 to both configurations. Note that both configurations have been observed in experiments with different C/O ratios.^{27,29}

The Vienna ab initio simulation package (VASP v.5.3.3) was used to perform density functional (DFT) calculations in this work. Projector augmented wave method and the generalized gradient approximation were employed.^{38,39} A plane-wave cutoff energy was set as 600 eV. Monkhorst-Pack gamma-centered k -points mesh of $40 \times 10 \times 1$ and $42 \times 6 \times 1$ was adopted for C₈O-Sym and C₈O-Asym unit cell, respectively (Fig. 1). Similar k point mesh density was adopted for other

supercells. Electron charge injection was compensated using a jellium background to maintain charge neutrality in the unit cell. As periodic boundary conditions were employed in VASP, thick vacuum layers were included to minimize interlayer interactions. An interlayer spacing of 60 Å was used throughout,³³ which represents a good balance between computational accuracy and efforts. To hold this interlayer space constant, the VASP source code (constr_cell_relax.F) was modified to allow the cells to relax within the basal plane only. In all cases, the atomic positions were allowed to relax in all directions. Prior to being subjected to any electron charge injection, all structures were fully relaxed to determine their equilibrium lattice constants. GO crystals simulated in this study intrinsically have two stable (or bi-stable) phases, hence, electron charge injection needs to be applied separately to individual phase. This can be done by treating pre-converged charge neutral P1 (Fig. 2) as the starting point and gradually increase the charging electron by 0.02 -e/atom until the value reaches -0.12 -e/atom. The in-plane strain is calculated by the length change of lattice constant a in Fig. 1 as strain in the direction of lattice constant b is negligible. Then, the same charging and analysis processes can be done by treating pre-converged charge neutral P2 (Fig. 2) as the starting point.

Our recent study has revealed a GO crystal with ordered epoxy groups namely C₈O-Asym intrinsically exhibits bi-stable phases caused by a unique intra-molecular bond.³⁶ By varying the C/O ratio, Figure 2 suggests that bi-stable phases can exist in both symmetric and asymmetric GO crystals for some other C/O ratios. For the symmetric GO crystals, although the bi-stable phases are not fully-developed in Fig. 2a and 2b, the red dashed lines indicate that there is a trend to form two local minimums in both C₈O-Sym and C₁₂O-Sym. Interestingly, two local minimums in Fig. 2c denote the existence of fully-developed bi-stable phases (i.e. P1 and P2) in C₁₆O-Sym. The measured C-O-C bond angle α equals 138° for P1 and 107° for P2. For the asymmetric GO crystals, double-well energy curves clearly indicate bi-stable phases for C₈O-Asym ($\beta = 133^\circ$ for P1 and 104° for P2), C₁₂O-Asym ($\beta = 133^\circ$ for P1 and 102° for P2) and C₁₆O-Asym ($\beta = 134^\circ$ for P1 and 104° for P2). Overall, fully-developed bi-stable phases can be found intrinsically for asymmetric GO crystals with C/O ratio equals or larger than eight, while high C/O ratio (e.g. 16) leads to the fully-developed bi-stable phase in symmetric GO crystals.

Figure 3 (a-c) represents the in-plane strain as a function of electron injection for symmetric GO crystals. For GO crystals with non-fully-developed bi-stable phases (Fig. 3 (a, b)), both C₈O-Sym and C₁₂O-Sym contract upon electron injection (black lines). The obtained maximum strain outputs are -0.7 and -0.8%, respectively. The trend agrees well with previous study on unzipped C₄O-Sym,³³ and the amount of contraction is enhanced by more than three times under the same amount of electron injection. The significant enhancement of contraction is directly caused by the increase in structural rippling as the C:O ratios become larger in C₈O-Sym and C₁₂O-Sym.³³ Intriguingly, the strain-charge relationship shown in Fig. 3c suggests that P1 and P2 of C₁₆O-Sym responses completely different upon electron injection. P1 phase contracts to a maximum value of 0.9% at 0.12 -e/atom. Injection of electrons into to P2 leads to a significant expansion (red line) of 4.4% at 0.12 -e/atom. It has been reported that pristine graphene expands about 0.2% upon electron injection,⁴⁰ and the expansion upon electron injection for GO with ordered epoxy groups is only about 0.4%.³³ It is important to notice that the expansion performance of P2 of C₁₆O-Sym is improved by more than ten times.

Given that all Asym-GO crystals investigated in this study exhibit bi-stable phases with significant rippling differences, it is reasonable to expect that the unique QM actuation observed in

C₁₆O-Sym could also be obtained in the Asym-GO crystals. Figure 3 (d-f) shows the strain-charge curves upon electron injection for C₈O, C₁₂O, and C₁₆O-Asym. Indeed, black lines clearly illustrate the contraction of P1, and red lines confirm expansion of P2 for all asymmetric crystals. Depending on the choice of initial phase (i.e. P1 or P2), one single piece bi-stable GO crystal is able to produce a significant amount of contraction and expansion without making any adjustment to the external stimuli. This unusual but fascinating phenomenon is defined as electron injection-induced two-way QM actuation. Particularly, a huge amount expansion close to 8% can be obtained by either C₈O-Asym or C₁₂O-Asym, while maintaining the capability of contracting more than 5% without alternating the external stimulus.

To reveal the underlying mechanism of such unique two-way actuation, an in-depth structural and electronic analysis of bi-stable GO crystal upon electron injection is essential. Taking C₈O-Asym upon electron injection as an example, projected density of states (DOS) of P1 and P2 in the vicinity of Fermi level (E_F) are plotted in Fig. 4. The major DOS difference between these two stable phases is p -electrons DOS of the oxygen-bonded carbon atoms (grey shaded area) inherently interact with p -electrons DOS of the oxygen atom (red shaded area) below E_F as shown in Fig. 4b, which directly leads to the existence of P2.³⁶ As the electron injection commenced, E_F of the crystal shifts to the right (i.e. from the blue dashed line to the solid black line at $E-E_F = 0$) gradually. In other words, excess electrons injected into P1 start to occupy the unfilled lone pair (lp) orbital of the oxygen atom and π orbitals of oxygen-bonded carbon atoms as shown in Fig. 4a. This process tends to promote the intra-molecular $lp-\pi$ bond. Inset of Fig. 4a, partial charge density surrounding the oxygen and its neighboring carbon atoms (within the energy range from virtual E_F to the true E_F), evidentially confirms the formation of such intra-molecular bond. Given that this unique bond serves to reduce the C-O-C bond angle β significantly as indicated by the arrow in Fig. 4a inset,³⁶ the crystal becomes more ripple and thus results in the in-plane contraction of P1 upon electron injection.³³ However, for P2, only π orbitals of carbon atoms are available for the injected electrons. Inset of Fig. 4b visually confirms the enrichment of π orbitals upon electron injection, especially between the two oxygen-bonded carbon atoms. The enhanced π orbitals between the two carbon atoms can induce a $\pi-\pi$ repulsive force,³³ which leads to the increase of the C-O-C bond angle β as indicated by the arrow in Fig. 4b inset. Consequently, the obtained in-plane expansion of P2 as a result of increased angle β .

In summary, we have demonstrated electron injection-induced two-way QM actuation of the GO crystals with linearly aligned epoxy groups. Intrinsic bi-stable phases are found in these GO with different C/O ratios. These two stable phases can respond oppositely (i.e. contraction and expansion) upon electron injection. The obtained maximum expansion and contraction at 0.12 e-/atom are approximately 8% and -5%, respectively. Through an in-depth electronic analysis, we find that excess electrons into P1 promote the intra-molecular $lp-\pi$ bond, leading to the decrease of C-O-C bond angle β and thus in-plane contraction of P1. On the contrary, a repulsive force between two oxygen-bonded carbon atoms arising from the enhancement of $\pi-\pi$ interaction in P2 tends to flatten the crystal. Thus, an in-plane expansion is achieved. The disclosure of injection-induced two-way QM actuation may offer great potential of utilizing bi-stable GO crystals for easily tunable, fast responding and highly integrated two-way actuators in NEMS.

References

- 1 Jo, C., Pugal, D., Oh, I.-K., Kim, K. J. & Asaka, K. Recent advances in ionic polymer–metal composite actuators and their modeling and applications. *Progress in Polymer Science* **38**, 1037-1066 (2013).
- 2 Devendran, C., Gralinski, I. & Neild, A. Separation of particles using acoustic streaming and radiation forces in an open microfluidic channel. *Microfluidics and Nanofluidics* **17**, 879-890 (2014).
- 3 Asaka, K. & Okuzaki, H. *Soft Actuators: Materials, Modeling, Applications, and Future Perspectives*. (Springer, 2014).
- 4 Ionov, L. Actively-moving materials based on stimuli-responsive polymers. *Journal of Materials Chemistry* **20**, 3382-3390 (2010).
- 5 Zhao, Q., Qi, H. J. & Xie, T. Recent progress in shape memory polymer: New behavior, enabling materials, and mechanistic understanding. *Progress in Polymer Science* **49**, 79-120 (2015).
- 6 Zhang, J., Wang, C. & Bowen, C. Piezoelectric effects and electromechanical theories at the nanoscale. *Nanoscale*, doi:10.1039/C4NR03756A (2014).
- 7 Jani, J. M., Leary, M., Subic, A. & Gibson, M. A. A review of shape memory alloy research, applications and opportunities. *Materials & Design* **56**, 1078-1113 (2014).
- 8 Hager, M. D., Bode, S., Weber, C. & Schubert, U. S. Shape memory polymers: Past, present and future developments. *Progress in Polymer Science* **49**, 3-33 (2015).
- 9 Park, S., An, J., Suk, J. W. & Ruoff, R. S. Graphene - Based Actuators. *Small* **6**, 210-212 (2010).
- 10 Zhu, S.-E. *et al.* Graphene-based bimorph microactuators. *Nano letters* **11**, 977-981 (2011).
- 11 Xie, X. *et al.* An asymmetrically surface-modified graphene film electrochemical actuator. *ACS nano* **4**, 6050-6054 (2010).
- 12 Novoselov, K. S. *et al.* Electric field effect in atomically thin carbon films. *science* **306**, 666-669 (2004).
- 13 Raccichini, R., Varzi, A., Passerini, S. & Scrosati, B. The role of graphene for electrochemical energy storage. *Nature materials* **14**, 271-279 (2015).
- 14 Hu, Y. *et al.* Zeolitic Imidazolate Framework/Graphene Oxide Hybrid Nanosheets as Seeds for the Growth of Ultrathin Molecular Sieving Membranes. *Angewandte Chemie International Edition* doi:10.1002/anie.201509213 (2015).
- 15 Trung, T. Q. *et al.* A Flexible Reduced Graphene Oxide Field - Effect Transistor for Ultrasensitive Strain Sensing. *Advanced Functional Materials* **24**, 117-124 (2014).
- 16 Borini, S. *et al.* Ultrafast graphene oxide humidity sensors. *ACS nano* **7**, 11166-11173 (2013).
- 17 Chandrakumara, G. G. *et al.* Tuning the oxygen functional groups in reduced graphene oxide papers to enhance the electromechanical actuation. *RSC Advances* **5**, 68052-68060 (2015).
- 18 Suk, J. W., Piner, R. D., An, J. & Ruoff, R. S. Mechanical properties of monolayer graphene oxide. *ACS nano* **4**, 6557-6564 (2010).
- 19 Zhu, Y. *et al.* Graphene and graphene oxide: synthesis, properties, and applications. *Advanced materials* **22**, 3906-3924 (2010).
- 20 Casabianca, L. B. *et al.* NMR-based structural modeling of graphite oxide using multidimensional ¹³C solid-state NMR and ab initio chemical shift calculations. *Journal of the American Chemical Society* **132**, 5672-5676 (2010).
- 21 Zhao, J., Liu, L. & Li, F. *Graphene oxide: Physics and applications*. (Springer, 2015).
- 22 Cai, W. *et al.* Synthesis and solid-state NMR structural characterization of ¹³C-labeled graphite oxide. *Science* **321**, 1815-1817 (2008).
- 23 Kim, S. *et al.* Room-temperature metastability of multilayer graphene oxide films. *Nature materials* **11**, 544-549 (2012).
- 24 Hossain, M. Z. *et al.* Chemically homogeneous and thermally reversible oxidation of epitaxial graphene. *Nature chemistry* **4**, 305-309 (2012).
- 25 Mattson, E. C. *et al.* Evidence of nanocrystalline semiconducting graphene monoxide during thermal reduction of graphene oxide in vacuum. *ACS nano* **5**, 9710-9717 (2011).
- 26 Huang, B., Xiang, H., Xu, Q. & Wei, S.-H. Overcoming the phase inhomogeneity in chemically functionalized graphene: the case of graphene oxides. *Physical review letters* **110**, 085501 (2013).
- 27 Pandey, D., Reifengerger, R. & Piner, R. Scanning probe microscopy study of exfoliated oxidized graphene sheets. *Surface Science* **602**, 1607-1613 (2008).

- 28 Li, J.-L. *et al.* Oxygen-driven unzipping of graphitic materials. *Physical review letters* **96**, 176101 (2006).
- 29 Fujii, S. & Enoki, T. Cutting of oxidized graphene into nanosized pieces. *Journal of the American Chemical Society* **132**, 10034-10041 (2010).
- 30 Li, Z., Zhang, W., Luo, Y., Yang, J. & Hou, J. G. How graphene is cut upon oxidation? *Journal of the American Chemical Society* **131**, 6320-6321 (2009).
- 31 Ma, L., Wang, J. & Ding, F. Strain - Induced Orientation - Selective Cutting of Graphene into Graphene Nanoribbons on Oxidation. *Angewandte Chemie International Edition* **51**, 1161-1164 (2012).
- 32 Sun, T. & Fabris, S. Mechanisms for oxidative unzipping and cutting of graphene. *Nano letters* **12**, 17-21 (2011).
- 33 Rogers, G. W. & Liu, J. Z. High-performance graphene oxide electromechanical actuators. *Journal of the American Chemical Society* **134**, 1250-1255 (2011).
- 34 Rogers, G. W. & Liu, J. Z. Monolayer graphene oxide as a building block for artificial muscles. *Applied Physics Letters* **102**, 021903 (2013).
- 35 Chang, Z., Yan, W., Shang, J. & Liu, J. Z. Piezoelectric properties of graphene oxide: A first-principles computational study. *Applied Physics Letters* **105**, 023103 (2014).
- 36 Chang, Z., Deng, J., Chandrakumara, G. G., Yan, W., & Liu, J. Z. Two-Dimensional Shape Memory Graphene Oxide. *In Press* (2016).
- 37 Xu, Z. & Xue, K. Engineering graphene by oxidation: a first-principles study. *Nanotechnology* **21**, 045704 (2010).
- 38 Kresse, G. & Furthmüller, J. Efficient iterative schemes for ab initio total-energy calculations using a plane-wave basis set. *Physical Review B* **54**, 11169 (1996).
- 39 Kresse, G. & Joubert, D. From ultrasoft pseudopotentials to the projector augmented-wave method. *Physical Review B* **59**, 1758 (1999).
- 40 Rogers, G. W. & Liu, J. Z. Graphene actuators: quantum-mechanical and electrostatic double-layer effects. *Journal of the American Chemical Society* **133**, 10858-10863 (2011).

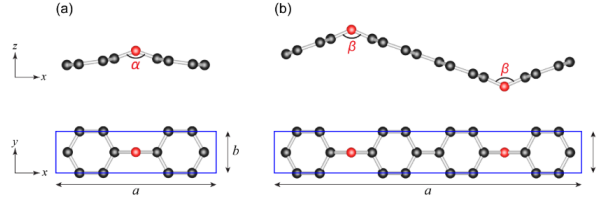


Figure 1: Crystal structure of Sym-C₈O (a) and Asym-C₈O with a and b as the lattice constant in x and y -axis (rectangular supercells are used). Black and red spheres represent the carbon (C) and oxygen (O) atoms, respectively. Angle α and β measures the bond angle of oxygen atom and its two neighboring carbon atoms for Sym-C₈O and Asym-C₈O, respectively.

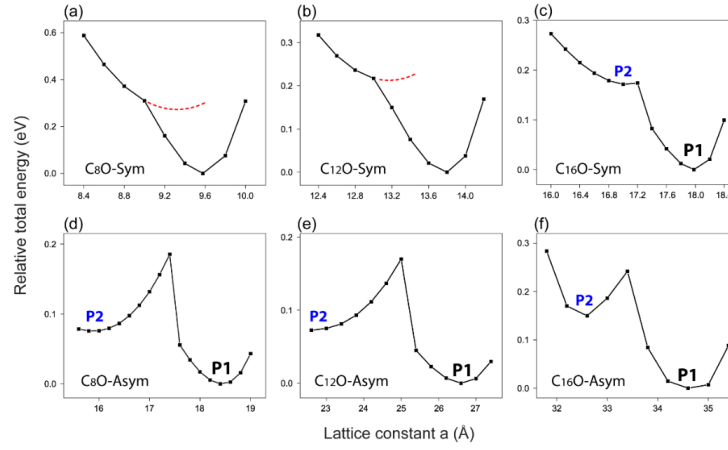


Figure 2: The relative total energy as a function of lattice constant a for Sym-C₈O (a), Sym-C₁₂O (b), Sym-C₁₆O (c), Asym-C₈O (d), Asym-C₁₂O (e), and Asym-C₁₆O (f) monolayer GO crystal. The two local minimum points represent the two stable phases: P1 and P2.

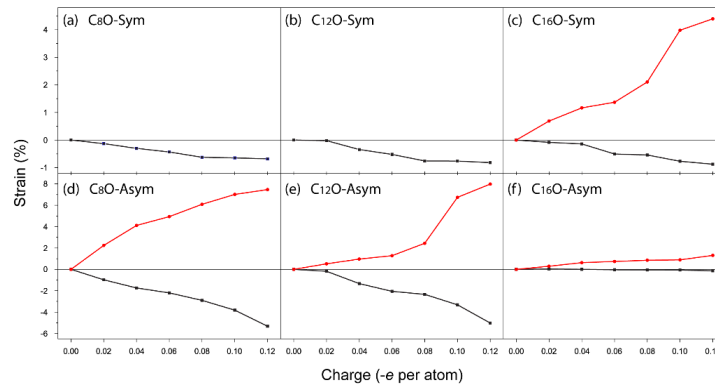


Figure 3: In-plane strain as a function of electron injection for Sym-C₈O (a), Sym-C₁₂O (b), Sym-C₁₆O (c), Asym-C₈O (d), Asym-C₁₂O (e), and Asym-C₁₆O (f) monolayer GO crystal. The red and black lines indicate expansion and contraction of the P2 and P1, respectively.

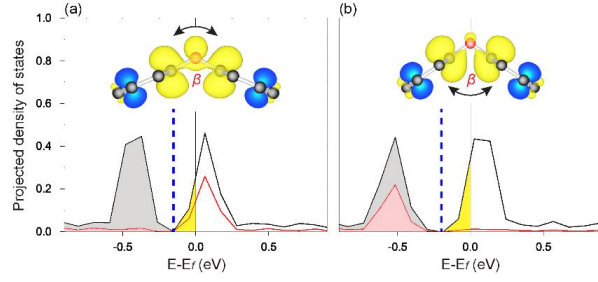


Figure 4: Projection density of state (PDOS) results for P1 (a) and P2 (b) of Asym-C₈O upon electron injection of -0.12 e/atom. The black curves represent *p*-electrons DOS of the carbon atoms and the red curves represent *p*-electrons DOS of the oxygen atom. The solid vertical lines represent the E_F . Below E_F , red and grey shaded areas indicate occupation of electrons on the *p*-orbitals of oxygen and carbon atoms, respectively. The yellow shaded areas represent excess electrons injected into the system and the vertical blue dashed line drawn here is used as an indicator for E_F of both P1 and P2 in the charge neutral state. Inset of (a) and (b): partial charge density surrounding the oxygen and its neighboring carbon atoms for both P1 and P2.

Chapter 6

Conclusions and Future Work

This chapter will summarise the contribution of the work discussed throughout this thesis. Following this, ongoing work and recommendation on future work will be presented.

6.1 Contributions

The fundamental knowledge gap in utilising GO crystal as a electromechanical nano- or two-dimensional actuator is apparent. Therefore, the focus of the work carried out within this thesis was to gain a comprehensive understanding of three common electromechanical properties of GO with ordered epoxy groups. Throughout this thesis, piezoelectric effect of GO was revealed, which enables GO as one of the thinnest piezoelectric material that could potentially be employed for two-dimensional actuation. Additionally, shape memory effect is discovered in GO crystal along with the programmability feature. For the first time ever, monolayer GO with ordered epoxy groups is discovered as a two-dimensional shape memory material. Lastly, the great potential of quantum mechanical effect was further extended by observing electron injection-induced two-way quantum mechanical actuation of GO. The following will discuss the specific contributions that stem from each of the chapters included in this thesis.

Chapter 3

In this chapter, piezoelectricity was revealed in GO with ordered epoxy groups, namely clamped and unzipped. By varying the percentage of oxygen doping, the obtained maximum in-plane was measured to be 0.12 % at the electric field strength of 0.5 eV\AA^{-1} . The calculated piezoelectric strain coefficient d_{31} of 0.24 pmV^{-1} is comparable with some bulk and most graphene-based piezoelectric materials. A detail electronic and structural analysis was carried out to fully understand the strain deformation of the piezoelectric GO crystal at atomic scale, which could be highly desirable for designing and controlling two-dimensional actuators with extremely fast responses.

Chapter 4

The discovery of first atomically thin shape memory material, namely two-dimensional shape memory GO, was demonstrated in this chapter. Phase transformation (thus the shape memory effect) between two intrinsic phases of the GO is triggered by a combination of electric field and mechanical force. A unique intra-molecular bond was classified as atomic switch, which is responsible for controlling the shape memory effect upon external stimuli. The recoverable strain was calculated to be 14.5 %, which is significantly larger than that of for conventional shape memory alloys. Owing to the excellent mechanical properties of monolayer GO, shape memory GO may overcome the low power density output of commonly used shape memory polymers. Indeed, the overall actuation performance of shape memory GO is beyond the limit of commonly implemented materials. Finally, a prototype electric field stimulated two-way nano-actuator based on the shape memory GO was proposed to show its potential in developing advanced two-dimensional electromechanical devices.

Chapter 5

Here, the great potential of quantum mechanical actuation was further extended as the exploration of electron injection-induced two-way quantum mechanical actuation of GO. A throughout search of GO crystals was conducted first to find bi-stable GO with ordered epoxy groups. By applying electron injection only, the stable phase of GO contracts and expansion was observed for meta-stable phase of the same GO. High actuation strain outputs were achieved, that is a maximum contraction and expansion of approximately 5 and 8 %, respectively. The fact that one single piece of bi-stable GO crystal is able to contract and expand upon the same external stimuli may greatly simplify the integration complexity of actuators system in the future, and could potentially offer opportunities in designing high tunable and multi-functional two-dimensional actuators in NEMS.

6.2 Ongoing and Future Work

As outlined in this thesis, investigations into electromechanical properties of GO has resulted in several contributions. However, the need for further development into both GO and other atomically thin materials is evidently necessary. This section will briefly discuss some ongoing and potential avenues for future research.

In Chapter 4, two-dimensional shape memory GO was discovered and the concept of atomic switch was adopted to control the phase transformation between the intrinsic phases. Many other atomically thin materials with functional groups exhibit bi-stable or multiple phases inherently, which can be potentially used as two-dimensional shape memory materials. Indeed, one of our recent work has successfully demonstrated shape memory effect in Li doped phosphorene upon the applied electric field. [18] As discussed in 2.3, the first necessary step of exploring other two-dimensional or atomically thin materials with shape memory effect is to determine two or more intrinsic stable phases. Then, a right

external stimulus is required to triggered phase transformations so that shape memory effect or multi-shape memory effect can be identified. It is crucial to distinguish shape change effect from shape memory effect based on the energy barrier between phases. In addition, one method to demonstrate the programmability of an atomically thin material is to demonstrate the co-existence of multi-phases in one crystal. Furthermore, only electric field is employed in this thesis to trigger the phase transformation, shape memory effect of atomically thin materials could be simulated by other external stimulus. Therefore, the discovery of shape memory graphene oxide has provided the basic knowledge for searching and utilising two-dimensional shape memory materials. Many additional works can be done in this direction to offer brand new opportunities in shape memory based nano-electromechanical devices.

In Chapter 5, electron injection-induced two-way quantum mechanical actuation of GO was explored. Even only consider one single piece of GO crystal, this work suggested that the performance of quantum mechanical actuation is highly depend on the structural difference caused by the original phase status of a crystal. The actuation performances (either expansion or contraction) can be selectively programmed to suit various actuation requirements. This concept would greatly reduce the complexity of electromechanical devices at extremely small scales. Since other bi-stable two-dimensional materials have been, and it is expected that more will be revealed, it is thus necessary to explore their quantum mechanical actuation performance because new phenomenons, for example, multi-quantum mechanical actuations, could be explored in the nearly future.

"The process of scientific discovery is, in effect, a continual flight from wonder"

Albert Einstein

Bibliography

- [1] Mikhail I Katsnelson. Graphene: carbon in two dimensions. *Materials Today*, 10(1):20–27, 2007.
- [2] Shintaro Fujii and Toshiaki Enoki. Cutting of oxidized graphene into nanosized pieces. *Journal of the American Chemical Society*, 132(29):10034–10041, 2010.
- [3] Tao Sun and Stefano Fabris. Mechanisms for oxidative unzipping and cutting of graphene. *Nano Letters*, 12(1):17–21, 2011.
- [4] Liang Ma, Jinlan Wang, and Feng Ding. Strain-induced orientation-selective cutting of graphene into graphene nanoribbons on oxidation. *Angewandte Chemie International Edition*, 51(5):1161–1164, 2012.
- [5] Md Zakir Hossain, James E Johns, Kirk H Bevan, Hunter J Karmel, Yu Teng Liang, Shinya Yoshimoto, Kozo Mukai, Tatanori Koitaya, Jun Yoshinobu, Maki Kawai, et al. Chemically homogeneous and thermally reversible oxidation of epitaxial graphene. *Nature Chemistry*, 4(4):305–309, 2012.
- [6] Swapnil Chandratre and Pradeep Sharma. Coaxing graphene to be piezoelectric. *Applied Physics Letters*, 100(2):023114, 2012.
- [7] Mitchell T Ong and Evan J Reed. Engineered piezoelectricity in graphene. *ACS Nano*, 6(2):1387–1394, 2012.
- [8] Jaronie Mohd Jani, Martin Leary, Aleksandar Subic, and Mark A Gibson. A review of shape memory alloy research, applications and opportunities. *Materials & Design*, 56:1078–1113, 2014.
- [9] CP Henry, GP McKnight, A Enke, R Bortolin, and S Joshi. 3d fea simulation of segmented reinforcement variable stiffness composites. In *The 15th International Symposium on: Smart Structures and Materials & Nondestructive Evaluation and Health Monitoring*, pages 69290X–69290X. International Society for Optics and Photonics, 2008.
- [10] Ray H Baughman, Changxing Cui, Anvar A Zakhidov, Zafar Iqbal, Joseph N Barisci, Geoff M Spinks, Gordon G Wallace, Alberto Mazzoldi, Danilo De Rossi, Andrew G Rinzler, et al. Carbon nanotube actuators. *Science*, 284(5418):1340–1344, 1999.

- [11] J Scott Bunch, Arend M Van Der Zande, Scott S Verbridge, Ian W Frank, David M Tanenbaum, Jeevak M Parpia, Harold G Craighead, and Paul L McEuen. Electromechanical resonators from graphene sheets. *Science*, 315(5811):490–493, 2007.
- [12] Xuejun Xie, Liangti Qu, Ce Zhou, Yan Li, Jia Zhu, Hua Bai, Gaoquan Shi, and Liming Dai. An asymmetrically surface-modified graphene film electrochemical actuator. *ACS Nano*, 4(10):6050–6054, 2010.
- [13] Shou-En Zhu, Roxana Shabani, Jonghyun Rho, Youngsoo Kim, Byung Hee Hong, Jong-Hyun Ahn, and Hyoung J Cho. Graphene-based bimorph microactuators. *Nano Letters*, 11(3):977–981, 2011.
- [14] Geoffrey W Rogers and Jefferson Z Liu. Graphene actuators: quantum-mechanical and electrostatic double-layer effects. *Journal of the American Chemical Society*, 133(28):10858–10863, 2011.
- [15] Geoffrey W Rogers and Jefferson Z Liu. High-performance graphene oxide electromechanical actuators. *Journal of the American Chemical Society*, 134(2):1250–1255, 2011.
- [16] Zhenyue Chang, Wenyi Yan, Jin Shang, and Jefferson Zhe Liu. Piezoelectric properties of graphene oxide: A first-principles computational study. *Applied Physics Letters*, 105(2):023103, 2014.
- [17] Zhenyue Chang, Junkai Deng, Ganaka Gilshan Chandrakumara, Wenyi Yan, and Jefferson Zhe Liu. Two-dimensional shape memory graphene oxide. *Nature Communications*, In Press (DOI: 10.1038/ncomms11972) 2016.
- [18] Junkai Deng, Zhenyue Chang, Tong Zhao, Xiangdong Ding, Jun Sun, and Jefferson Zhe Liu. Electric field induced reversible phase transition in li doped phosphorene: Shape memory effect and superelasticity. *Journal of the American Chemical Society*, 138(14):4772–4778, 2016.
- [19] Richard P Feynman. There’s plenty of room at the bottom. *Engineering and Science*, 23(5):22–36, 1960.
- [20] Amitabha Ghosh and Burkhard Corves. *Introduction to Micromechanisms and Microactuators*. Springer, 2015.
- [21] Choonghee Jo, David Pugal, Il-Kwon Oh, Kwang J Kim, and Kinji Asaka. Recent advances in ionic polymer–metal composite actuators and their modeling and applications. *Progress in Polymer Science*, 38(7):1037–1066, 2013.
- [22] Owen Y Loh and Horacio D Espinosa. Nanoelectromechanical contact switches. *Nature Nanotechnology*, 7(5):283–295, 2012.
- [23] Robert Osiander, M Ann Garrison Darrin, and John L Champion. *MEMS and microstructures in aerospace applications*. CRC press, 2005.

- [24] Hartmut Janocha. *Actuators: basics and applications*. Springer Science & Business Media, 2013.
- [25] Jun Lu, Sang-Gyun Kim, Sunwoo Lee, and Il-Kwon Oh. A biomimetic actuator based on an ionic networking membrane of poly (styrene-alt-maleimide)-incorporated poly (vinylidene fluoride). *Advanced Functional Materials*, 18(8):1290–1298, 2008.
- [26] Yi Huang, Jiajie Liang, and Yongsheng Chen. The application of graphene based materials for actuators. *Journal of Materials Chemistry*, 22(9):3671–3679, 2012.
- [27] Tissaphern Mirfakhrai, John DW Madden, and Ray H Baughman. Polymer artificial muscles. *Materials Today*, 10(4):30–38, 2007.
- [28] Adelaide Nespoli, Stefano Besseghini, Simone Pittaccio, Elena Villa, and Stefano Viscuso. The high potential of shape memory alloys in developing miniature mechanical devices: A review on shape memory alloy mini-actuators. *Sensors and Actuators A: Physical*, 158(1):149–160, 2010.
- [29] R Lefevre, MF Goffman, V Derycke, C Miko, L Forró, JP Bourgoin, and P Hesto. Scaling law in carbon nanotube electromechanical devices. *Physical Review Letters*, 95(18):185504, 2005.
- [30] Chang Liu and Yoseph Bar-Cohen. Scaling laws of microactuators and potential applications of electroactive polymers in mems. In *1999 Symposium on Smart Structures and Materials*, pages 345–354. International Society for Optics and Photonics, 1999.
- [31] Orphee Cugat, Jerome Delamare, and Gilbert Reyne. Magnetic micro-actuators and systems (magmas). *Magnetics, IEEE Transactions on*, 39(6):3607–3612, 2003.
- [32] Manfred Kohl. *Shape memory microactuators*. Springer Science & Business Media, 2013.
- [33] Holger Conrad, Harald Schenk, Bert Kaiser, Sergiu Langa, Matthieu Gaudet, Klaus Schimmanz, Michael Stolz, and Miriam Lenz. A small-gap electrostatic micro-actuator for large deflections. *Nature Communications*, 6, 2015.
- [34] Marc J Madou. *Manufacturing techniques for microfabrication and nanotechnology*, volume 2. CRC Press, 2011.
- [35] Kaushik Bhattacharya and Richard D James. The material is the machine. *Science*, 307(5706):53, 2005.
- [36] Keith Worden, William A Bullough, and Jonathan Haywood. *Smart technologies*. World Scientific, 2003.
- [37] Kenji Uchino. *Advanced piezoelectric materials: Science and technology*. Elsevier, 2010.

- [38] Massood Tabib-Azar. *Microactuators: electrical, magnetic, thermal, optical, mechanical, chemical & smart structures*, volume 4. Springer Science & Business Media, 2013.
- [39] Cícero R de Lima, Sandro L Vatanabe, Andres Choi, Paulo Henrique Nakasone, Rogério Felipe Pires, and Emílio Carlos Nelli Silva. A biomimetic piezoelectric pump: Computational and experimental characterization. *Sensors and Actuators A: Physical*, 152(1):110–118, 2009.
- [40] Kazuhiro Otsuka and Clarence Marvin Wayman. *Shape memory materials*. Cambridge University Press, 1999.
- [41] Xuelian Wu, Wei Min Huang, Yong Zhao, Zheng Ding, Cheng Tang, and Jiliang Zhang. Mechanisms of the shape memory effect in polymeric materials. *Polymers*, 5(4):1169–1202, 2013.
- [42] WM Huang, Z Ding, CC Wang, J Wei, Y Zhao, and H Purnawali. Shape memory materials. *Materials Today*, 13(7):54–61, 2010.
- [43] Qian Zhao, H Jerry Qi, and Tao Xie. Recent progress in shape memory polymer: New behavior, enabling materials, and mechanistic understanding. *Progress in Polymer Science*, 49:79–120, 2015.
- [44] Yoseph Bar-Cohen. Electroactive polymers as artificial muscles-capabilities, potentials and challenges. *Handbook on Biomimetics*, 8, 2000.
- [45] Binayak Bhandari, Gil-Yong Lee, and Sung-Hoon Ahn. A review on ipmc material as actuators and sensors: fabrications, characteristics and applications. *International Journal of Precision Engineering and Manufacturing*, 13(1):141–163, 2012.
- [46] Yong-Lai Zhang, Qi-Dai Chen, Zhi Jin, Eunkyong Kim, and Hong-Bo Sun. Biomimetic graphene films and their properties. *Nanoscale*, 4(16):4858–4869, 2012.
- [47] Geoffrey W Rogers and Jefferson Z Liu. Monolayer graphene oxide as a building block for artificial muscles. *Applied Physics Letters*, 102(2):021903, 2013.
- [48] Kostya S Novoselov, Andre K Geim, SV Morozov, D Jiang, Y_ Zhang, SV Dubonos, IV Grigorieva, and AA Firsov. Electric field effect in atomically thin carbon films. *Science*, 306(5696):666–669, 2004.
- [49] Changgu Lee, Xiaoding Wei, Jeffrey W Kysar, and James Hone. Measurement of the elastic properties and intrinsic strength of monolayer graphene. *Science*, 321(5887):385–388, 2008.
- [50] Alexander A Balandin, Suchismita Ghosh, Wenzhong Bao, Irene Calizo, Desalegne Teweldebrhan, Feng Miao, and Chun Ning Lau. Superior thermal conductivity of single-layer graphene. *Nano Letters*, 8(3):902–907, 2008.

- [51] Philip Richard Wallace. The band theory of graphite. *Physical Review*, 71(9):622, 1947.
- [52] Gordon W Semenoff. Condensed-matter simulation of a three-dimensional anomaly. *Physical Review Letters*, 53(26):2449, 1984.
- [53] F Duncan M Haldane. Model for a quantum hall effect without landau levels: Condensed-matter realization of the " parity anomaly". *Physical Review Letters*, 61(18):2015, 1988.
- [54] Andre Konstantin Geim. Graphene: status and prospects. *Science*, 324(5934):1530–1534, 2009.
- [55] Kirill I Bolotin, KJ Sikes, Zd Jiang, M Klima, G Fudenberg, J Hone, Ph Kim, and HL Stormer. Ultrahigh electron mobility in suspended graphene. *Solid State Communications*, 146(9):351–355, 2008.
- [56] Frank Schwierz. Graphene transistors. *Nature Nanotechnology*, 5(7):487–496, 2010.
- [57] Eduardo V Castro, KS Novoselov, SV Morozov, NMR Peres, JMB Lopes Dos Santos, Johan Nilsson, F Guinea, AK Geim, and AH Castro Neto. Biased bilayer graphene: semiconductor with a gap tunable by the electric field effect. *Physical Review Letters*, 99(21):216802, 2007.
- [58] Yaping Dan, Ye Lu, Nicholas J Kybert, Zhengtang Luo, and AT Charlie Johnson. Intrinsic response of graphene vapor sensors. *Nano Letters*, 9(4):1472–1475, 2009.
- [59] Konstantin S Novoselov, VI Fal, L Colombo, PR Gellert, MG Schwab, K Kim, et al. A roadmap for graphene. *Nature*, 490(7419):192–200, 2012.
- [60] Vasilios Georgakilas, Michal Otyepka, Athanasios B Bourlinos, Vimlesh Chandra, Namdong Kim, K Christian Kemp, Pavel Hobza, Radek Zboril, and Kwang S Kim. Functionalization of graphene: covalent and non-covalent approaches, derivatives and applications. *Chemical Reviews*, 112(11):6156–6214, 2012.
- [61] Daniel R Dreyer, Sungjin Park, Christopher W Bielawski, and Rodney S Ruoff. The chemistry of graphene oxide. *Chemical Society Reviews*, 39(1):228–240, 2010.
- [62] JA Johnson, CJ Benmore, S Stankovich, and RS Ruoff. A neutron diffraction study of nano-crystalline graphite oxide. *Carbon*, 47(9):2239–2243, 2009.
- [63] Sasha Stankovich, Dmitriy A Dikin, Richard D Piner, Kevin A Kohlhaas, Alfred Kleinhammes, Yuanyuan Jia, Yue Wu, SonBinh T Nguyen, and Rodney S Ruoff. Synthesis of graphene-based nanosheets via chemical reduction of exfoliated graphite oxide. *Carbon*, 45(7):1558–1565, 2007.
- [64] Songfeng Pei and Hui-Ming Cheng. The reduction of graphene oxide. *Carbon*, 50(9):3210–3228, 2012.

- [65] Cristina Botas, Patricia Alvarez, Clara Blanco, Ricardo Santamaría, Marcos Granda, M Dolores Gutiérrez, Francisco Rodríguez-Reinoso, and Rosa Menéndez. Critical temperatures in the synthesis of graphene-like materials by thermal exfoliation–reduction of graphite oxide. *Carbon*, 52:476–485, 2013.
- [66] Ji Won Suk, Richard D Piner, Jinho An, and Rodney S Ruoff. Mechanical properties of monolayer graphene oxide. *Acs Nano*, 4(11):6557–6564, 2010.
- [67] Weiwei Cai, Richard D Piner, Frank J Stadermann, Sungjin Park, Medhat A Shaibat, Yoshitaka Ishii, Dongxing Yang, Aruna Velamakanni, Sung Jin An, Meryl Stoller, et al. Synthesis and solid-state nmr structural characterization of ^{13}C -labeled graphite oxide. *Science*, 321(5897):1815–1817, 2008.
- [68] Leah B Casabianca, Medhat A Shaibat, Weiwei W Cai, Sungjin Park, Richard Piner, Rodney S Ruoff, and Yoshitaka Ishii. Nmr-based structural modeling of graphite oxide using multidimensional ^{13}C solid-state nmr and ab initio chemical shift calculations. *Journal of the American Chemical Society*, 132(16):5672–5676, 2010.
- [69] Akbar Bagri, Cecilia Mattevi, Muge Acik, Yves J Chabal, Manish Chhowalla, and Vivek B Shenoy. Structural evolution during the reduction of chemically derived graphene oxide. *Nature Chemistry*, 2(7):581–587, 2010.
- [70] Eric C Mattson, Haihui Pu, Shumao Cui, Marvin A Schofield, Sonny Rhim, Ganhua Lu, Michael J Nasse, Rodney S Ruoff, Michael Weinert, Marija Gajdardziska-Josifovska, et al. Evidence of nanocrystalline semiconducting graphene monoxide during thermal reduction of graphene oxide in vacuum. *ACS Nano*, 5(12):9710–9717, 2011.
- [71] Suenne Kim, Si Zhou, Yike Hu, Muge Acik, Yves J Chabal, Claire Berger, Walt de Heer, Angelo Bongiorno, and Elisa Riedo. Room-temperature metastability of multilayer graphene oxide films. *Nature Materials*, 11(6):544–549, 2012.
- [72] Bing Huang, Hongjun Xiang, Qiang Xu, and Su-Huai Wei. Overcoming the phase inhomogeneity in chemically functionalized graphene: the case of graphene oxides. *Physical Review Letters*, 110(8):085501, 2013.
- [73] D Pandey, R Reifengerger, and R Piner. Scanning probe microscopy study of exfoliated oxidized graphene sheets. *Surface Science*, 602(9):1607–1613, 2008.
- [74] Je-Luen Li, Konstantin N Kudin, Michael J McAllister, Robert K Prud'Homme, Ilhan A Aksay, and Roberto Car. Oxygen-driven unzipping of graphitic materials. *Physical Review Letters*, 96(17):176101, 2006.
- [75] RJWE Lahaye, HK Jeong, CY Park, and YH Lee. Density functional theory study of graphite oxide for different oxidation levels. *Physical Review B*, 79(12):125435, 2009.

- [76] Zhiping Xu and Kun Xue. Engineering graphene by oxidation: a first-principles study. *Nanotechnology*, 21(4):045704, 2009.
- [77] Danil W Boukhvalov and Mikhail I Katsnelson. Modeling of graphite oxide. *Journal of the American Chemical Society*, 130(32):10697–10701, 2008.
- [78] Zhenyu Li, Wenhua Zhang, Yi Luo, Jinlong Yang, and Jian Guo Hou. How graphene is cut upon oxidation? *Journal of the American Chemical Society*, 131(18):6320–6321, 2009.
- [79] Manrui Ren, Yilun Liu, Jefferson Zhe Liu, Lifeng Wang, and Quanshui Zheng. Anomalous elastic buckling of layered crystalline materials in the absence of structure slenderness. *Journal of the Mechanics and Physics of Solids*, 88:83–99, 2016.
- [80] Shepard Roberts. Dielectric and piezoelectric properties of barium titanate. *Physical Review*, 71(12):890, 1947.
- [81] Bernard Jaffe. Us patent 2,708,244 piezoelectric transducers using lead titanate and lead zirconate, May 1955.
- [82] Heiji Kawai. The piezoelectricity of poly (vinylidene fluoride). *Japanese Journal of Applied Physics*, 8(7):975, 1969.
- [83] Inderjit Chopra and Jayant Sirohi. *Smart structures theory*. Number 35. Cambridge University Press, 2013.
- [84] Khaled S Ramadan, D Sameoto, and S Evoy. A review of piezoelectric polymers as functional materials for electromechanical transducers. *Smart Materials and Structures*, 23(3):033001, 2014.
- [85] Chang-Beom Eom and Susan Trolier-McKinstry. Thin-film piezoelectric mems. *MRS Bulletin*, 37(11):1007–1017, 2012.
- [86] Xue-Qian Fang, Jin-Xi Liu, and Vijay Gupta. Fundamental formulations and recent achievements in piezoelectric nano-structures: a review. *Nanoscale*, 5(5):1716–1726, 2013.
- [87] Zhong Lin Wang and Jinhui Song. Piezoelectric nanogenerators based on zinc oxide nanowire arrays. *Science*, 312(5771):242–246, 2006.
- [88] Xi Chen, Shiyu Xu, Nan Yao, and Yong Shi. 1.6 v nanogenerator for mechanical energy harvesting using pzt nanofibers. *Nano Letters*, 10(6):2133–2137, 2010.
- [89] Ken-Tye Yong, Siu Fung Yu, et al. Aln nanowires: synthesis, physical properties, and nanoelectronics applications. *Journal of Materials Science*, 47(14):5341–5360, 2012.
- [90] Jonathan E Spanier, Alexie M Kolpak, Jeffrey J Urban, Ilya Grinberg, Lian Ouyang, Wan Soo Yun, Andrew M Rappe, and Hongkun Park. Ferroelectric phase transition in individual single-crystalline batio₃ nanowires. *Nano Letters*, 6(4):735–739, 2006.

- [91] A Ferreira, Paulo Cardoso, D Klosterman, JA Covas, FWJ Van Hattum, F Vaz, and S Lanceros-Mendez. Effect of filler dispersion on the electromechanical response of epoxy/vapor-grown carbon nanofiber composites. *Smart Materials and Structures*, 21(7):075008, 2012.
- [92] Kyle J Alvine, Vaithiyalingam Shutthanandan, Bruce W Arey, Chongmin Wang, Wendy D Bennett, and Stan G Pitman. Pb nanowire formation on al/lead zirconate titanate surfaces in high-pressure hydrogen. *Journal of Applied Physics*, 112(1):013533, 2012.
- [93] Giuseppe Romano, Giulia Mantini, Aldo Di Carlo, Arnaldo Di Carlo, Christian Falconi, and Zhong Lin Wang. Piezoelectric potential in vertically aligned nanowires for high output nanogenerators. *Nanotechnology*, 22(46):465401, 2011.
- [94] Zhou Li, Guang Zhu, Rusen Yang, Aurelia C Wang, and Zhong Lin Wang. Muscle-driven in vivo nanogenerator. *Advanced Materials*, 22(23):2534–2537, 2010.
- [95] John S Dodds, Frederick N Meyers, and Kenneth J Loh. Piezoelectric characterization of pvdf-trfe thin films enhanced with zno nanoparticles. *IEEE Sensors Journal*, 12(6):1889–1890, 2012.
- [96] M Ataka, M Mita, Hiroshi Toshiyoshi, and Hideaki Fujita. Electrostatic microactuators in a flexible sheet-based smart mems sheet# 2. In *Solid-State Sensors, Actuators and Microsystems (TRANSDUCERS & EUROSENSORS XXVII), 2013 Transducers & Eurosensors XXVII: The 17th International Conference on*, pages 2341–2344. IEEE, 2013.
- [97] A Uranga, J Verd, E Marigó, J Giner, JL Muñoz-Gamarra, and N Barniol. Exploitation of non-linearities in cmos-nems electrostatic resonators for mechanical memories. *Sensors and Actuators A: Physical*, 197:88–95, 2013.
- [98] Wen-Ming Zhang, Han Yan, Zhi-Ke Peng, and Guang Meng. Electrostatic pull-in instability in mems/nems: A review. *Sensors and Actuators A: Physical*, 214:187–218, 2014.
- [99] Dillon D Fong, G Brian Stephenson, Stephen K Streiffer, Jeffrey A Eastman, Orlando Auciello, Paul H Fuoss, and Carol Thompson. Ferroelectricity in ultrathin perovskite films. *Science*, 304(5677):1650–1653, 2004.
- [100] Susan Trolier-McKinstry and Peter Muralt. Thin film piezoelectrics for mems. *Journal of Electroceramics*, 12(1-2):7–17, 2004.
- [101] Jin-Bock Lee, Myung-Ho Lee, Chang-Kyun Park, and Jin-Seok Park. Effects of lattice mismatches in zno/substrate structures on the orientations of zno films and characteristics of saw devices. *Thin Solid Films*, 447:296–301, 2004.
- [102] Wangmin Zhou, Guangyong Huang, and Shuyuan Yin. A surface chemical potential and instability of piezoelectric thin films. *Journal of Applied Physics*, 117(14):145303, 2015.

- [103] Kenji Uchino, Eiji Sadanaga, and Terukiyo Hirose. Dependence of the crystal structure on particle size in barium titanate. *Journal of the American Ceramic Society*, 72(8):1555–1558, 1989.
- [104] Karel-Alexander N Duerloo, Mitchell T Ong, and Evan J Reed. Intrinsic piezoelectricity in two-dimensional materials. *The Journal of Physical Chemistry Letters*, 3(19):2871–2876, 2012.
- [105] Chiu-ming Lueng, Helen LW Chan, Charles Surya, and Chung-loong Choy. Piezoelectric coefficient of aluminum nitride and gallium nitride. *Journal of Applied Physics*, 88(9):5360–5363, 2000.
- [106] Michael N Blonsky, Houlong L Zhuang, Arunima K Singh, and Richard G Hennig. Ab initio prediction of piezoelectricity in two-dimensional materials. *ACS Nano*, 9(10):9885–9891, 2015.
- [107] Hanyu Zhu, Yuan Wang, Jun Xiao, Ming Liu, Shaomin Xiong, Zi Jing Wong, Ziliang Ye, Yu Ye, Xiaobo Yin, and Xiang Zhang. Observation of piezoelectricity in free-standing monolayer mos2. *Nature Nanotechnology*, 10(2):151–155, 2015.
- [108] Wenzhuo Wu, Lei Wang, Yilei Li, Fan Zhang, Long Lin, Simiao Niu, Daniel Chenet, Xian Zhang, Yufeng Hao, Tony F Heinz, et al. Piezoelectricity of single-atomic-layer mos2 for energy conversion and piezotronics. *Nature*, 514(7523):470–474, 2014.
- [109] Matthew Zelisko, Yuranan Hanlumyuang, Shubin Yang, Yuanming Liu, Chihou Lei, Jiangyu Li, Pulickel M Ajayan, and Pradeep Sharma. Anomalous piezoelectricity in two-dimensional graphene nitride nanosheets. *Nature Communications*, 5, 2014.
- [110] WM Huang, Y Zhao, CC Wang, Z Ding, H Purnawali, C Tang, and JL Zhang. Thermo/chemo-responsive shape memory effect in polymers: a sketch of working mechanisms, fundamentals and optimization. *Journal of Polymer Research*, 19(9):1–34, 2012.
- [111] Kiyoshi Yamauchi, Ichizo Ohkata, Koichi Tsuchiya, and Shuichi Miyazaki. *Shape memory and superelastic alloys: Applications and technologies*. Elsevier, 2011.
- [112] Arne Ölander. An electrochemical investigation of solid cadmium-gold alloys. *Journal of the American Chemical Society*, 54(10):3819–3833, 1932.
- [113] William J Buehler, JV Gilfrich, and RC Wiley. Effect of low-temperature phase changes on the mechanical properties of alloys near composition tni. *Journal of Applied Physics*, 34(5):1475–1477, 1963.
- [114] István Mihálcz. Fundamental characteristics and design method for nickel-titanium shape memory alloy. *Periodica Polytechnica. Engineering. Mechanical Engineering*, 45(1):75, 2001.

- [115] G Eggeler, E Hornbogen, A Yawny, A Heckmann, and M Wagner. Structural and functional fatigue of niti shape memory alloys. *Materials Science and Engineering: A*, 378(1):24–33, 2004.
- [116] Dimitris C Lagoudas. *Shape memory alloys: modeling and engineering applications*. Springer Science & Business Media, 2008.
- [117] Xiaobing Ren and Kazuhiro Otsuka. Origin of rubber-like behaviour in metal alloys. *Nature*, 389(6651):579–582, 1997.
- [118] Hiroyasu Funakubo and JB Kennedy. Shape memory alloys. *Gordon and Breach, xii+ 275, 15 x 22 cm, Illustrated*, 1987.
- [119] Stephen Derby, M Sreekumar, T Nagarajan, M Singaperumal, M Zoppi, and R Molfino. Critical review of current trends in shape memory alloy actuators for intelligent robots. *Industrial Robot: An International Journal*, 34(4):285–294, 2007.
- [120] Cees Bil, Kevin Massey, and Ermira J Abdullah. Wing morphing control with shape memory alloy actuators. *Journal of Intelligent Material Systems and Structures*, 24(7):879–898, 2013.
- [121] Darren J Hartl and Dimitris C Lagoudas. Aerospace applications of shape memory alloys. *Proceedings of the Institution of Mechanical Engineers, Part G: Journal of Aerospace Engineering*, 221(4):535–552, 2007.
- [122] H Kahn, MA Huff, and AH Heuer. The tini shape-memory alloy and its applications for mems. *Journal of Micromechanics and Microengineering*, 8(3):213, 1998.
- [123] Li Sun, Wei Min Huang, Zhi Ding, Y Zhao, Chang Chun Wang, Hendra Purnawali, and Cheng Tang. Stimulus-responsive shape memory materials: a review. *Materials & Design*, 33:577–640, 2012.
- [124] Jinsong Leng, Xin Lan, Yanju Liu, and Shanyi Du. Shape-memory polymers and their composites: stimulus methods and applications. *Progress in Materials Science*, 56(7):1077–1135, 2011.
- [125] Andreas Lendlein and Steffen Kelch. Shape-memory polymers. *Angewandte Chemie International Edition*, 41(12):2034–2057, 2002.
- [126] Jinlian Hu. *Advances in shape memory polymers*. Elsevier, 2013.
- [127] W Huang. On the selection of shape memory alloys for actuators. *Materials & design*, 23(1):11–19, 2002.
- [128] Christoph Chluba, Wenwei Ge, Rodrigo Lima de Miranda, Julian Strobel, Lorenz Kienle, Eckhard Quandt, and Manfred Wuttig. Ultralow-fatigue shape memory alloy films. *Science*, 348(6238):1004–1007, 2015.
- [129] I Bellin, S Kelch, R Langer, and A Lendlein. Polymeric triple-shape materials. *Proceedings of the National Academy of Sciences*, 103(48):18043–18047, 2006.

- [130] Marc Behl and Andreas Lendlein. Triple-shape polymers. *Journal of Materials Chemistry*, 20(17):3335–3345, 2010.
- [131] Qian Zhao, Marc Behl, and Andreas Lendlein. Shape-memory polymers with multiple transitions: complex actively moving polymers. *Soft Matter*, 9(6):1744–1755, 2013.
- [132] Xiaofan Luo and Patrick T Mather. Triple-shape polymeric composites (tspcs). *Advanced Functional Materials*, 20(16):2649–2656, 2010.
- [133] Tao Xie. Tunable polymer multi-shape memory effect. *Nature*, 464(7286):267–270, 2010.
- [134] Guoqin Liu, Xiaobin Ding, Yiping Cao, Zhaohui Zheng, and Yuxing Peng. Novel shape-memory polymer with two transition temperatures. *Macromolecular Rapid Communications*, 26(8):649–652, 2005.
- [135] Tao Xie, Xingcheng Xiao, and Yang-Tse Cheng. Revealing triple-shape memory effect by polymer bilayers. *Macromolecular Rapid Communications*, 30(21):1823–1827, 2009.
- [136] GA Shaw, DS Stone, AD Johnson, AB Ellis, and WC Crone. Shape memory effect in nanoindentation of nickel–titanium thin films. *Applied Physics Letters*, 83(2):257–259, 2003.
- [137] Zhen Wang, Curt Hansen, Qi Ge, Sajjad H Maruf, Dae Up Ahn, H Jerry Qi, and Yifu Ding. Programmable, pattern-memorizing polymer surface. *Advanced Materials*, 23(32):3669–3673, 2011.
- [138] Aayush A Shah, Benjamin Schultz, Wenjia Zhang, Sharon C Glotzer, and Michael J Solomon. Actuation of shape-memory colloidal fibres of janus ellipsoids. *Nature Materials*, 14(1):117–124, 2015.
- [139] Jose San Juan, Maria L Nó, and Christopher A Schuh. Superelasticity and shape memory in micro-and nanometer-scale pillars. *Advanced Materials*, 20(2):272–278, 2008.
- [140] N Liu, Q Xie, WM Huang, SJ Phee, and NQ Guo. Formation of micro protrusion arrays atop shape memory polymer. *Journal of Micromechanics and Microengineering*, 18(2):027001, 2008.
- [141] N Liu, WM Huang, SJ Phee, H Fan, and KL Chew. A generic approach for producing various protrusive shapes on different size scales using shape-memory polymer. *Smart Materials and Structures*, 16(6):N47, 2007.
- [142] Zhen Zhang, Xiangdong Ding, Jun Sun, Tetsuro Suzuki, Turab Lookman, Kazuhiro Otsuka, and Xiaobing Ren. Nonhysteretic superelasticity of shape memory alloys at the nanoscale. *Physical Review Letters*, 111(14):145701, 2013.

- [143] Koji Asaka, Yoshihiko Hirotsu, and Tsugio Tadaki. Structure of nanometer-sized au-cd alloy particles near equiatomic compositions at room temperature. *Materials Science and Engineering: A*, 312(1):232–236, 2001.
- [144] T Waitz, V Kazykhanov, and HP Karnthaler. Martensitic phase transformations in nanocrystalline niti studied by tem. *Acta Materialia*, 52(1):137–147, 2004.
- [145] Kenta Seki, Hiroaki Kura, Tetsuya Sato, and Tomoyasu Taniyama. Size dependence of martensite transformation temperature in ferromagnetic shape memory alloy fepd. *Journal of Applied Physics*, 103(6):063910, 2008.
- [146] Malcolm E Lines and Alastair M Glass. *Principles and applications of ferroelectrics and related materials*. Oxford university press, 1977.
- [147] Jinxing Zhang, Xiaoxing Ke, Gaoyang Gou, Jan Seidel, Bin Xiang, Pu Yu, Wen-I Liang, Andrew M Minor, Ying-hao Chu, Gustaaf Van Tendeloo, et al. A nanoscale shape memory oxide. *Nature Communications*, 4, 2013.
- [148] Harper Meng and Guoqiang Li. A review of stimuli-responsive shape memory polymer composites. *Polymer*, 54(9):2199–2221, 2013.
- [149] Matthew J Allen, Vincent C Tung, and Richard B Kaner. Honeycomb carbon: a review of graphene. *Chemical Reviews*, 110(1):132–145, 2009.
- [150] Ray H Baughman, Anvar A Zakhidov, and Walt A de Heer. Carbon nanotubes—the route toward applications. *Science*, 297(5582):787–792, 2002.
- [151] AM Fennimore, TD Yuzvinsky, Wei-Qiang Han, MS Fuhrer, J Cumings, and A Zettl. Rotational actuators based on carbon nanotubes. *Nature*, 424(6947):408–410, 2003.
- [152] Brian J Landi, Ryne P Raffaele, Michael J Heben, Jeffrey L Alleman, William VanDerveer, and Thomas Gennett. Single wall carbon nanotube-nafion composite actuators. *Nano Letters*, 2(11):1329–1332, 2002.
- [153] Guangyu Sun, Jenő Kürti, Miklos Kertesz, and Ray H Baughman. Dimensional changes as a function of charge injection in single-walled carbon nanotubes. *Journal of the American Chemical Society*, 124(50):15076–15080, 2002.
- [154] Vera Sazonova, Yuval Yaish, Hande Üstünel, David Roundy, Tomás A Arias, and Paul L McEuen. A tunable carbon nanotube electromechanical oscillator. *Nature*, 431(7006):284–287, 2004.
- [155] L Sekaric, JM Parpia, HG Craighead, T Feygelson, BH Houston, and JE Butler. Nanomechanical resonant structures in nanocrystalline diamond. *Applied Physics Letters*, 81(23):4455–4457, 2002.
- [156] Xinxin Li, Takahito Ono, Yuelin Wang, and Masayoshi Esashi. Ultrathin single-crystalline-silicon cantilever resonators: fabrication technology and significant specimen size effect on young’s modulus. *Applied Physics Letters*, 83(15):3081–3083, 2003.

- [157] Wenzhong Bao, Feng Miao, Zhen Chen, Hang Zhang, Wanyoung Jang, Chris Dames, and Chun Ning Lau. Controlled ripple texturing of suspended graphene and ultrathin graphite membranes. *Nature Nanotechnology*, 4(9):562–566, 2009.
- [158] Changyao Chen, Sami Rosenblatt, Kirill I Bolotin, William Kalb, Philip Kim, Ioannis Kymissis, Horst L Stormer, Tony F Heinz, and James Hone. Performance of monolayer graphene nanomechanical resonators with electrical readout. *Nature Nanotechnology*, 4(12):861–867, 2009.
- [159] Shingo Maeda, Yusuke Hara, Takamasa Sakai, Ryo Yoshida, and Shuji Hashimoto. Self-walking gel. *Advanced Materials*, 19(21):3480–3484, 2007.
- [160] Gang Gu, Michael Schmid, Po-Wen Chiu, Andrew Minett, Jérôme Fraysse, Gyu-Tae Kim, Siegmur Roth, Mikhail Kozlov, Edgar Muñoz, and Ray H Baughman. V2O5 nanofibre sheet actuators. *Nature Materials*, 2(5):316–319, 2003.
- [161] Pierre Hohenberg and Walter Kohn. Inhomogeneous electron gas. *Physical Review*, 136(3B):B864, 1964.
- [162] Walter Kohn and Lu Jeu Sham. Self-consistent equations including exchange and correlation effects. *Physical Review*, 140(4A):A1133, 1965.
- [163] Jürgen Hafner. A joint effort with lasting impact. *Nature Materials*, 9(9):690–692, 2010.
- [164] Dominik Marx and Jürg Hutter. *Ab initio molecular dynamics: basic theory and advanced methods*. Cambridge University Press, 2009.
- [165] Philip Phillips. *Advanced solid state physics*. Cambridge University Press, 2012.
- [166] Mike C Payne, Michael P Teter, Douglas C Allan, TA Arias, and JD Joannopoulos. Iterative minimization techniques for ab initio total-energy calculations: molecular dynamics and conjugate gradients. *Reviews of Modern Physics*, 64(4):1045, 1992.
- [167] Richard Car and Mark Parrinello. Unified approach for molecular dynamics and density-functional theory. *Physical Review Letters*, 55(22):2471, 1985.
- [168] J Hutter, P Ballone, M Bernasconi, P Focher, E Fois, St Goedecker, M Parrinello, and M Tuckerman. Cpmc version 3.0. *Max-Planck Institut für Festkörperforschung and IBM Zurich Research Laboratory*, 1999, 1995.
- [169] Michael P Teter, Michael C Payne, and Douglas C Allan. Solution of schrödinger equation for large systems. *Physical Review B*, 40(18):12255, 1989.
- [170] Georg Kresse and Jürgen Furthmüller. Efficiency of ab-initio total energy calculations for metals and semiconductors using a plane-wave basis set. *Computational Materials Science*, 6(1):15–50, 1996.
- [171] Georg Kresse and J Furthmüller. Software vasp, vienna (1999). *Physical Review B*, 54(11):169, 1996.

- [172] Peter E Blöchl. Projector augmented-wave method. *Physical Review B*, 50(24):17953, 1994.
- [173] Georg Kresse and Jürgen Furthmüller. Efficient iterative schemes for ab initio total-energy calculations using a plane-wave basis set. *Physical Review B*, 54(16):11169, 1996.
- [174] Georg Kresse and D Joubert. From ultrasoft pseudopotentials to the projector augmented-wave method. *Physical Review B*, 59(3):1758, 1999.